

University of Texas at Arlington

**MavMatrix**

---

Civil Engineering Dissertations

Civil Engineering Department

---

2023

# ANALYTICAL AND EXPERIMENTAL OF ELECTROMAGNETIC WAVE PROPAGATION EFFECT ON MOISTURE AND CORROSION IN AN INHOMOGENEOUS MEDIUM

Dafnik Saril Kumar David

Follow this and additional works at: [https://mavmatrix.uta.edu/civilengineering\\_dissertations](https://mavmatrix.uta.edu/civilengineering_dissertations)



Part of the [Civil Engineering Commons](#)

---

## Recommended Citation

David, Dafnik Saril Kumar, "ANALYTICAL AND EXPERIMENTAL OF ELECTROMAGNETIC WAVE PROPAGATION EFFECT ON MOISTURE AND CORROSION IN AN INHOMOGENEOUS MEDIUM" (2023). *Civil Engineering Dissertations*. 465.

[https://mavmatrix.uta.edu/civilengineering\\_dissertations/465](https://mavmatrix.uta.edu/civilengineering_dissertations/465)

This Dissertation is brought to you for free and open access by the Civil Engineering Department at MavMatrix. It has been accepted for inclusion in Civil Engineering Dissertations by an authorized administrator of MavMatrix. For more information, please contact [leah.mccurdy@uta.edu](mailto:leah.mccurdy@uta.edu), [erica.rousseau@uta.edu](mailto:erica.rousseau@uta.edu), [vanessa.garrett@uta.edu](mailto:vanessa.garrett@uta.edu).

ANALYTICAL AND EXPERIMENTAL OF ELECTROMAGNETIC WAVE PROPAGATION  
EFFECT ON MOISTURE AND CORROSION IN AN INHOMOGENEOUS MEDIUM

BY

DAFNIK SARIL KUMAR DAVID

DISSERTATION

Presented to the Faculty of the Graduate School of

The University of Texas at Arlington

in Partial Fulfillment of the Requirements

for the Degree of Doctor of Philosophy

THE UNIVERSITY OF TEXAS AT ARLINGTON

August 2023

## ABSTRACT

This dissertation presents electromagnetic wave studies for infrastructure. The research contributes to a comprehensive understanding of electromagnetic wave propagation in moisture and provides insights into corrosion detection and monitoring in reinforced concrete infrastructure. Three major studies are performed to: 1) understand the multiple wave scattering in inhomogeneous moisture medium, 2) validate the experimental reflection through analytical finite difference time domain simulations with experimental measurements, and 3) evaluate the electromagnetic wave responses in the early stage and post stage corrosion experimentally, and 4) develop rapid corrosion monitoring methodology for field applications by employing cutting-edge electromagnetic wave image processing as refer to as 3-dimensional ground-penetrating radar (3DGPR) system.

First, the propagation of electromagnetic (EM) waves in a moisture medium is influenced by various key factors, including the dielectric constant, conductivity, and magnetic/electrical permeability. However, the majority of literature studying EM waves in multiple mediums tends to place a greater emphasis on the analysis by the dielectric constant. This study of moisture mediums focuses on the importance of the dielectric constant and conductivity, as they play a significant role in EM wave behavior. In the experimental approach, the EM wave response of inhomogeneous moisture mediums undergoing a transition from a wet to a dry state over the course of a day effectively simulates the shift from saturation to drier conditions. To validate the results, EM wave frequency analyses obtained by these moisture mediums were compared with the results of numerical simulations using the finite difference time domain method, alongside moisture weight measurements. By incorporating a comprehensive approach, a deeper understanding of EM wave propagation in moisture mediums and its practical implications. This research will contribute to advancements in technology and offer valuable insights into the behavior of EM waves in various applications.

Second, in this study, numerical models are employed with an advanced computation analysis, specifically utilizing the finite difference time domain method based on Yee cell theory and Taylor series. These models

are designed to replicate the experimental setup used in the initial study. To ensure comparable evaluations, the numerical model incorporates a similar antenna source and accounts for the inhomogeneity of the medium. To verify the accuracy of the numerical model, the antenna's response is validated against the experimental data obtained from the 1600MHz antenna in an air medium. The results from these numerical simulations demonstrate a frequency analysis pattern that closely resembles the experimental EM wave frequency pattern, showcasing the model's effectiveness in capturing the specific antenna behavior and moisture variation within the medium

Third, the extent of corrosion is predominantly influenced by the amplitude response of the EM wave signals. In pursuit of a deeper understanding and analysis of the corrosion process, conducted experimental accelerated corrosion tests on concrete rebar samples in the laboratory. To verify the different corrosion stages, utilized half-cell potentials and surface resistivity measurements. Additionally, radar signals were periodically collected over the course of the experiment for the concrete samples. The EM wave analysis revealed significant variations in both amplitude and frequency during the early and post-corrosion stages. To further validate the findings, employed simulation models were developed using the FDTD method, facilitating a thorough comparison with the experimental data. Additionally, the recorded current and voltage data from the accelerated concrete samples were utilized to comprehensively study the corrosion rate.

Finally, a cutting-edge 3DGPR system was developed and demonstrated for rapid bridge deck inspection. The primary purpose of using the 3DGPR system was to identify potential areas of corroded rebar by employing multiple 1600MHz antennas. The novelty of this system lies in its ability to rapidly collect data with a distance tracking system and a bridge data mapping algorithm. Through two field studies of bridge inspection, I effectively utilized the 3DGPR system to provide comprehensive insights into the scanned bridge area. The bridge data mapping algorithm employed in the system enables us to generate a 2D interpolation map highlighting potential reinforcement corrosion areas across the scanned bridge region. This mapping technique offers valuable visual information and aids in the assessment of the bridge's



structural integrity. By integrating these multiple approaches, aim to enhance the robustness of the research findings and gain a more comprehensive understanding of the corrosion process in concrete structures.

## **ACKNOWLEDGEMENTS**

Firstly, I extend my heartfelt gratitude to my advisor, Dr. Suyun Ham, for his unwavering support and guidance. Being his student has been an immense honor, and I consider myself fortunate to have worked with him on various projects, courses, and research endeavors, which have provided invaluable experiences. Without his mentorship and encouragement, this study would not have been possible.

I am also deeply grateful to the committee members, Dr. Shin-ho Chao, Dr. Xinbao Yu, and Dr. Chen Kan, for their dedicated service as committee members and for providing valuable feedback that has significantly contributed to shaping this dissertation.

Lastly, I want to express my heartfelt appreciation to my mother, Santhi Arumugam, whose extraordinary support and unwavering love have been a constant source of strength throughout my journey at the University of Texas at Arlington. Her encouragement has been pivotal in helping me overcome challenges and achieve my academic goals.

# TABLE OF CONTENTS

CHAPTER 1	INTRODUCTION .....	1
1.1	Problem statement.....	1
1.2	Objectives and approach.....	1
CHAPTER 2	BACKGROUND .....	3
2.1	Overview.....	3
2.2	Pavement & bridge defects .....	3
2.2.1	Asphalt stripping.....	4
2.2.2	Pavement settlement .....	5
2.2.3	Structural damage .....	5
2.3	Electromagnetic wave theory.....	6
2.3.1	Electromagnetic wave propagation.....	6
2.3.2	Finite difference time domain (FDTD).....	8
2.3.3	Frequency spectrum analysis .....	11
2.4	Nondestructive testing.....	12
2.4.1	Ground penetrating radar .....	12
2.4.2	Half-cell potential .....	13
2.4.3	Surface resistivity.....	14
CHAPTER 3	MODEL STUDY .....	15
3.1	Motivation.....	15
3.2	Analytical model.....	16

3.2.1	Antenna source modeling.....	16
3.2.2	Random scattering of particle for inhomogeneous medium .....	23
3.3	Verification .....	26
3.3.1	Antenna model .....	26
3.3.2	Radom aggregate model.....	31
CHAPTER 4	MOISTURE STUDY.....	37
4.1	Motivations .....	37
4.2	Moisture model investigation.....	39
4.2.1	Experimental .....	39
4.2.2	Numerical simulation .....	40
4.3	Result and discussion.....	42
4.3.1	Analysis of experimental wave responses.....	44
4.3.2	Frequency spectrum analysis .....	50
4.3.3	Discussion and conclusion.....	57
CHAPTER 5	CORROSION STUDY .....	58
5.1	Motivations .....	58
5.2	Corrosion model investigation.....	59
5.2.1	Experimental testing: Rebar.....	59
5.2.2	Experimental testing: Embedded rebar in concrete.....	61
5.2.3	Numerical simulation.....	65
5.3	Result and discussion.....	68

5.3.1	Experimental data analysis: AC-T1, -T2 &-T3.....	68
5.3.2	Experimental data analysis: Early age concrete.....	74
5.3.3	Experimental data analysis: Mature concrete .....	83
5.3.4	Numerical simulation: Corrosion indications .....	96
5.3.5	Discussion and conclusion.....	98
CHAPTER 6 FIELD STUDY .....		103
6.1	Motivation.....	103
6.2	Advancement of a continuous 3DGPR scanning system.....	104
6.3	Algorithm for post-processing rebar identification.....	105
6.3.1	Direct wave and noise subtraction .....	105
6.3.2	Rebar picking and amplitude normalization. ....	107
6.3.3	Mapping of the 3DGPR scanning data.....	111
6.3.4	Corrosion thresholds .....	114
6.4	Field demonstration of 3DGPR scanning system .....	115
6.4.1	Inspection of Bridge 1 .....	115
6.4.2	Inspection of Bridge 2.....	117
CHAPTER 7 CONCLUSION.....		121
REFERENCES .....		124

## LIST OF FIGURES

<i>Figure 2.1. Photo of Asphalt stripping occurred in (a) bridge decks and (b) resulting from poor drainage of road asphalt pavements (Patil, 2011).</i> .....	4
<i>Figure 2.2. Pavement settlement caused by (a) subgrade softening and (b) typical concrete pavement failure due to water erosion (Jung, 2009).</i> .....	5
<i>Figure 2.3. Typical concrete bridge deck deterioration and damage: (a) corrosion of reinforcement, (b) delamination, and (c) deck spalling(Gucunski, 2013).</i> .....	6
<i>Figure 2.4. Positions of various field components. The E-components are located at the midpoint of the edges, while the H-components are situated at the center of the faces. (Yee, 1966).</i> .....	8
<i>Figure 2.5. Contrasting the resolution and accuracy: (a) FDTD and (b) FEM models. (Grosge, 2005).</i> 11	
<i>Figure 2.6. Representation of EM wave: (a) standard configuration of a commercial radar system. (b) wave responses within a multi-layered medium (n layers) (Al-Qadi, 2005).</i> .....	12
<i>Figure 2.7. Schematic illustration of Half-Cell Potential measurement. (Pour-Ghaz, 2009).</i> .....	13
<i>Figure 2.8. Representation of surface resistivity: (a) four-probe wenner array setup in a typical surface resistivity meter, (b) schematic of applied electric voltage across a surface for resistivity measurement. (Gucunski, 2011).</i> .....	14
<i>Figure 3.1. The simulation setup progresses from (a) to (c), representing variable heights (230-244 mm). (d) The wave responses corresponding to these variable heights and (e) the parameter study of the variable height indicates an increase in travel time along with consistent energy levels.</i> .....	18
<i>Figure 3.2. Simulation parameter analysis: (a) illustrates the arrangement for varying dielectric constants (3-15), with sensors placed above and a high-density polyethylene plate below. (b) The parameter study of the variable dielectric constant) reveals consistent travel time and energy characteristics.</i> .....	19
<i>Figure 3.3. Simulation parameter analysis: (a) to (c) for variable thickness (4-8 mm) considering printed circuit board and high-density polyethylene plate below the sensors. (d) parameter study of variable thickness (e) showing increasing travel time energy.</i> .....	19
<i>Figure 3.4. Data comparison of wave response analysis in air at different depths (12-20 inches or 305-506 mm) for simulations with different frequency sources: (a) 1120MHz, (b) 1300MHz, and (c) 1600MHz.</i> ..	21

*Figure 3.5. Waterfall plots for peak amplitude and boundary of metal reflection at different depths (12-20 inches or 305-506 mm) for simulations with different frequency sources: (a) 1120MHz, (b) 1300MHz, and (c) 1600MHz. .... 22*

*Figure 3.6. Designed antenna model: (a) perspective view, (b) cross-section along the transmitter showing a detailed view. .... 23*

*Figure 3.7. Simulation models of particle distribution algorithms: (a) equally spaced particles in a single plane and (b) variable patterns in a single plane. .... 24*

*Figure 3.8. Simulation model with (a) randomly distributed particles developed from the above algorithm. upon zooming in, (b) detailed aggregate model considering tolerance for aggregate positions becomes visible. .... 25*

*Figure 3.9. Experimental setup for scanning antenna at multiple depths: (a) 305mm (12 inches), (b) 356mm (14 inches), (c) 406mm (16 inches), (d) 457 mm (18 inches), and (e) 508 mm (20 inches). .... 26*

*Figure 3.10. Simulation of the designed antenna at various depths: (a) 305mm (12 inches), (b) 356mm (14 inches), (c) 406mm (16 inches), (d) 457 mm (18 inches), and (e) 508 mm (20 inches). .... 27*

*Figure 3.11. Wave response analysis in air: (a) different depths (305-506mm) for experiment and (b) waterfall plots for peak amplitude and boundary of metal reflection from experiment. .... 28*

*Figure 3.12. Wave response analysis in air: (a) different depths (305-506mm) for simulation and (b) waterfall plots for peak amplitude and boundary of metal reflection from simulation. .... 28*

*Figure 3.13. Comparison of slope lines similarity between simulation and experiment ..... 29*

*Figure 3.14. Antenna model parameter study with different depth: (a) 12-inches (b) 14-inches (c) 16-inches (d) 18 inches and (e) 20 inches with different frequency (1120 MHz, 1300MHz & 1600MHz). The dashed line corresponds to the wave response at the start of the metal surface medium. .... 31*

*Figure 3.15. Experimental setup (a) for testing varying depth with (b) two different types of aggregates of sizes 12-25 mm(left) and 25-50 mm(right). .... 32*

*Figure 3.16. Experimental wave responses result of the different size of aggregates (a) 12-25 mm and (b) 25-50 mm at three different depths. The arrival time (blue dot) from the metal surface medium is used for comparison with simulation models. .... 33*

*Figure 3.17. Scatter plot of the arrival time in experimental results for two different sizes of aggregates. .... 33*

<i>Figure 3.18. Inhomogeneous simulation model generated from random aggregate particles for different depths with two different aggregate sizes. ....</i>	<i>34</i>
<i>Figure 3.19. Scatter plot of the arrival time in simulation results for two different sizes of aggregates. ..</i>	<i>34</i>
<i>Figure 3.20. Simulation wave responses results of the different size of aggregates (a) 12-25 mm and (b) 25-50 mm at three different depths. The arrival time (blue dot) from the metal surface medium is used for comparison with experimental. ....</i>	<i>35</i>
<i>Figure 3.21. Comparison of time variation at different depths between simulation and experiment depth</i>	<i>36</i>
<i>Figure 4.1. Illustration of the transmitted incident wave transformation in an inhomogeneous medium (a) with moisture and (b) without moisture, which in return affects the reflected wave by multiple scattering to the receiver.....</i>	<i>38</i>
<i>Figure 4.2. Schematic illustration depicting the proposed experimental setup for transitioning from a saturated aggregate medium to a dry aggregate medium. ....</i>	<i>39</i>
<i>Figure 4.3. The experimental setup for moisture verification was performed on the (a) top surface and the (b) side surface to assess the evaporation effect. (c) Randomly saturated aggregate, where radar scans are attenuated.....</i>	<i>40</i>
<i>Figure 4.4. Schematic representation of the data acquisition system, from the transmitted/received antenna to data processing.....</i>	<i>40</i>
<i>Figure 4.5. The randomly distributed aggregate model M1 was used for numerical moisture studies, with the developed antenna model positioned at various locations: (a) 20 cm, (b) 22 cm, and (c) 24 cm.....</i>	<i>41</i>
<i>Figure 4.6. The randomly distributed aggregate-water model M2 considered water as discrete particles rather than a continuous property, with a reduction of water volume in the top half of the model: (a) 20%, (b) 40%, and (c) 50%.....</i>	<i>42</i>
<i>Figure 4.7. The EM wave responses obtained from the top surface at the 26 cm location demonstrate a shift in the arrival time of the bottom surface throughout the 24-hour period.....</i>	<i>43</i>
<i>Figure 4.8. The EM wave responses obtained from the side surface at the 17 cm location exhibit a shift in the arrival time of the bottom surface over the 24-hour period.....</i>	<i>43</i>
<i>Figure 4.9. The velocity variation of the signal along the side surface exhibits a gradual decrease as the depth increases. Notably, at the location of 8 cm (red mark), there is a substantial 17% increase in velocity attributed to evaporation occurring at the top surface.....</i>	<i>45</i>



<i>Figure 4.10. The arrival time for reaching the end of the aggregate medium, as observed from the side surface, demonstrates a reduction, indicating that the wave propagates faster.</i>	45
<i>Figure 4.11. The evaporation rate, derived from the EM wave data obtained from the side surface scan, is averaged for each location, and subsequently fitted with a curve.</i>	46
<i>Figure 4.12. Weight measurements of the saturated aggregate experimental setup were taken as it transitioned from a saturated to a dry state, and these measurements were fitted with a curve.</i>	46
<i>Figure 4.13. Comparing the evaporation rate and the curve fit for weight reduction serves to validate the EM wave signals.</i>	46
<i>Figure 4.14. The arrival time for reaching the end of the aggregate medium, as observed from the top surface, demonstrates a reduction, indicating that the wave propagates faster.</i>	47
<i>Figure 4.15. The evaporation rate, derived from the EM wave data of the side surface scan, was averaged for each location and plotted alongside a curve fit.</i>	48
<i>Figure 4.16. Comparing the curve fits of the evaporation rate and weight reduction serves to validate the EM wave signals.</i>	48
<i>Figure 4.17. Box plot illustrating the range and pattern of arrival times recorded throughout the testing period.</i>	49
<i>Figure 4.18. Box plot illustrating the range and pattern of maximum amplitude recorded over the testing period.</i>	49
<i>Figure 4.19. Box plot illustrating the range and pattern of the mean of the EM wave signal recorded over the testing period.</i>	50
<i>Figure 4.20. Box plot illustrating the range and pattern of frequency amplitudes recorded over the testing period.</i>	50
<i>Figure 4.21. The EM wave signal encompasses the direct wave response, the wave response within the medium, and the reflection response from the metal plate.</i>	51
<i>Figure 4.22. Frequency spectrum analysis of the windowed EM wave response signal from the top surface reveals shifts in peak frequency at various locations: (a) 14 cm (b) 16 cm, (c) 20 cm and (d) 26 cm.</i>	52
<i>Figure 4.23. Frequency spectrum analysis of the windowed EM wave response signal from side surface reveals shift in peak frequencies at location: (a) 11 cm and (b) 29 cm.</i>	53
<i>Figure 4.24. Variation in central frequency shift across different locations of the experimental EM wave spectral response.</i>	53

<i>Figure 4.25. Frequency spectrum analysis of numerical model M1 reveals a subtle peak frequency shift at distinct locations: (a) 20 cm, (b) 22 cm, and (c) 24 cm. ....</i>	<i>54</i>
<i>Figure 4.26. The frequency spectrum of numerical model M2 exhibits a significant shift in both magnitude and peak frequency. Each distinct frequency and magnitude signify the shift in the central frequency as the drying process progresses.....</i>	<i>55</i>
<i>Figure 4.27. Slight increment in peak frequency shift in numerical simulation M1, reflecting the variation in conductivity from 0.2 (saturated) to 0 (dry condition) as obtained from EM wave spectral response... </i>	<i>55</i>
<i>Figure 4.28. Increase in peak frequency shift in numerical simulation model M2, illustrating moisture variation from 50% to 20%.....</i>	<i>56</i>
<i>Figure 5.1. Schematic representation of AC-T1 testing for rebar corrosion (16 and 10 mm), conducted exclusively without concrete, aimed at providing enhanced clarity. ....</i>	<i>59</i>
<i>Figure 5.2. Schematic representation of AC-T3 testing, illustrating corrosion of two 16mm rebars in two modes: (a) constant voltage (CV) and (b) constant current (CA), conducted solely without concrete. This depiction aims to offer improved clarity regarding the voltage/current supplied. ....</i>	<i>60</i>
<i>Figure 5.3. Schematic representation of AC-T2 testing for concrete rebar specimens, focused on estimating the duration of corrosion under high voltage and current conditions.....</i>	<i>61</i>
<i>Figure 5.4. Testing of AC-T2 (a) schematic diagram of the performed antenna scan direction. (b) experimental setup positioned in the laboratory.....</i>	<i>62</i>
<i>Figure 5.5. Schematic representation of AC-T4 testing for concrete rebar specimens, aimed at understanding the corrosion effects on early-age concrete without curing.....</i>	<i>62</i>
<i>Figure 5.6. Schematic representation of AC-T5 testing, illustrating the corrosion of two 16mm concrete rebar specimens in two modes: (a) constant voltage (CV) of 6 &amp; 12V and (b) constant current (CV) of 0.1A. The aim is to comprehend the corrosion rate's effect on the EM wave. ....</i>	<i>63</i>
<i>Figure 5.7. Testing of AC-T4, T5 &amp; T6: (a) schematic diagram of the antenna scan direction performed. (b) experimental setup positioned in the laboratory.....</i>	<i>64</i>
<i>Figure 5.8. Schematic representation of AC-T5 testing, illustrating the corrosion of two 16mm concrete rebar specimens in two modes: (a) constant voltage of 10V (CV) and (b) constant current (CA) of 0.05A. The aim is to understand the effect of corrosion after 1 hour and 24 hours of drying. ....</i>	<i>65</i>
<i>Figure 5.9. Numerical model developed: (a) resemble the experimental specimen, (b) after considering the appropriate depth for clear rebar reflection.....</i>	<i>66</i>

<i>Figure 5.10. Variation in rust and rebar was considered for the numerical model simulation. ....</i>	<i>66</i>
<i>Figure 5.11. Rebar groups 1, 2, and 3 were employed to represent the variation of rebar placement in the concrete model, illustrating the impact of rust-induced changes. ....</i>	<i>68</i>
<i>Figure 5.12. Rebar obtained after AC-T1 accelerated corrosion testing, showing a mass reduction of 15% for 16mm and 32% for 10mm. ....</i>	<i>69</i>
<i>Figure 5.13. Data obtained from different locations and times for AC-T1 testing: (a) EM wave response and (b) half-cell potentials.....</i>	<i>69</i>
<i>Figure 5.14. Half-cell potential evaluation of the rebar revealed a significant reduction in potential within corroded areas.....</i>	<i>70</i>
<i>Figure 5.15. AC-T3 rebar with (a) rust particles attached to it, and (b) the rebar after the rust particles were cleaned. ....</i>	<i>70</i>
<i>Figure 5.16. Half-cell potential variation for the constant current rebar tested in AC-T3: (a) before cleaning and (b) after cleaning the rebar, highlighting the potential variation after the 7th day.....</i>	<i>71</i>
<i>Figure 5.17. Half-cell potential variation for the constant voltage rebar tested in AC-T3: (a) before cleaning and (b) after cleaning the rebar, highlighting the potential variation after the 7th day.....</i>	<i>72</i>
<i>Figure 5.18. Voltage and current data were gathered using an Arduino Mega board for both (a) constant voltage and (b) constant current configurations. In the case of constant voltage, a reduction in current flow was observed as corrosion advanced, whereas under constant current conditions, the current remained stable while voltage varied in response to corrosion.....</i>	<i>73</i>
<i>Figure 5.19. The measured weight of the clean rebar during AC-T3 testing is depicted by the blue line for constant voltage and the red line for constant current. ....</i>	<i>73</i>
<i>Figure 5.20. Corrosion rates obtained through (a) weight measurement and (b) current variation for AC-T3 reveal that in the case of constant voltage (CV), (c) the corrosion rate decreases (blue line), whereas in the constant current scenario, the rate remains relatively consistent (red line).....</i>	<i>74</i>
<i>Figure 5.21. Photos indicate corrosion progression in the rebar embedded within the concrete (a) before corrosion and (b) after corrosion for CR10 and CR16 specimens of AC-T4 testing.....</i>	<i>75</i>
<i>Figure 5.22. Mass reduction of the rebar due to accelerated corrosion in AC-T4. ....</i>	<i>75</i>
<i>Figure 5.23. Rebar diameter variation of (a) CR10 and (b) CR16, with the observed reduction in diameter marked by arrows when measured around the rebar. ....</i>	<i>76</i>

<i>Figure 5.24. Collected half-cell potential data at locations A, B, C, and D are presented over the testing period for (a) CR10 and (b) CR16 specimens of AC-T4.....</i>	<i>77</i>
<i>Figure 5.25. Surface resistivity data collected at locations A, B, C, and D are plotted over the testing period for (a) CR10 and (b) CR16 specimens of AC-T4. ....</i>	<i>78</i>
<i>Figure 5.26. Illustrating the EM wave signal transformation (a) before subtraction and (b) after subtraction, acquired for CR10 at location B. This process effectively eliminates noise and direct wave, providing a clearer resolution of the rebar reflection. ....</i>	<i>79</i>
<i>Figure 5.27. The EM waves were synchronized with the first negative peak (dotted line) to obtain a clear variation in the rebar responses. ....</i>	<i>79</i>
<i>Figure 5.28. Phase angle analysis of the EM wave is conducted to identify the optimal time window corresponding to the medium transition. This selected time window is then employed for the subsequent signal post-processing. ....</i>	<i>80</i>
<i>Figure 5.29. Signal post-processing analysis of (a) single EM wave involves determining the amplitude, signal energy, and time window for the respective (b) FFT. Spectrum analysis yields the half-bandwidth and central frequency. ....</i>	<i>81</i>
<i>Figure 5.30. Averaged half-cell potential data grouped by locations for CR10 and CR16 specimens of AC-T4. ....</i>	<i>81</i>
<i>Figure 5.31. Signal post-processing analysis of the EM wave reveals the variations in signal attributes for the specimens tested in AC-T4. These attributes include (a) signal energy, (b) signal maximum amplitude, (c) center frequency, (d) peak frequency magnitude, and (e) half-bandwidth of frequency energy. This analysis provides insights into the dynamic behavior of EM wave responses in correlation with the corrosion process.....</i>	<i>83</i>
<i>Figure 5.32. Voltage and current data were collected for AC-T5: (a) constant voltage and (b) constant current configurations. ....</i>	<i>84</i>
<i>Figure 5.33. Corrosion rates obtained from current variation in AC-T5 reveal that in the case of constant voltage (blue line), the corrosion rate remains passive until the 10th day and then progresses to an active corrosion state, whereas in the constant current scenario, the rate remains relatively consistent (red line). ....</i>	<i>84</i>
<i>Figure 5.34. Specimens subjected to accelerated corrosion in AC-T5 for constant voltage and current along with reference control specimen measured: (a) half-cell potentials and (b) surface resistivity measured for</i>	

*specimens of AC-T5. Half-cell potential indicates that the specimen undergoes active corrosion after the 12th day, consistent with the corrosion rate trend..... 85*

*Figure 5.35. The signal post-processing analysis of the EM wave provides insights into the changes in signal attributes for the specimens tested in AC-T5 during both the passive and active corrosion states. These attributes encompass (a) signal energy, (b) signal maximum amplitude, (c) center frequency, (d) peak frequency magnitude, and (e) half-bandwidth of frequency energy..... 87*

*Figure 5.36. Specimens subjected to constant voltage in AC-T6 at both 1-hour and 24-hour intervals along with reference control specimen measured: (a) half-cell potentials and (b) surface resistivity. The half-cell potential data indicates that the specimen transitions into an active corrosion state after the 10th day... 88*

*Figure 5.37. AC-T6 under constant voltage: (a) voltage data collected (b) current data collected (c) variation in corrosion rate between the passive and active states..... 89*

*Figure 5.38: The impact of moisture variation of AC-T6 between a 1-hour drying period and a 24-hour drying period is depicted in: (a) half-cell potentials, and (b) center frequency. .... 90*

*Figure 5.39. The signal post-processing analysis of the EM wave under constant voltage provides insights into the changes in signal attributes for the specimens tested in AC-T6 during both the passive and active corrosion states. These attributes encompass (a) signal energy, (b) signal maximum amplitude, (c) center frequency, (d) peak frequency magnitude, and (e) half-bandwidth of frequency energy..... 92*

*Figure 5.40. Specimens subjected to constant current in AC-T6 at both 1-hour and 24-hour intervals along with reference control specimen measured: (a) half-cell potentials and (b) surface resistivity. The half-cell potential data indicates that the specimen transitions into an active corrosion state after the 21st day. .. 93*

*Figure 5.41. AC-T6 constant current study depicting: (a) voltage data collected, (b) current data were collected (c) steady state with corrosion rate. .... 94*

*Figure 5.42. The signal post-processing analysis of the EM wave under constant current provides insights into the changes in signal attributes for the specimens tested in AC-T6 during both the passive and active corrosion states. These attributes encompass (a) signal energy, (b) signal maximum amplitude, (c) center frequency, (d) peak frequency magnitude, and (e) half-bandwidth of frequency energy..... 96*

*Figure 5.43. The signal post-processing analysis of the EM wave for numerical simulation provides insights into the changes in signal attributes for different groups 1,2 & 3 during both the passive and active corrosion states. These attributes encompass (a) signal energy, (b) signal maximum amplitude, (c) center frequency, (d) peak frequency magnitude, and (e) half-bandwidth of frequency energy..... 98*

*Figure 5.44. A parallel energy shift is observed in AC-T5 both: (a) half bandwidth frequency energy extracted from EM waves and (b) corrosion rate applied to the specimen. .... 100*

*Figure 5.45. Comparative study of the experimental EM wave analysis in AC-T6: (a) center frequency and (b) half bandwidth energy. .... 101*

*Figure 5.46. The analysis of AC-T6 constant current with EM waves exhibited a discernible but primarily upward trend without substantial significance. .... 101*

*Figure 5.47. Comparative study of the numerical EM wave analysis: (a) center frequency and (b) half bandwidth energy. .... 102*

*Figure 6.1. The field-testing setup involves the 3DGPR system, incorporating the SIR 30 data acquisition logger along with an encoder affixed to the rotating wheel. .... 105*

*Figure 6.2. Process of EM wave subtraction: (a) raw EM wave A-scan signal obtained from the data acquisition, (b) overall average of all the EM wave A-scans collected from the antenna and (c) subtracted EM wave signal, showing the rebar reflection after removal of noise and direct wave. .... 106*

*Figure 6.3. Time steps of A-scans in proximity to the rebar location are depicted: (a) before subtraction and (b) after subtraction, revealing the distinct outline of the rebar. .... 107*

*Figure 6.4. The unprocessed B-scan data (a) before and (b) after subtraction distinctly illustrate the hyperbolic reflection response of the EM wave. .... 107*

*Figure 6.5. The rebar's hyperbolic reflection is observed to occur within a specific time window, between  $t_1$  and  $t_2$ , of the EM wave signal. .... 108*

*Figure 6.6 Anticipated red dots signifying the targeted rebar location in need of identification. .... 108*

*Figure 6.7. The maximum amplitude line (depicted in blue) is plotted over the B-scan within the specified time window. .... 109*

*Figure 6.8. The rebar locations are determined by identifying the peaks of the hyperbolic curves. .... 109*

*Figure 6.9. The scatter plot depicting rebar picking in relation to depth is displayed prior to the amplitude-depth correlation, showcasing the range of variability in normalized amplitudes. The red line signifies the 90% regression line, while the black line represents the corrosion threshold with before amplitude-depth correlation. .... 110*

*Figure 6.10. The scatter plot illustrating rebar picking relative to depth is presented following the amplitude-depth correlation, highlighting the adjustment made to the normalized amplitude values. The*

*red line signifies the 90% regression line, while the black line represents the corrosion threshold after amplitude-depth correlation. .... 111*

*Figure 6.11. Mapping: correlation between encoder readings and normalized rebar amplitudes. .... 113*

*Figure 6.12. Mapping refinement: zero column removal for enhanced visualization. .... 113*

*Figure 6.13. Mapping enhancement: aligning and merging normalized amplitudes at a 3-inch resolution, accompanied by inclusion of missing encoder values..... 113*

*Figure 6.14. Mapping finalization: achieving conformity with rebar spacing in the plan through last realignment and zero column elimination. .... 114*

*Figure 6.15. The histogram illustrates the corrosion threshold, where normalized amplitude values below the threshold (TH) are categorized as corrosion..... 115*

*Figure 6.16. Concluding corrosion area map following application of normalized amplitude corrosion threshold. The red spot indicates the area with a high probability of corrosion, as identified through EM wave analysis. .... 115*

*Figure 6.17. Bridge scanning and surface defects visualization: The 3DGPR system covers a 150-meter length and 4-meter width area, employing four scanning paths (Lane 1 and Lane 2). The bridge deck exhibits multiple surface damages, including cracks and spalling..... 116*

*Figure 6.18. Results of the initial bridge inspection: (a) Delamination Map, (b) Corrosion Map. The red box indicates the corresponding regions between the delamination and corrosion maps, while the yellow box highlights the corroded area that could potentially result in delamination..... 117*

*Figure 6.19. The bridge was subjected to scanning using the 3DGPR system, covering an expanse of 150 meters in length and 4 meters in width through four distinct scanning paths (designated as Lane 1 and Lane 2). .... 118*

*Figure 6.20. Bridge 2 inspection results: corrosion maps for three sequential scans: (a) 03/2022, (b) 06/2022 and (c) 11/2022, highlighting affected areas, alongside visual damage patches (Ham, 2023).. 120*

## LIST OF TABLES

<i>Table 3.1. Parametric variable considered parametric antenna model design.....</i>	<i>16</i>
<i>Table 3.2. Parameter values of the antenna model obtained after several simulations. ....</i>	<i>20</i>
<i>Table 5.1. Parameter variables considered for corrosion study involving rust and rebar.....</i>	<i>66</i>
<i>Table 5.2. Collective investigation involving numerical simulations with varying combinations of rebar rust diameters.....</i>	<i>67</i>
<i>Table 6.1. Progression of Detected Damage Across Three Scans.....</i>	<i>119</i>



# **CHAPTER 1 INTRODUCTION**

## **1.1 Problem statement**

Infrastructure including runways and bridges, typically constructed with inhomogeneous material such as concrete and asphalt, are designed to have a sustainable service life of 30 to 50 years. However, due to various external factors such as environmental conditions and transportation fatigue, damage gradually develops over time. This damage can range from mild to severe cases, posing potential risks to structural integrity and safety. The initial focus of this dissertation is to address the challenge of early detection of damage using nondestructive methods and analysis. Detecting damages at an early stage is crucial to implement timely repair or remedial measures, which can prevent further deterioration and ensure the longevity of the structures. Visible damage to these structures often includes cracks, delamination, pavement settlement, and asphalt stripping. However, the underlying root cause of these damages is typically linked to moisture inside or beneath the concrete and corrosion. Moisture penetration and corrosion can significantly weaken the concrete, leading to the observed damage. Therefore, the research objective is to develop effective methods for detecting and evaluating concrete moisture and corrosion in a timely manner.

## **1.2 Objectives and approach**

The primary goal of this study is to present an approach for detecting and evaluating concrete damage, mainly caused by two major factors: moisture and corrosion. The research encompasses several studies conducted to achieve different objectives.

Objective 1 focuses on comprehending the electromagnetic (EM) wave responses from the reflected inhomogeneous moisture medium using both experimental and numerical methods. Chapter 3 introduces

the numerical method, finite difference time domain (FDTD), to analyze the EM wave response within the inhomogeneous moisture medium. Chapter 4 presents the experimental responses from the inhomogeneous moisture medium. The culmination of Study 1 is the proposal of a moisture evaluation method using the incremental variation of the center frequency.

In Objective 2, the investigation delves into understanding the EM wave responses from the reflected concrete corrosion medium using field, experimental, and numerical methods. Chapter 5 entails the analysis of the 3-dimensional ground penetrating radar (3DGPR) and the mapping of potential detection areas for corrosion. Chapter 6 delves into further experimental and numerical methods for studying corrosion stages. Study 2 concludes with the proposition of a corrosion evaluation approach utilizing the variations in amplitude and center frequency.

By conducting these studies and proposing evaluation approaches, this research aims to contribute to a better understanding of concrete damages caused by moisture and corrosion, ultimately leading to improved methods for early detection and effective evaluation of such damages in various structures.

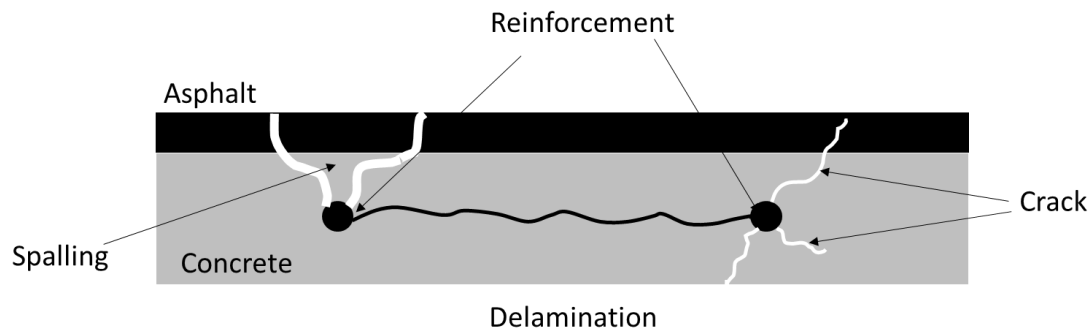
## CHAPTER 2 BACKGROUND

### 2.1 Overview

This chapter provides the fundamental background necessary to comprehend the studies conducted in this dissertation. Begins by discussing general concrete defects and the fundamental theory of electromagnetic wave propagation. Understanding these concepts is essential for the subsequent investigations. Additionally, it explores various nondestructive testing (NDT) methods commonly employed to identify and evaluate concrete damages, in particular corrosion. Understanding these concepts is essential for the subsequent investigations and analyses carried out in this research.

### 2.2 Pavement & bridge defects

Concrete pavements and bridge decks commonly experience various types of distress, such as cracking, spalling, and delamination, as illustrated in the mentioned study. This section provides an overview of the fundamental background related to concrete distress, including the different types of distress and their underlying causes. By understanding these aspects, gains valuable insights into the challenges faced by concrete structures and explore potential solutions to address these issues.



**Figure 2.1:** Typical damage of concrete due to distress. These distresses are primarily caused by corrosion and moisture within the concrete.

### 2.2.1 Asphalt stripping

Asphalt stripping is a distress phenomenon that occurs in asphalt pavements, where the bond between the asphalt binder and the aggregate particles in the pavement mix is compromised. This leads to the separation of the asphalt from the aggregate surface, resulting in the loss of adhesion. Moisture infiltration is often a contributing factor, especially through cracks or voids in the pavement structure, weakening the asphalt-aggregate bond (Patil, 2011). Regions with high rainfall or poor drainage are particularly susceptible to this issue. The stripped areas are vulnerable to further damage from moisture intrusion, which can cause more extensive deterioration, including cracking and potholes. Additionally, the reduction in structural integrity makes the pavement less capable of withstanding heavy traffic loads and environmental stresses. Addressing asphalt stripping is crucial to ensure the long-term durability and performance of asphalt pavements, and preventive measures are essential to mitigate its impact on the pavement's integrity and safety.



(a)



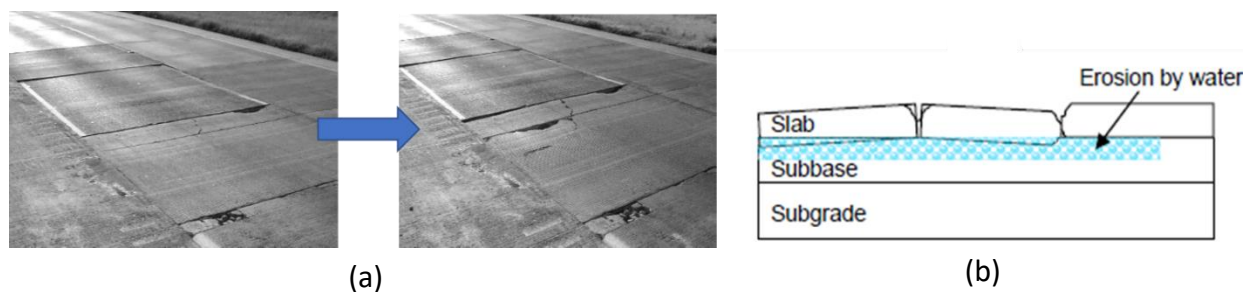
(b)

**Figure 2.1. Photo of Asphalt stripping occurred in (a) bridge decks and (b) resulting from poor drainage of road asphalt pavements (Patil, 2011).**

### 2.2.2 *Pavement settlement*

Pavement settlement refers to the downward movement or depression of a road surface or pavement structure relative to its original position. This phenomenon occurs when the ground underneath the pavement compresses, weakens, or shifts, leading to the pavement sinking or settling. Several factors can contribute to pavement settlement, including soil consolidation, poor soil compaction, and softening due to erosion caused by water flow.

The consequences of pavement settlement can be significant, resulting in various problems and hazards such as an uneven surface and structural damage as shown in Figure 2.2 (Jung, 2009). Moreover, structural damage can compromise the pavement's integrity, potentially leading to more extensive repairs and higher costs.

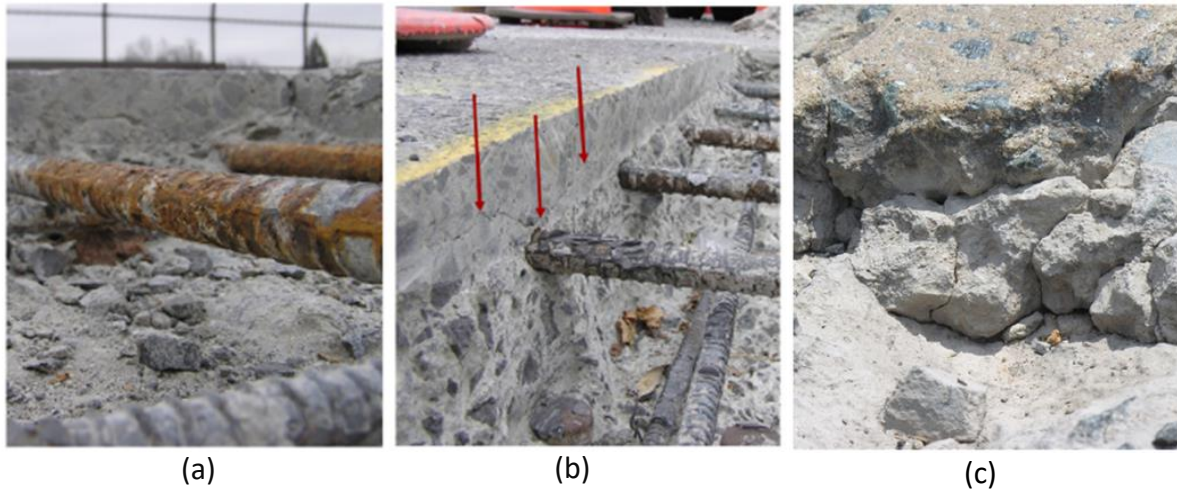


**Figure 2.2. Pavement settlement caused by (a) subgrade softening and (b) typical concrete pavement failure due to water erosion (Jung, 2009).**

### 2.2.3 *Structural damage*

Structural damage in the context of bridge decks refers to the deterioration, degradation, or impairment of the components and overall integrity of the uppermost surface of the bridge. This surface directly supports the traffic load and provides a platform for vehicles and pedestrians to cross over the bridge. The occurrence of bridge deck structural damage can be attributed to various factors, including environmental conditions, traffic load, and design and construction practices. Common types of bridge deck structural damage as depicted in Figure 2.3 include cracks, spalling, delamination, potholes, and corrosion of reinforcement

include cracks, spalling, delamination, potholes, and corrosion of reinforcement (Gucunski, 2013). Early detection and prompt addressing of bridge deck structural damage are imperative for maintaining the safety and serviceability of the bridge. Timely intervention and repair measures are essential to prevent further deterioration, ensure the integrity of the structure, and extend the bridge's lifespan.



**Figure 2.3. Typical concrete bridge deck deterioration and damage: (a) corrosion of reinforcement, (b) delamination, and (c) deck spalling (Gucunski, 2013).**

## 2.3 Electromagnetic wave theory

### 2.3.1 *Electromagnetic wave propagation*

EM waves are a fundamental form of energy propagation characterized by oscillating electric and magnetic fields. These waves arise from the acceleration of charged particles, particularly electrons. Remarkably, EM waves can traverse in a vacuum, such as space, as well as mediums like air, water, or solids. Their behavior and propagation are described mathematically by Maxwell's equations (Benedetto, 2014) expressed as:

$$\nabla \times E = -\frac{\partial B}{\partial t}, \quad 2.1$$

$$\nabla \times H = J + \frac{\partial D}{\partial t}, \quad 2.2$$

$$D = \varepsilon E, \quad 2.3$$

$$B = \mu H, \quad 2.4$$

where,  $D$  &  $B$  represent the electric and magnetic flux density. respectively, while  $E$  &  $H$  represent the electric and magnetic field intensity,  $J$  stands for current density,  $\varepsilon$  denotes the relative permittivity, and  $\mu$  represents the permeability of the medium. By further solving the above equations 2.1 to 2.4, the harmonic plane wave equation can be obtained (Benedetto, 2014). These equations play a fundamental role in understanding the behavior of EM waves and their propagation in different mediums expressed as:

$$\vec{E} = \vec{E}_0 \cdot e^{-\alpha \cdot \vec{r}} \cdot e^{-j\beta \cdot \vec{r}}, \quad 2.5$$

$$\alpha = \omega \cdot \sqrt{\mu\varepsilon} \cdot \sqrt{0.5 \cdot (\sqrt{1 + \tan^2 \delta} - 1)}, \quad 2.6$$

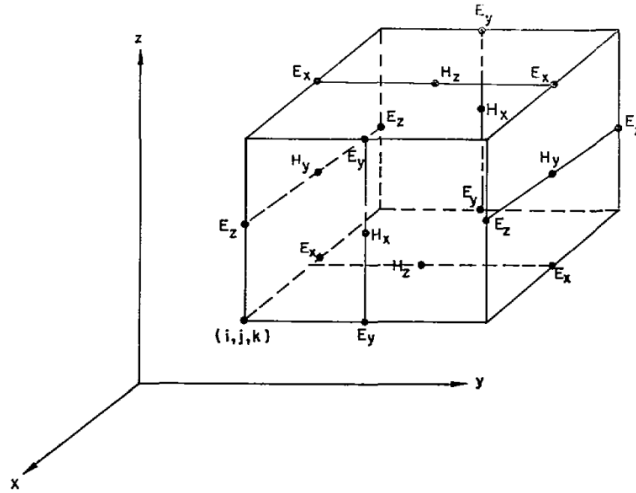
$$\beta = \omega \cdot \sqrt{\mu\varepsilon} \cdot \sqrt{0.5 \cdot (\sqrt{1 + \tan^2 \delta} + 1)}, \quad 2.7$$

$$\tan \delta = \frac{\sigma}{\omega \cdot \varepsilon}, \quad 2.8$$

where  $\sigma$  - conductivity,  $\omega$  – frequency of the signal applied. The behavior of EM wave in a medium is determined by its conductivity, permeability, and relative permittivity. In the case of ground penetrating radar, the relative permittivity of the subsurface material plays a crucial role. The electrical conductivity of the material, which is typically influenced by its moisture content, strongly affects the EM wave behavior. In non-destructive testing using EM waves, these waves are directed into the structure, and the reflected signals are analyzed to gather information about the internal condition of the material. The advantage of employing EM waves for NDT in civil engineering lies in their ability to provide valuable information about the structural condition without the need for invasive testing methods.

### 2.3.2 Finite difference time domain (FDTD)

Finite-difference time-domain method is a direct space method (Figure 2.4), first introduced by Kane S. Yee (Yee 1966). The FDTD method is a widely used numerical technique for simulating EM fields. It discretizes both the time and space domains and solves Maxwell's equations at discrete points in time and space to simulate wave propagation (Grosjes, 2005).



**Figure 2.4. Positions of various field components. The E-components are located at the midpoint of the edges, while the H-components are situated at the center of the faces. (Yee, 1966).**

The governing equations for Maxwell's time-varying EM fields are expressed in Eq.2.9 -2.12.

$$\nabla \cdot D = \rho_v, \quad 2.9$$

$$\nabla \cdot B = 0, \quad 2.10$$

$$\nabla \times E = -\frac{\partial B}{\partial t}, \quad 2.11$$

$$\nabla \times H = J + \frac{\partial D}{\partial t}, \quad 2.12$$

$$D = \epsilon E, \quad 2.13$$

$$B = \mu H, \quad 2.14$$



where, electric flux density (D) is the propagation of the electric field (E) through a medium with permittivity ( $\epsilon$ ), while magnetic flux density (B) is the propagation of the magnetic field (H) through a medium with permeability ( $\mu$ ) The charge density ( $\rho_v$ ) and current density (J) describe the distribution of charge and current within the medium. To study a free-source medium, we can apply the curl operator to both sides of Eq.2.11 will be expressed as:

$$\nabla \times \nabla \times E = -\frac{\partial \nabla \times B}{\partial t} \quad 2.15$$

By solving Eq.2.15, we can obtain the three-dimensional spatial effect resulting from changes in the electric field over time, while taking into account the permittivity and permeability of the medium as:

$$\nabla^2 E = \mu\epsilon \frac{\partial^2 E}{\partial t^2}, \quad 2.16$$

$$\nabla^2 E = \frac{\partial^2 E}{\partial x^2} + \frac{\partial^2 E}{\partial y^2} + \frac{\partial^2 E}{\partial z^2},$$

$$\frac{\partial^2 E}{\partial x^2} + \frac{\partial^2 E}{\partial y^2} + \frac{\partial^2 E}{\partial z^2} = \mu\epsilon \frac{\partial^2 E}{\partial t^2}, \quad 2.17$$

The FDTD method, which employs the second-order central difference algorithm in the Yee cell (Yee, 1966) is commonly used to simulate EM wave propagation. This numerical method involves discretizing both space and time and replacing the derivatives in Ampere's and Faraday's laws with finite differences. By doing so, the electric and magnetic fields can be staggered in both space and time. The difference equations are then solved to obtain update equations that express the future EM fields in terms of past EM fields. The magnetic fields are evaluated one time-step into the future, effectively becoming past fields, followed by the evaluation of electric fields one time-step into the future, also becoming past fields. These steps are repeated until the fields have been obtained over the desired duration. The FDTD method is a powerful numerical tool for simulating EM wave propagation and finds applications in various fields, including optics, electromagnetics, and microwave engineering. Considering the Yee cell theory (Yee, 1966) Maxwell equation with applying curl can be rewritten as:

$$-\sigma_m H_x - \mu \frac{\partial H_x}{\partial t} = \frac{\partial E_z}{\partial y} - \frac{\partial E_y}{\partial z}, \quad 2.18$$

$$-\sigma_m H_y - \mu \frac{\partial H_y}{\partial t} = \frac{\partial E_x}{\partial z} - \frac{\partial E_z}{\partial x}, \quad 2.19$$

$$-\sigma_m H_z - \mu \frac{\partial H_z}{\partial t} = \frac{\partial E_y}{\partial x} - \frac{\partial E_x}{\partial y}, \quad 2.20$$

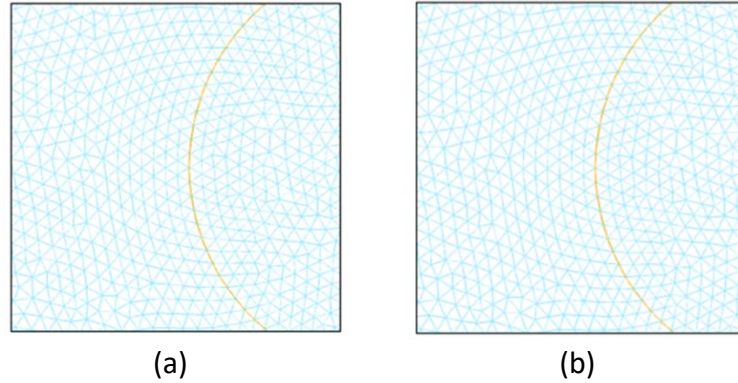
$$\sigma E_x + \varepsilon \frac{\partial E_x}{\partial t} = \frac{\partial H_z}{\partial y} - \frac{\partial H_y}{\partial z}, \quad 2.21$$

$$\sigma E_y + \varepsilon \frac{\partial E_y}{\partial t} = \frac{\partial H_x}{\partial z} - \frac{\partial H_z}{\partial x}, \quad 2.22$$

$$\sigma E_z + \varepsilon \frac{\partial E_z}{\partial t} = \frac{\partial H_y}{\partial x} - \frac{\partial H_x}{\partial y}, \quad 2.23$$

where  $\sigma_m$  is the magnetic conductivity and  $\sigma$  is the electrical conductivity. In the Yee cell numerical simulation, parameters affecting the medium are taken into consideration. These parameters include the permittivity and permeability that are used in the Maxwell equations (Eq. 2.9 -2.12). These properties affect the EM waves by influencing the wave energy's attenuation and interface within the medium.

The FDTD numerical method offers several advantages, one of which is its regular alignment, as demonstrated by the use of the first derivative of the Taylor theorem for calculation (Grosge, 2005). In contrast, finite element modeling (FEM) numerical analysis involves an irregular Cartesian coordinate grid with complex integrals and mathematical computations, as illustrated in Figure 2.5. Additionally, the FDTD simulation requires considerably less processing time, even for very fine resolutions. This computational efficiency makes FDTD an attractive choice for simulations and modeling tasks, particularly in scenarios where processing speed and regular grid alignment are critical factors for accurate and swift analysis.



**Figure 2.5. Contrasting the resolution and accuracy: (a) FDTD and (b) FEM models.** (Grosjes, 2005).

### 2.3.3 Frequency spectrum analysis

Frequency spectrum analysis is a fundamental technique employed to analyze and depict the frequency components present in a signal or waveform. By breaking down a signal into its constituent frequencies, this analysis enables a comprehensive understanding of its frequency content and characteristics. As a pivotal tool in signal processing, frequency spectrum analysis provides valuable insights into the behavior and features of diverse signals, enhancing the processing of real-world data.

Various tools are utilized for frequency spectrum analysis, including fast fourier transform (FFT), spectrogram, and power spectral density (PSD). For the purpose of this study, FFT will be employed to acquire and analyze the EM wave signals. This technique will facilitate the examination of the EM wave's frequency composition and patterns, contributing to the overall investigation and understanding of the EM wave behavior in different mediums.

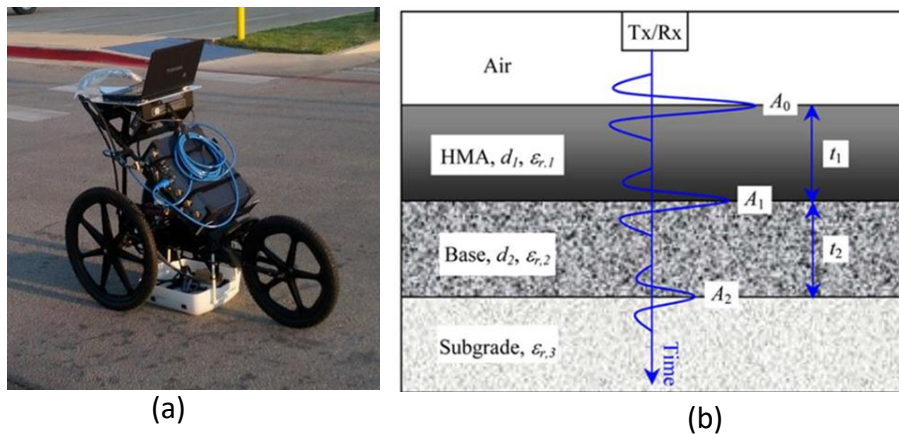
## 2.4 Nondestructive testing

### 2.4.1 Ground penetrating radar

GPR utilizes EM waves to penetrate the ground or other materials, capturing the reflections and scattering of these waves to generate a detailed subsurface image (Figure 2.6(a)). The emitted EM waves travel through the subsurface, encountering interfaces between different materials such as soil layers, rock formations, or buried objects. Some of the waves are reflected to the surface, as illustrated in Figure 2.6(b), while others continue to propagate deeper. The system records the time taken for these waves to return to the surface after reflection. The thickness of the  $i^{\text{th}}$  layer (Al-Qadi, 2005) can be calculated using the following:

$$d_i = \frac{c \cdot t_i}{2\sqrt{\epsilon_{r,i}}} \quad 2.24$$

where  $d_i$  is the thickness of the  $i^{\text{th}}$  layer,  $t_i$  is the EM wave two-way travel time through the  $i^{\text{th}}$  layer as shown in,  $c$  is the speed of light in free space, and  $\epsilon_{r,i}$  is the dielectric constant of the  $i^{\text{th}}$  layer.

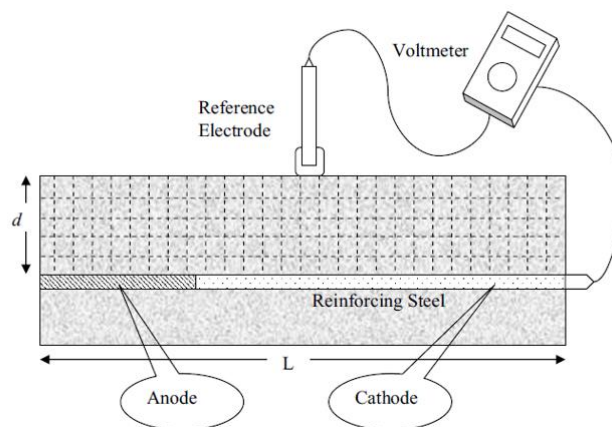


**Figure 2.6. Representation of EM wave: (a) standard configuration of a commercial radar system. (b) wave responses within a multi-layered medium ( $n$  layers) (Al-Qadi, 2005).**

After collecting the GPR data profile, it undergoes processing and analysis to create a representation of the subsurface in either two dimensions (B-scan) or three dimensions (C-scan). In the B-scan or C-scan images, different subsurface features are depicted through distinct reflection patterns. These scans provide valuable insights into the subsurface composition, allowing researchers and professionals to identify and interpret various subsurface structures, such as soil layers, buried objects, or voids.

### 2.4.2 *Half-cell potential*

Half-cell potential, also known as electrode potential or corrosion potential, is a fundamental parameter used in corrosion studies to assess the electrochemical potential difference between a reference electrode and the metal surface of interest. The measurement of the half-cell potential provides crucial information about the material's electrochemical behavior and its susceptibility to corrosion. To measure the half-cell potential, a setup involving a working electrode and a reference electrode is used, as depicted in Figure 2.7. The voltmeter is utilized to measure the potential difference between the working electrode and the reference electrode (Pour-Ghaz, 2009). This potential difference is then recorded as the half-cell potential of the metal.



**Figure 2.7. Schematic illustration of Half-cell potential measurement.** (Pour-Ghaz, 2009).

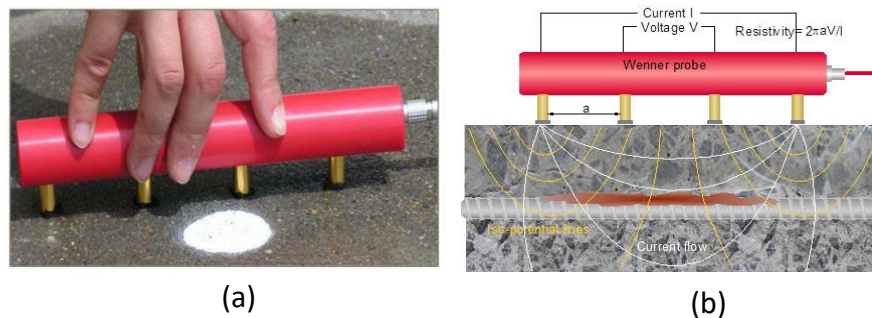
The half-cell potential serves as a valuable indicator to determine the current state of a metal surface, whether it is undergoing corrosion, in a passive state, or immune to corrosion. By analyzing the half-cell potential, one can predict the metal's tendency to corrode under specific environmental conditions.

### 2.4.3 Surface resistivity.

Surface resistivity is a crucial parameter that quantifies a material's electrical resistance across its surface. It measures how effectively a material can conduct or resist the flow of electric current along its surface, as illustrated in (Figure 2.8(a)). Surface resistivity represents the resistance between two opposite edges of a square area on the material's surface. The resistance  $\rho$  is then calculated with:

$$\text{Resistivity}(\rho) = \frac{2\pi aV}{i}, \quad 2.25$$

where  $\rho$  is the resistance,  $V$  is the applied voltage, and  $I$  is the measured current. Surface resistivity as shown in Figure 2.8(b) is measured by applying a known voltage  $V$  across the opposite edges of an area ( $2\pi a$ ) on the material's surface and measuring the resulting current flow.



**Figure 2.8. Representation of surface resistivity: (a) four-probe wenner array setup in a typical surface resistivity meter, (b) schematic of applied electric voltage across a surface for resistivity measurement.** (Gucunski, 2011).

Surface resistivity is influenced by several factors, including the material's electrical conductivity and the thickness of any surface coatings or layers. Materials with low surface resistivity exhibit high electrical conductivity, allowing electric current to flow easily across their surface. Conversely, materials with high surface resistivity possess low electrical conductivity and impede the flow of current.

## CHAPTER 3 MODEL STUDY

### 3.1 Motivation

This study is divided into two main tasks aimed at advancing our understanding of EM waves and their behavior through different modeling approaches.

The first task focuses on comprehending EM waves through various antenna modeling designs and establishing a testing configuration to enable comparative analysis of simulation models. To achieve this, an extensive literature review on EM waves and antenna modeling is conducted. Subsequently, simulation models are designed and created using various antenna designs to assess their effectiveness in generating and receiving EM waves when compared to experimental results. These simulation models are then subjected to testing using the established configuration, allowing for a meaningful comparative analysis.

The second task centers around understanding the behavior of EM waves through inhomogeneous mediums. The main purpose is to develop and validate a randomly distributed particle (RDP) modeling approach based on established principles and theories. Simulation models of EM waves through the inhomogeneous medium are created using the RDP approach. To verify the accuracy of the RDP approach, experiments are performed with aggregate specimens, and the results obtained from simulation modeling are compared with the outcomes of experimentation.

Throughout both tasks, a rigorous analytical approach is followed, employing tools such as numerical analysis and statistical analysis. These methods are instrumental in analyzing the data gathered from experimentation and simulation modeling. The insights gained from this comprehensive analysis will allow for meaningful conclusions and valuable recommendations based on the findings of the study. Ultimately, the study aims to contribute to the broader understanding of EM waves and their interactions with antenna designs and inhomogeneous mediums, potentially opening new avenues for future research and practical applications.

## 3.2 Analytical model

### 3.2.1 Antenna source modeling

In this study, various model parametric values were simulated to validate the accuracy of the input source, and their outcomes were compared with the experimental responses, as illustrated in Table 3.1. The evaluation primarily focused on energy and travel time, considering the medium's boundaries and metal reflection at the zero crossing before each peak reflection. The key emphasis of the investigation was to observe the time and signal attenuation within the medium, rather than the response of the initial direct wave. Consequently, only the reflected waves between the metal and the medium, encompassing air and aggregate medium, were taken into account. The boundary of the medium was defined using a metal plate as a reference. To determine the peak and low values within the specified time interval range, the Akaike information criterion (AIC) was utilized on the signal response data to identify the zero crossing intersections. The energy of each signal was derived from the area between the time intervals of medium and metal reflection, while travel time was calculated based on the time difference between the medium and metal reflection.

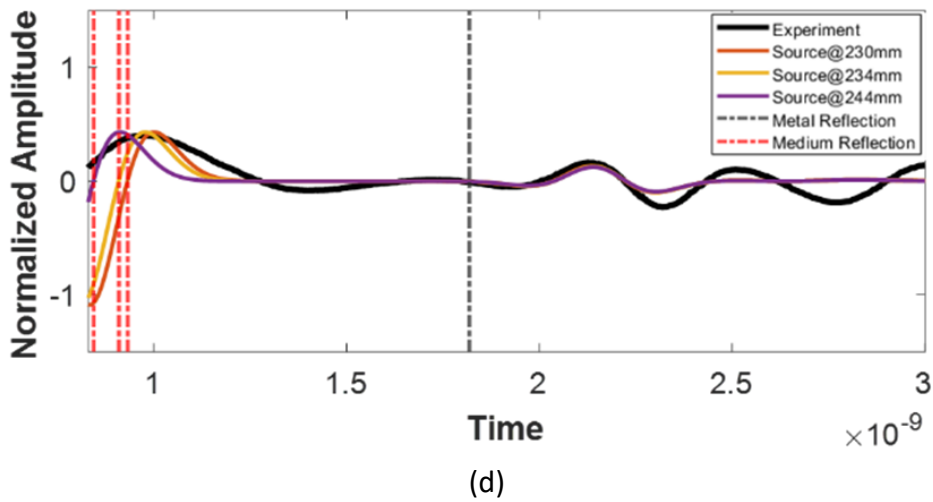
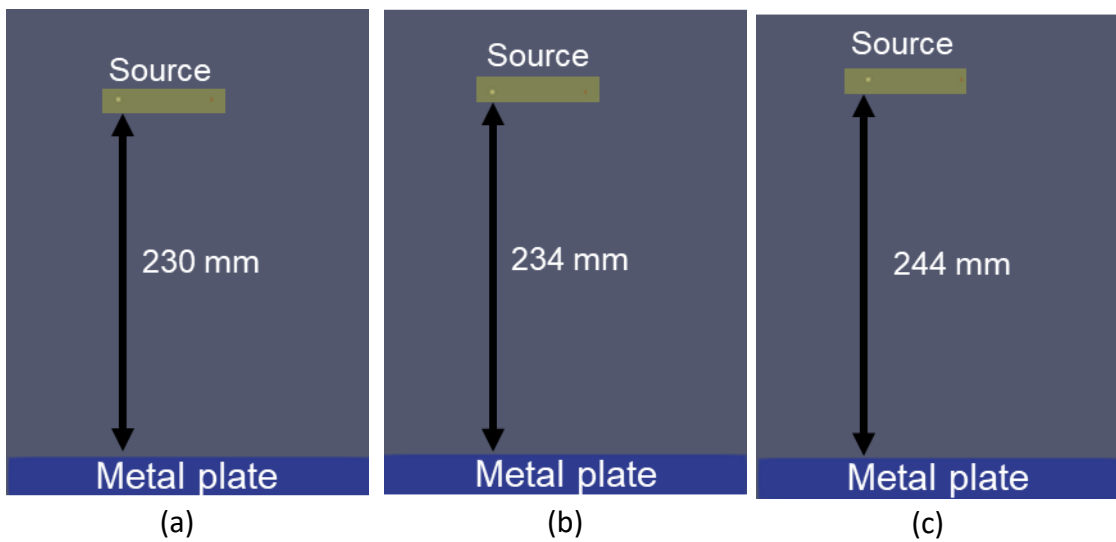
**Table 3.1. Parametric variable considered parametric antenna model design.**

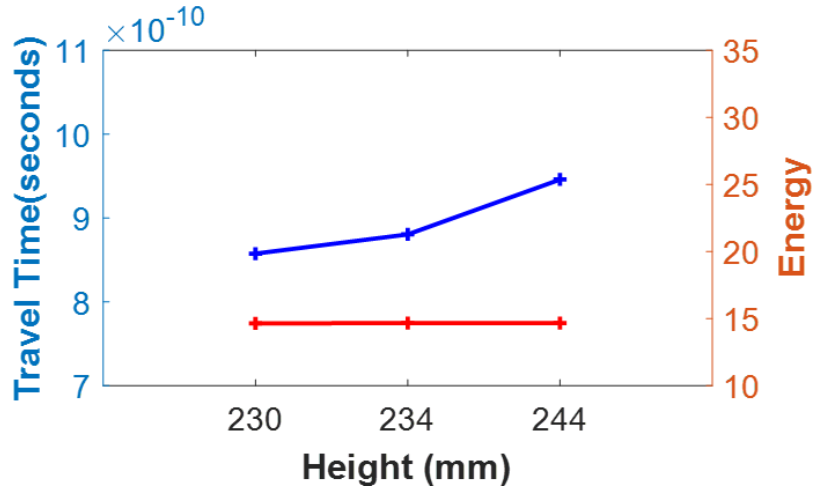
Parameter	Value
Time window	$4 \times 10^{-9}$ seconds
Domain (x, y, z)	0.5 x 0.5 x 0.7 m
Spatial resolution (x, y, z)	0.002 x 0.002 x 0.002 m
Height (above the medium)	0-14 mm (with medium 230-244 mm)
High density polyethylene with Dielectric Constant	3-15
Thickness of the HDPE/PCB	4-8mm

The purpose was to investigate the response of EM waves under different parameters to understand their effects and variability with each antenna design component. The results obtained from these simulation (Table 3.1) are presented in Figure 3.1, 3.2 and 3.3. Figure 3.1 illustrates a comparison between the experimental response (represented in black) and the antenna setup, considering only the transmitter and



receiver at different heights through an air medium with a depth of 230 mm (9 inches). The study aimed to observe the effect of variable height (0-14 mm) on travel time and energy attenuation. The energy attenuation is measured from the sum of the signal window. The center line in black indicates the boundary between the air medium and the metal plate. The results revealed that an increase in height led to a corresponding increase in travel time, while the energy attenuation remained relatively constant. These findings highlight the significance of the transmitter and receiver height as a crucial factor influencing the travel time of EM waves. Consequently, this factor should be taken into consideration in the design of antenna systems.





(e)

**Figure 3.1.** *The simulation setup progresses from (a) to (c), representing variable heights (230-244 mm). (d) The wave responses corresponding to these variable heights and (e) the parameter study of the variable height indicates an increase in travel time along with consistent energy levels.*

Figure 3.2 was dedicated to investigating the impact of various dielectric parameters on the travel time and energy attenuation of EM waves. To achieve this, the transmitter and receiver were positioned over a high-density polyethylene (HDPE) plate with different dielectric constants, while maintaining a constant depth of 230 mm. The study revealed that an increase in the dielectric constant of HDPE had little effect on the travel time, while the energy attenuation reduced when higher dielectric constants were considered. Moreover, different antenna heights were considered to align with the start of the medium.

In Figure 3.3 examined the impact of plate thickness variation for both HDPE and printed circuit board (PCB). The results demonstrated that an increase in plate thickness resulted in a corresponding increase in travel time, while the energy attenuation remained relatively constant. This finding highlights the significance of plate thickness as an important factor influencing the travel time of EM waves, and it should be taken into consideration during the design of antenna systems.

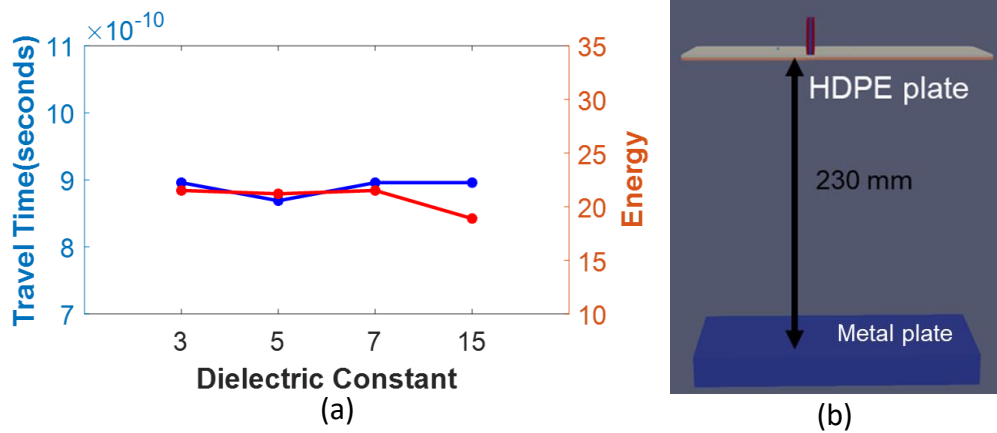


Figure 3.2. Simulation parameter analysis: (a) illustrates the arrangement for varying dielectric constants (3-15), with sensors placed above and a high-density polyethylene plate below. (b) The parameter study of the variable dielectric constant) reveals consistent travel time and energy characteristics.

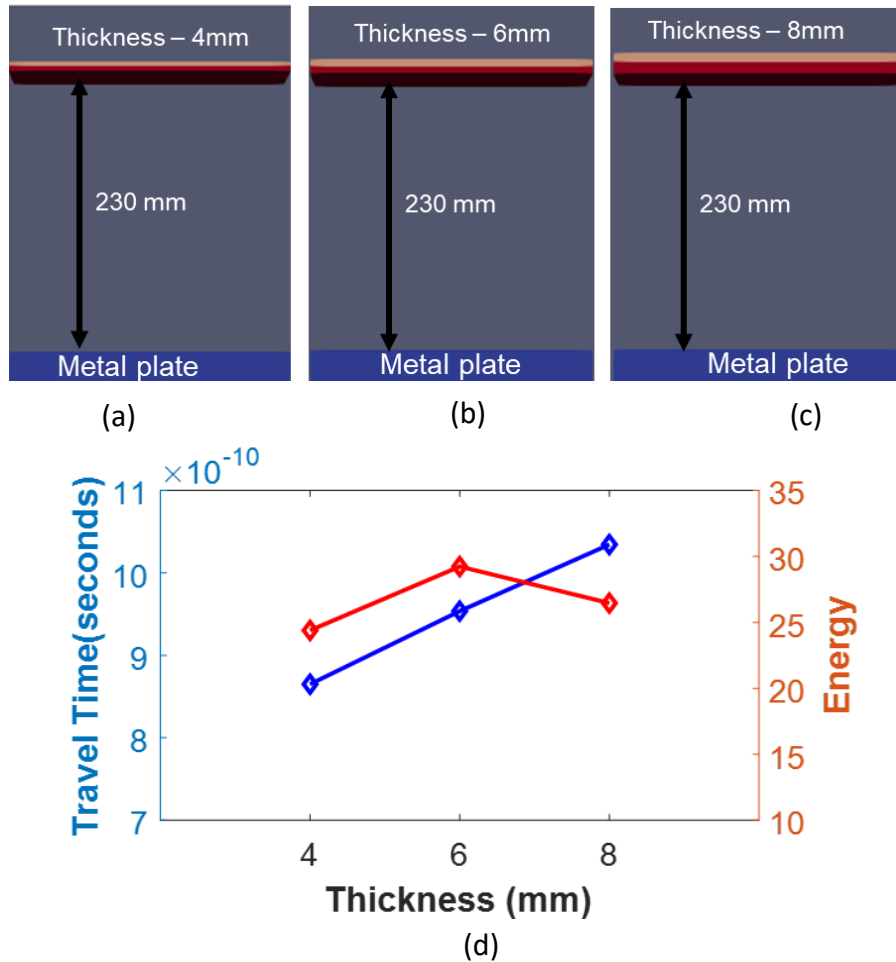


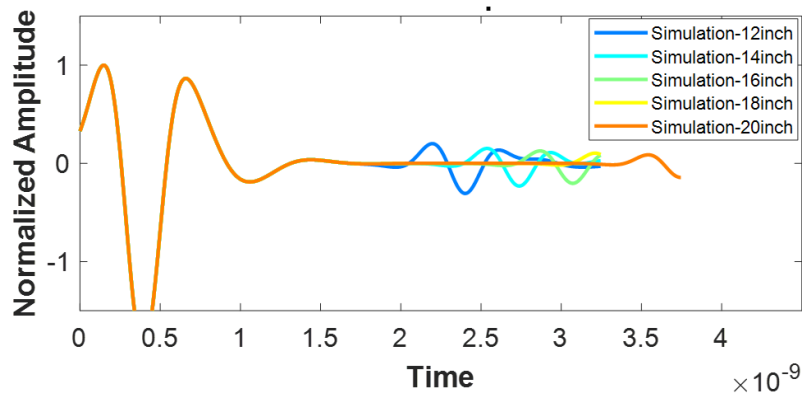
Figure 3.3. Simulation parameter analysis: (a) to (c) for variable thickness (4-8 mm) considering printed circuit board and high-density polyethylene plate below the sensors. (d) parameter study of variable thickness (e) showing increasing travel time energy.

The parameter studies conducted in this study have demonstrated that a simple source and transmitter are insufficient to accurately represent a GPR signal response. Instead, it is crucial to consider the structure of the antenna module. For this purpose, the internal components of the antenna module were examined from a cross-sectional perspective (Warren, 2011) with the antenna model confined between plastic HDPE plates, as illustrated in Figure 3.6. To enhance the accuracy of the model, absorbers and a perfect electric conductor were also incorporated.

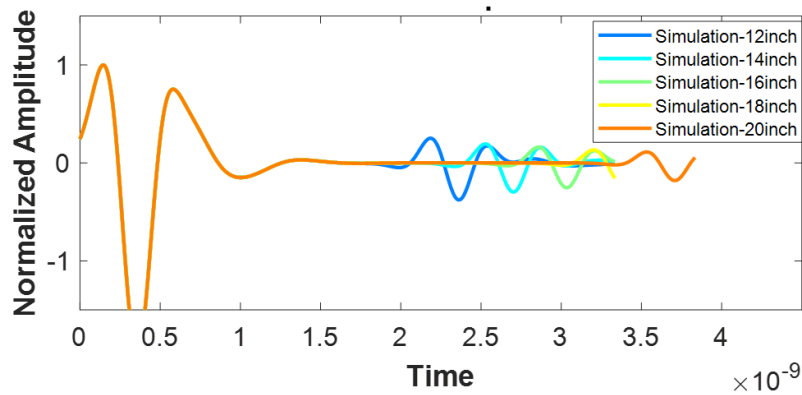
These internal components were integrated into the antenna model for the 1120, 1300, and 1600 MHz frequencies, in combination with the parameter studies shown in Figure 3.4 and 3.5. The resulting wave response closely resembled the experimental response observed between the medium and metal reflections for the 1600 MHz frequency source, as depicted in Figure 3.13. To determine the appropriate thickness, dielectric constant, and conductivity of these internal components, several simulations were conducted, and their final values for the antenna design setup are detailed in Table 2. The inclusion of these internal components significantly improved the accuracy and fidelity of the antenna model, enabling a more comprehensive representation of GPR signal responses.

***Table 3.2. Parameter values of the antenna model obtained after several simulations.***

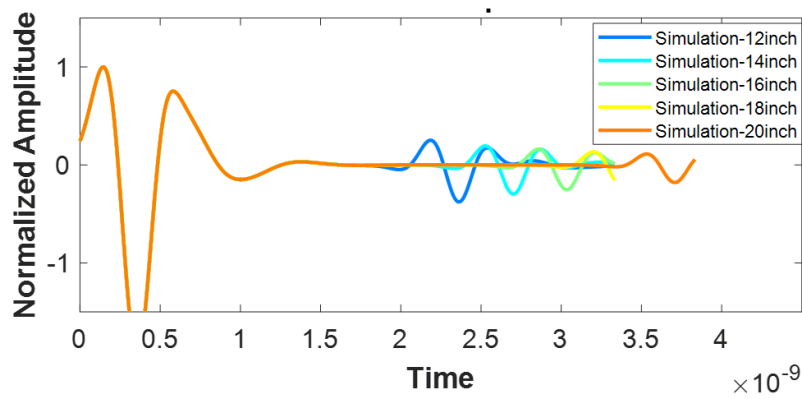
Material	Dielectric constant	Conductivity
High density polyethylene	2.35	0
Absorber 1	3	0
Absorber 2	1.58	0.628
PCB	3	0



(a)

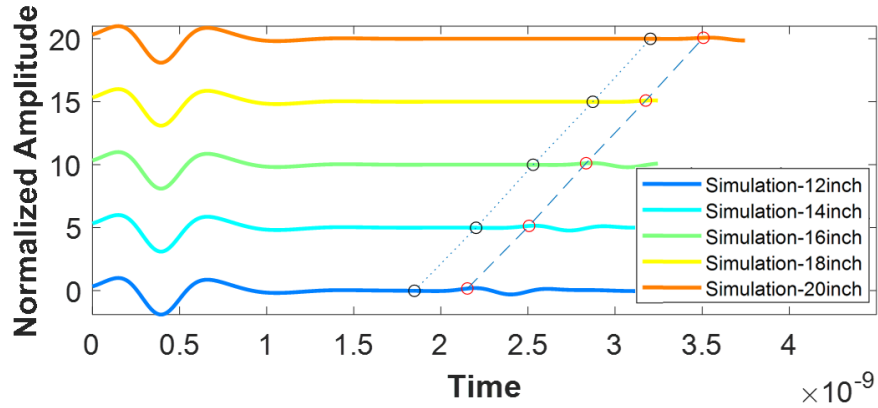


(b)

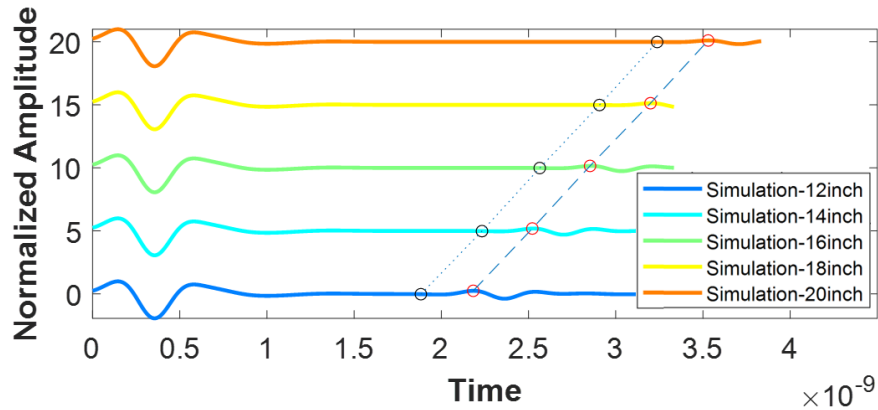


(c)

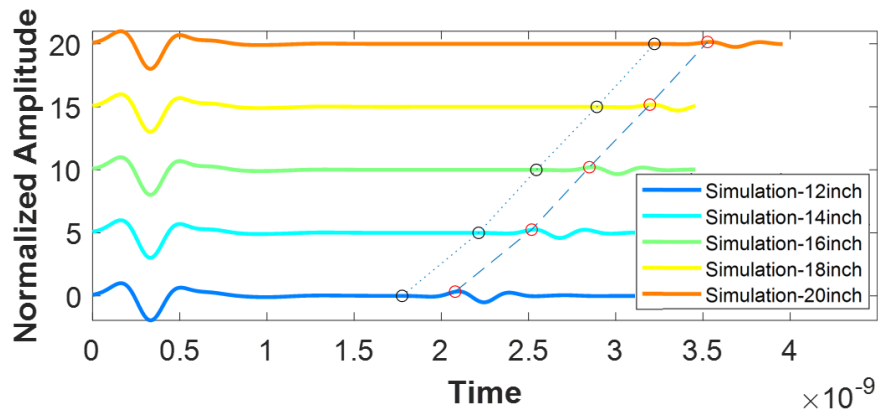
**Figure 3.4. Data comparison of wave response analysis in air at different depths (12-20 inches or 305-506 mm) for simulations with different frequency sources: (a) 1120MHz, (b) 1300MHz, and (c) 1600MHz.**



(a)

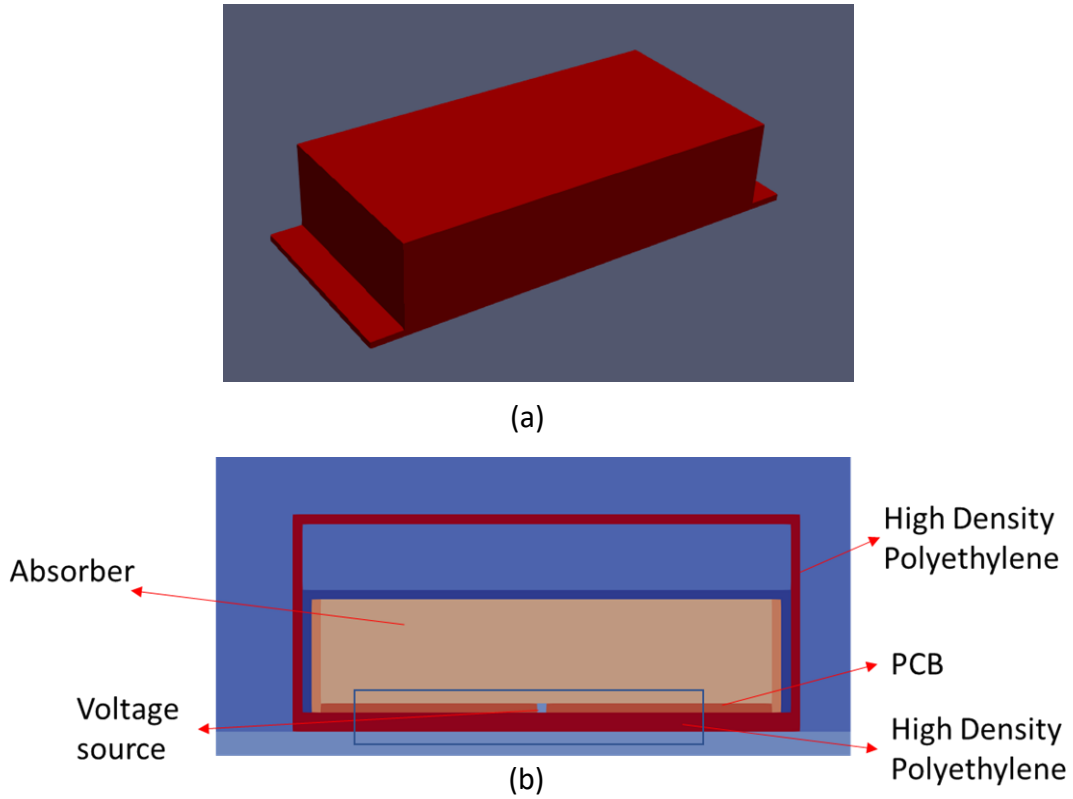


(b)



(c)

**Figure 3.5. Waterfall plots for peak amplitude and boundary of metal reflection at different depths (12-20 inches or 305-506 mm) for simulations with different frequency sources: (a) 1120MHz, (b) 1300MHz, and (c) 1600MHz.**



*Figure 3.6. Designed antenna model: (a) perspective view, (b) cross-section along the transmitter showing a detailed view.*

### 3.2.2 Random scattering of particle for inhomogeneous medium

To achieve a random distribution of particles without overlap, a Python code was developed to determine the 3D locations of the particles. Initially, equally spaced particles were modeled with the Python code using the Eq.3.1-**Error! Reference source not found.** to understand the pattern and location. The number of spherical particles is calculated by:

$$Nr_x = \frac{L}{r}, Nr_y = \frac{B}{r}, Nr_z = \frac{H}{r}, \quad 3.1$$

Where  $Nr_x$ ,  $Nr_y$  and  $Nr_z$  represent the counts of spherical particles along the dimensions of length (L), breadth (B) and height (H) of the model, respectively. The coordinates for these spherical particles are computed using:

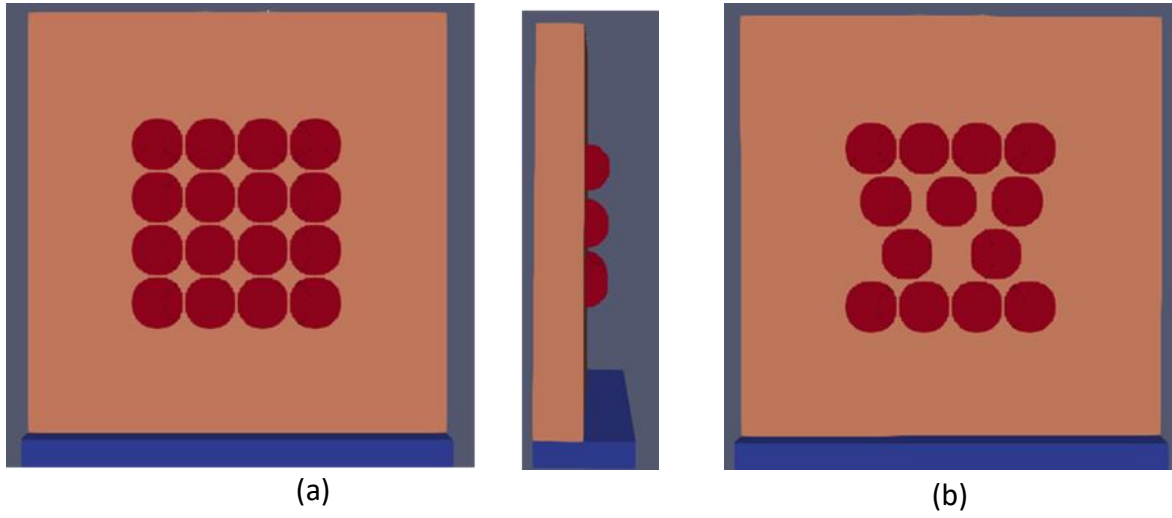
$$x = \begin{cases} L + (2 \cdot ((Nr_x/2) - i) + 1) \cdot r, & i \leq (Nr_x/2) \\ L - (2 \cdot (i - (Nr_x/2)) + 1) \cdot r, & i > (Nr_x/2) \end{cases}$$

3.2

$$y = B - (2 \cdot j - 1) \cdot r,$$

$$z = \begin{cases} H - (2 \cdot (k - (Nr_z/2)) + 1) \cdot r, & k \leq (Nr_z/2) \\ H + (2 \cdot ((Nr_z/2) - k) + 1) \cdot r, & k > (Nr_z/2) \end{cases}$$

where x, y and z are the coordinates in the 3D axis based on a given radius (r).



**Figure 3.7. Simulation models of particle distribution algorithms: (a) equally spaced particles in a single plane and (b) variable patterns in a single plane.**

To achieve a random distribution of particles, the percentage of the total volume is taken into account as shown in Eq. 3.3 to determine the number of particles to be randomly placed in the model, with a tolerance distance between each particle. Once the tolerance distance is maintained, the respective particle sphere is added to the input file and the volume of the particle is reduced accordingly. An example of randomly distributed particles is shown in Figure 3.8. Percentage of the volume occupied by the particle ( $V_{per}$ ) and volume of each particle ( $V_p$ ) are calculated by:

$$V_{per} = Percentage \cdot l \cdot b \cdot \frac{h}{100}, \quad 3.3$$

$$V_p = \frac{4}{3} \pi r^3, \quad 3.4$$



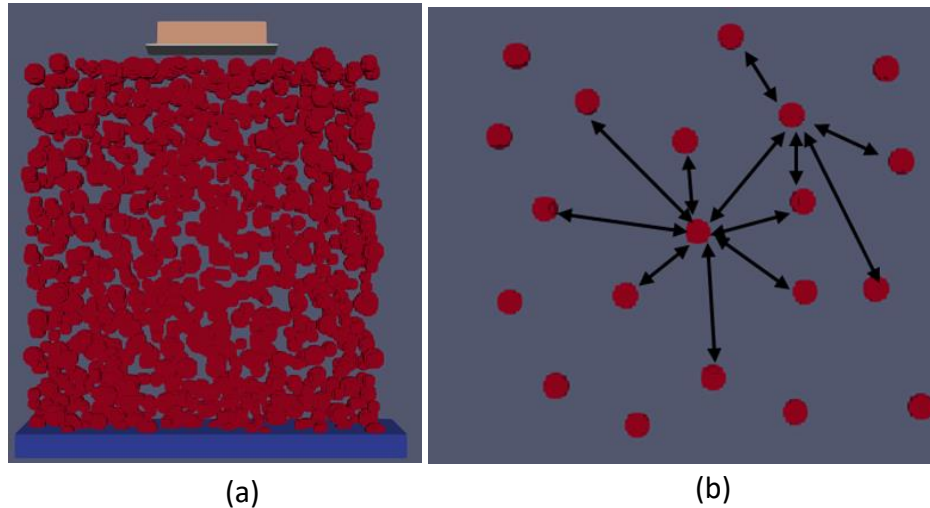
where  $l$ ,  $b$  and  $h$  are the dimension of the model and  $r$  is the radius of the particle. The distance between each particle is calculated by:

$$d_j = \sqrt{(x_i - x)^2 + (y_i - y)^2 + (z_i - z)^2} - 2r, \quad 3.5$$

where  $x$ ,  $y$  and  $z$  represent randomly generated coordinates within a defined range between  $(x_l, y_l, z_l)$  and  $(x_u, y_u, z_u)$ . For each set of these newly generated random coordinates, their distance ( $d_j$ ) from previously generated coordinates is examined to ensure it meets a specified tolerance. If the condition is met, these coordinates contribute to a non-overlapping random distribution of particles. This process continues iteratively until the total assigned volume reaches zero. The percentage of the particle occupied is reduced by:

$$V_{per} = V_{per} - V_p. \quad 3.6$$

The random particle experiment was conducted at three different depths 305, 356 and 405 mm (12, 14, and 16 inches) with two aggregate sieve size ranges from 12-25mm and 25-50mm (0.5-1 inch and 1-2 inches) as shown in Figure 3.15. The comparison will be discussed in Section 3.3.



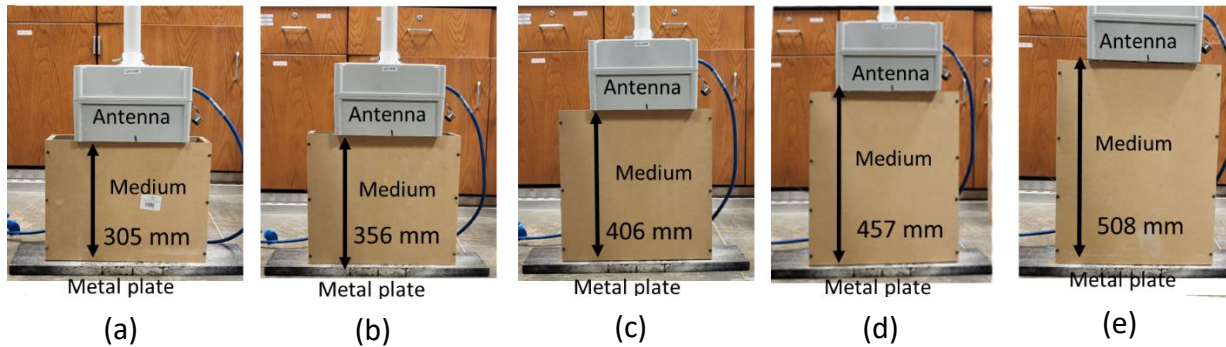
**Figure 3.8. Simulation model with (a) randomly distributed particles developed from the above algorithm. upon zooming in, (b) detailed aggregate model considering tolerance for aggregate positions becomes visible.**

### 3.3 Verification

#### 3.3.1 Antenna model

To accurately simulate wave propagation, careful consideration of the input sources used in the simulation is essential. As a result, various input source signals were studied in different setups and locations. These signals were cross verified with a reference signal obtained from a 1600MHz antenna over an air medium. Nevertheless, achieving an exact or even a similar match between the FDTD signal and the experimental signal presents a challenging task. To tackle this challenge, the study focuses on obtaining a signal match within the wave propagating medium.

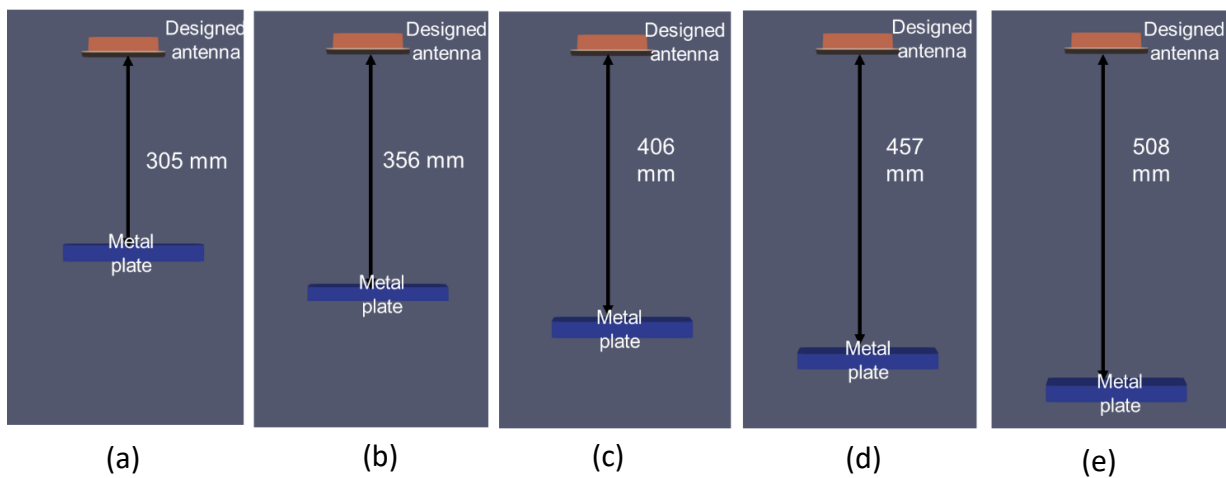
To validate the antenna model under varying conditions, simulations were conducted at different depths of the air medium with a metal reference plate placed below each depth. EM waves were propagated through the experimental setups at depths of 305, 356, 406, 457, and 508 mm (12, 14, 16, 18, and 20 inches), as depicted in Figure 3.8. FDTD antenna models were also simulated for the experimental frequency of 1600MHz to examine the effects of antenna and signal variability.



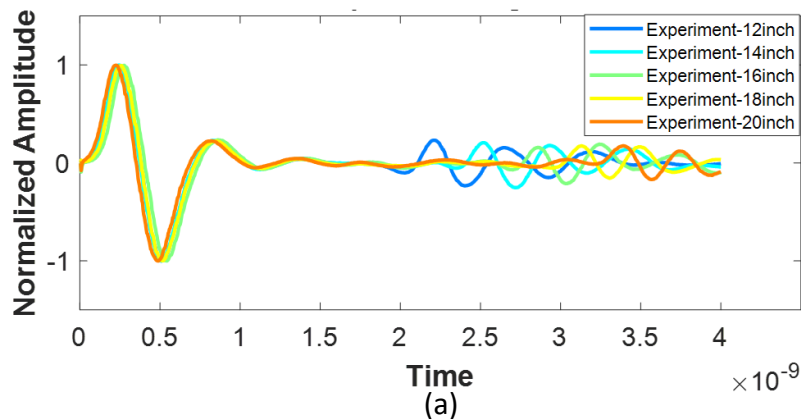
**Figure 3.9. Experimental setup for scanning antenna at multiple depths: (a) 305mm (12 inches), (b) 356mm (14 inches), (c) 406mm (16 inches), (d) 457 mm (18 inches), and (e) 508 mm (20 inches).**

To validate the accuracy of the designed antenna, simulation models were created with varying depths of the air medium, ranging from 305 mm to 506 mm (12 inches to 20 inches), as shown in Figure 3.10. Similar experimental setups were performed to analyze the wave response of different depths of the air medium, as depicted in Figure 3.9. The wave response of the experimental and simulation antenna designs is shown in

Figure 3.11 (a) and 3.12 (a). In both cases, a delay in arrival time and reduction in amplitude were observed. In the waterfall plot of Figure 3.11 (b) and 3.12 (b), the dotted line connects the arrival time of the metal plate, and the metal reflection peaks, and the slope of these lines indicates velocity change due to varying depth. On comparing the experiment and simulation slope lines (Figure 3.13), the trend is similar and overlapping, indicating that the current antenna model design is highly accurate for signal analysis. This demonstrates the reliability and precision of the designed antenna model across different depths of the air medium.



**Figure 3.10. Simulation of the designed antenna at various depths: (a) 305mm (12 inches), (b) 356mm (14 inches), (c) 406mm (16 inches), (d) 457 mm (18 inches), and (e) 508 mm (20 inches).**



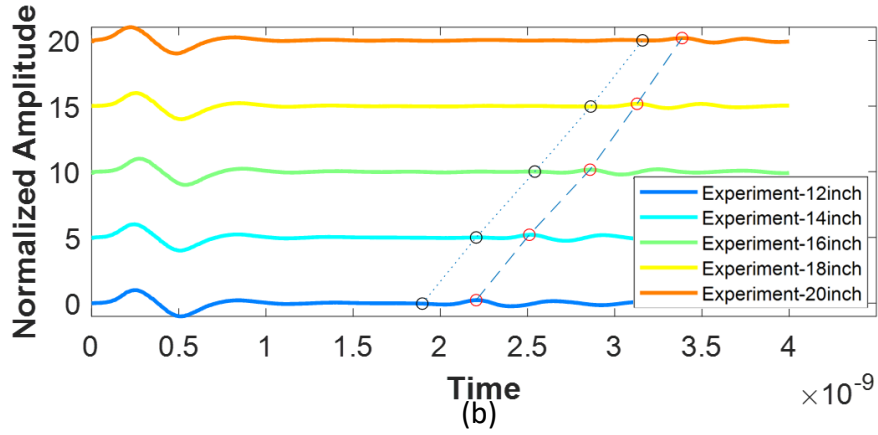


Figure 3.11. Wave response analysis in air: (a) different depths (305-506mm) for experiment and (b) waterfall plots for peak amplitude and boundary of metal reflection from experiment.

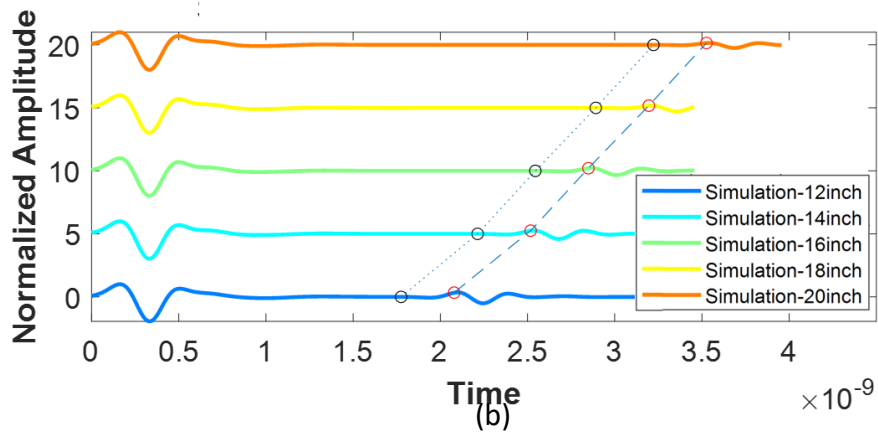
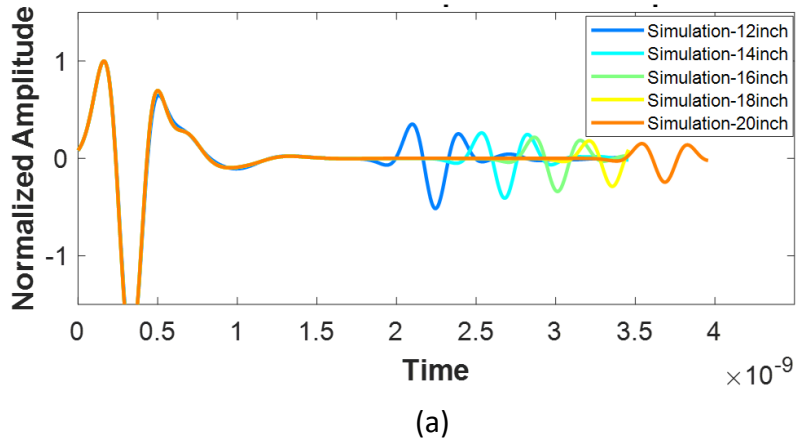
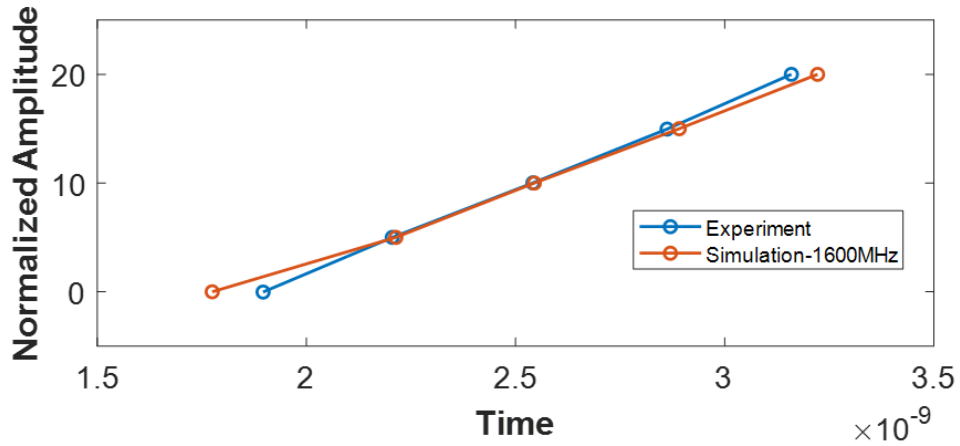
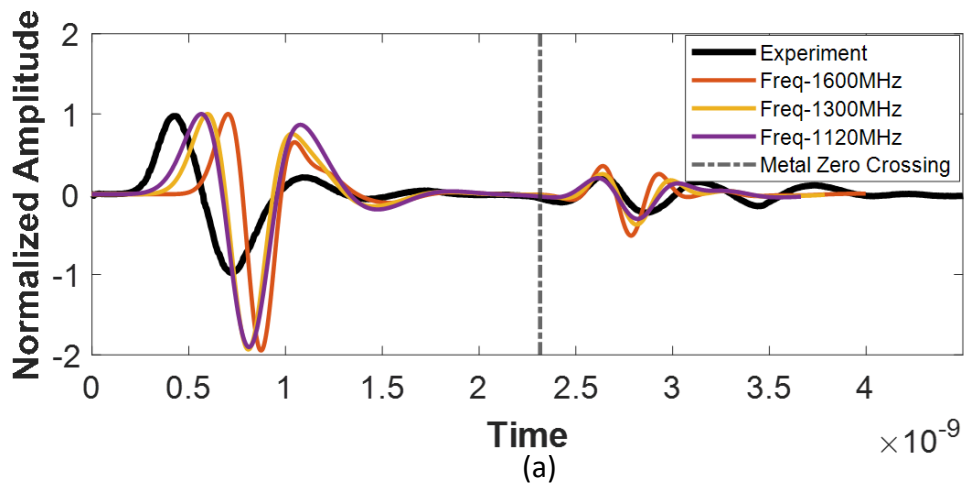


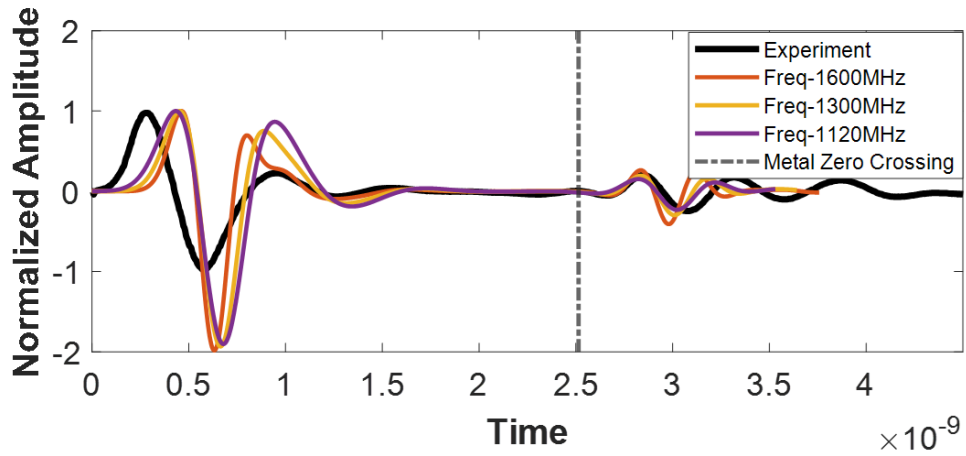
Figure 3.12. Wave response analysis in air: (a) different depths (305-506mm) for simulation and (b) waterfall plots for peak amplitude and boundary of metal reflection from simulation.



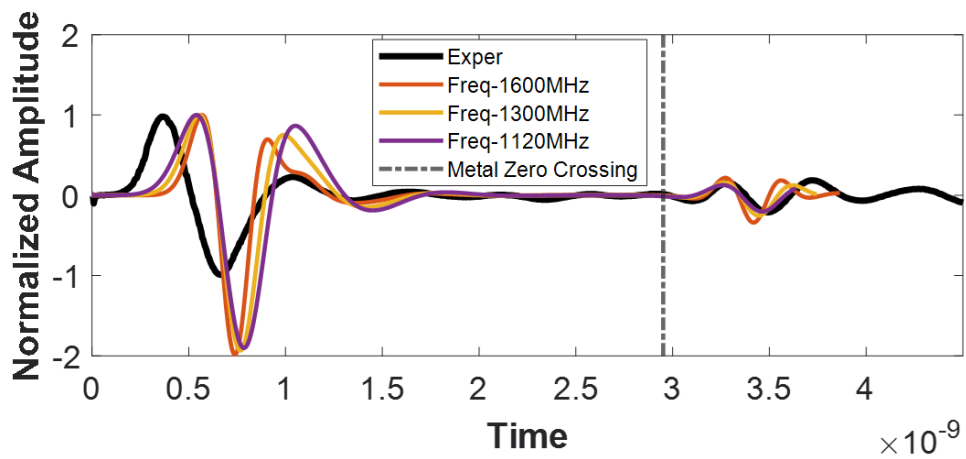
**Figure 3.13. Comparison of slope lines similarity between simulation and experiment**

Further verification for the antenna model was conducted by comparing different depths of the air medium experimentally and numerically in Figure 3.14. The simulation results demonstrated that the 1600MHz frequency performed optimally in all the depths, with a clear start of the air medium observed near 1ns, which closely resembled the experimental results. In Figure 3.14 the dashed line indicates the beginning of the metal surface medium.

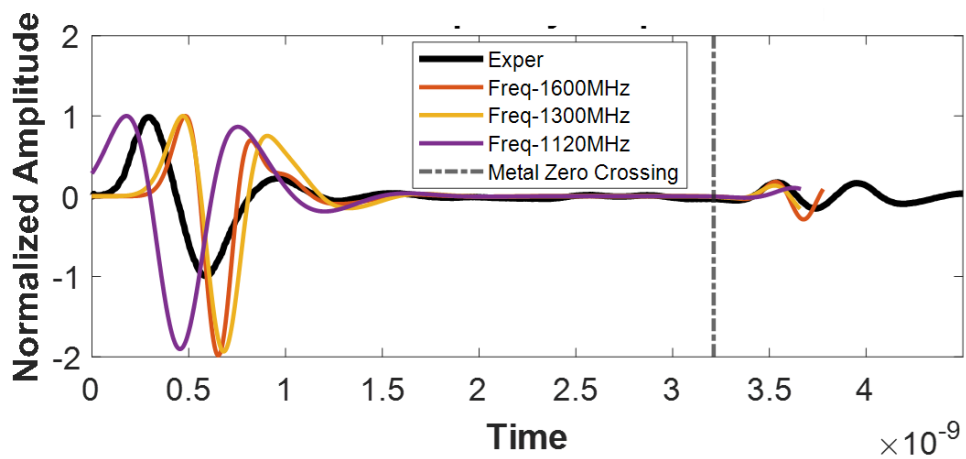




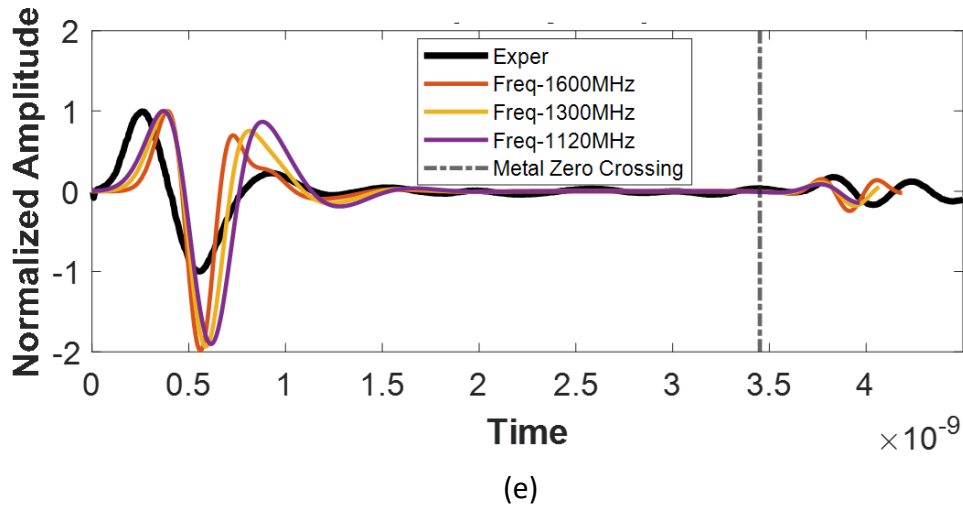
(b)



(c)



(d)



**Figure 3.14. Antenna model parameter study with different depth: (a) 12-inches (b) 14-inches (c) 16-inches (d) 18 inches and (e) 20 inches with different frequency (1120 MHz, 1300MHz & 1600MHz). The dashed line corresponds to the wave response at the start of the metal surface medium.**

### 3.3.2 Radom aggregate model

The experimental setup for testing the inhomogeneous aggregate-void medium is depicted in Figure 3, and it was conducted at three different depths, namely 305 mm, 356 mm, and 406 mm. To enhance the accuracy of the simulation, two different aggregate sizes of 12-25 mm and 25-50 mm, obtained from sieve analysis, were considered.

As the depth increases, the arrival time of the experimental wave responses (Figure 3.16) shows a delay in the wooden plate reflection. The red and blue dots correspond to the amplitude reflection from the metal plate and the initiation of the metal surface medium. Given the inhomogeneous nature of the medium, multiple wave response scans were recorded at five different locations for each setup. The arrival times of these different locations are presented as scatter plots in Figure 3.17, along with the average line connecting each depth. These observations provide valuable insights into the behavior of the inhomogeneous medium and validate the reliability of the simulation model.

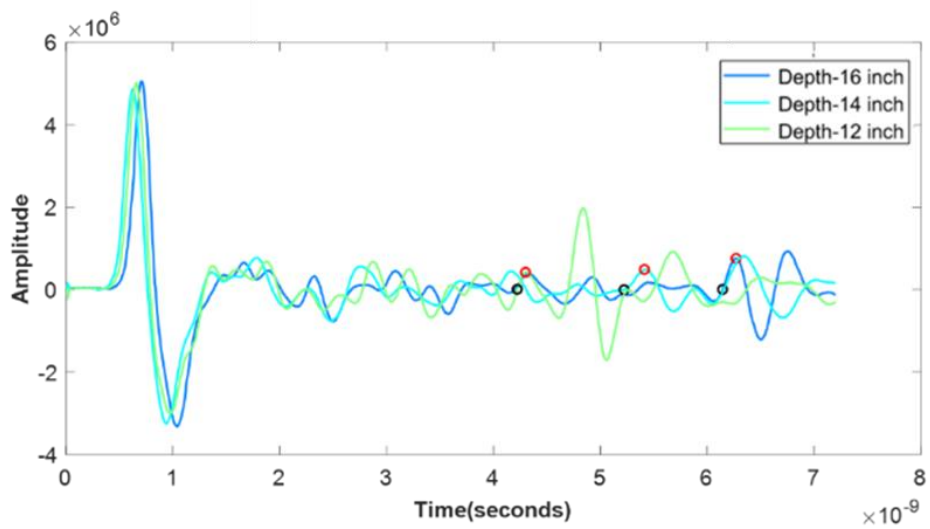


(a)



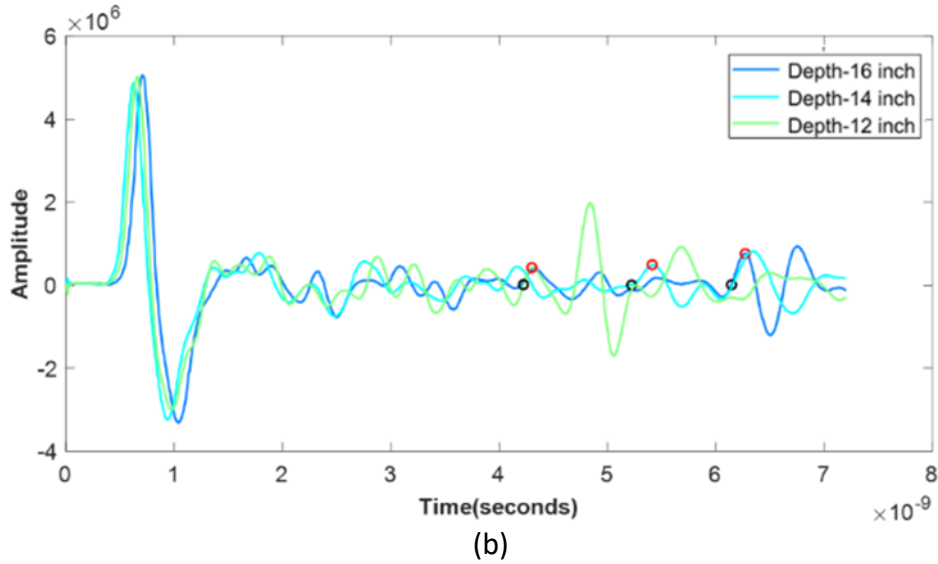
(b)

**Figure 3.15.** Experimental setup (a) for testing varying depth with (b) two different types of aggregates of sizes 12-25 mm(left) and 25-50 mm(right).

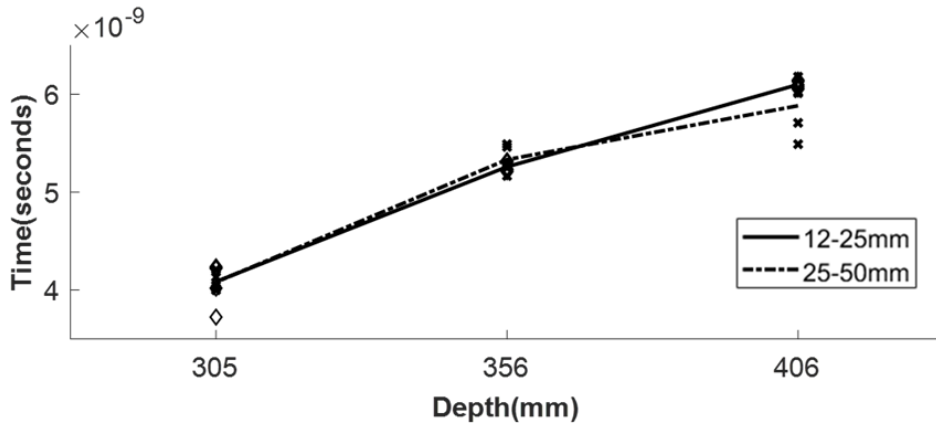


(a)



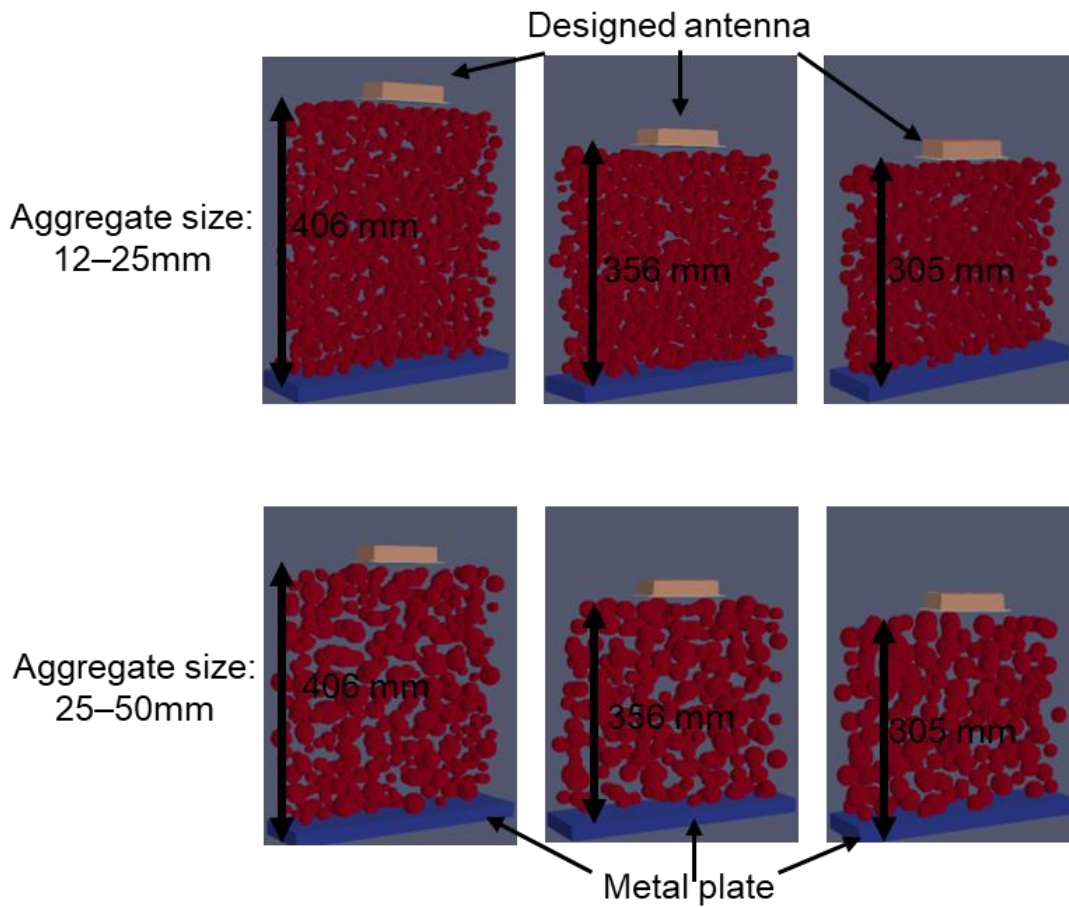


**Figure 3.16.** Experimental wave responses result of the different size of aggregates (a) 12-25 mm and (b) 25-50 mm at three different depths. The arrival time (blue dot) from the metal surface medium is used for comparison with simulation models.

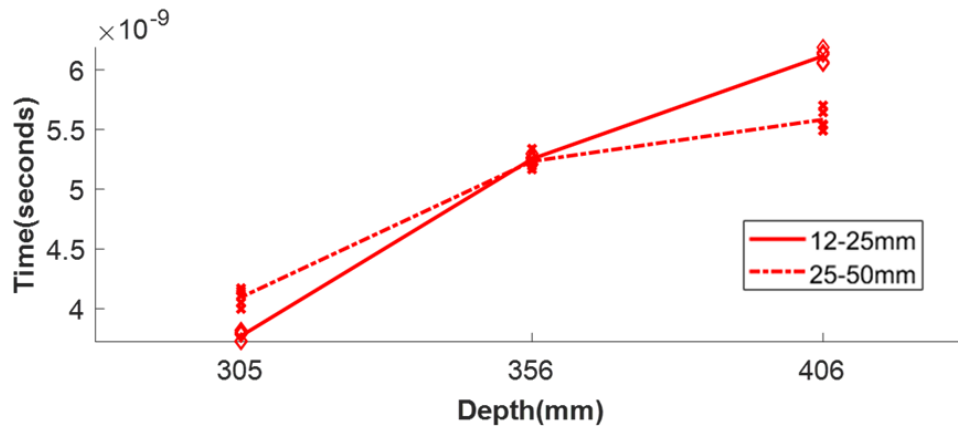


**Figure 3.17.** Scatter plot of the arrival time in experimental results for two different sizes of aggregates.

The simulation model was analyzed under the identical conditions as the experimental setup, as illustrated in Figure 3.15. The simulation of the inhomogeneous medium was accomplished by modeling randomly generated aggregate particles using Python. The analysis was performed for three different depths: 305 mm, 356 mm, and 406 mm, as depicted in Figure 3.18. The particles considered for this simulation were aggregates with a known dielectric constant of 4.2, as evaluated from the experiment. Remarkably, similar to the experimental results, the simulation wave response exhibited a linear trend (Figure 3.19) when plotting the arrival time for the three different depths of both aggregate sizes.



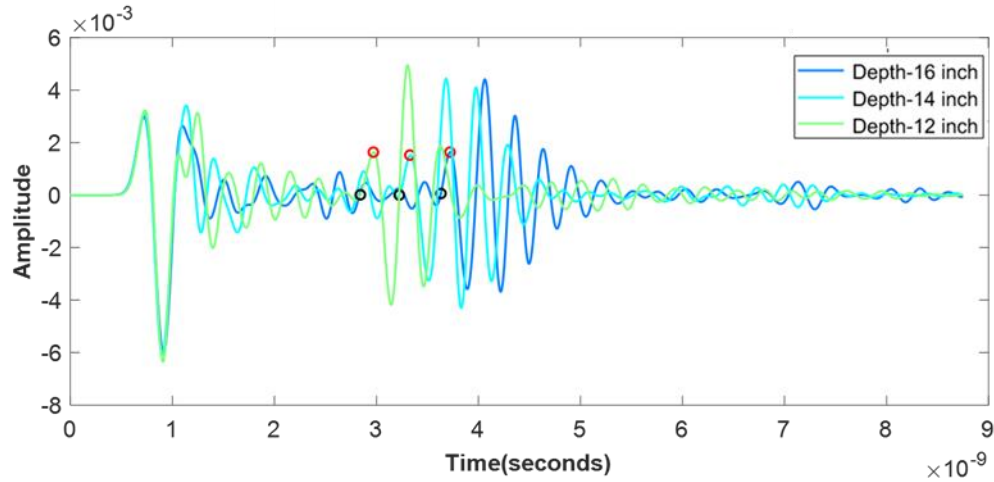
*Figure 3.18. Inhomogeneous simulation model generated from random aggregate particles for different depths with two different aggregate sizes.*



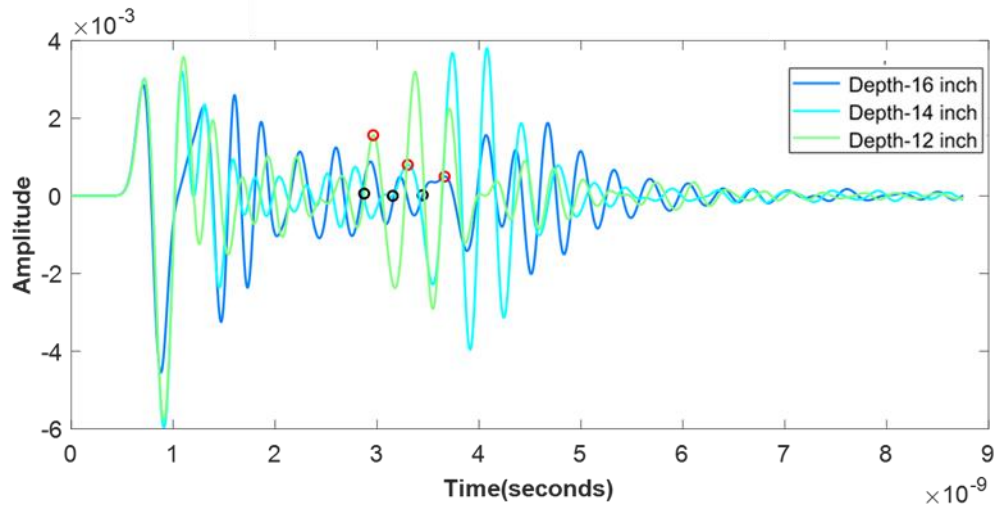
*Figure 3.19. Scatter plot of the arrival time in simulation results for two different sizes of aggregates.*

Upon comparing the wave response results of the random particle simulation (Figure 3.20) with the experimental study (Figure 3.16) for different sizes of aggregates, a similar trend is observed. However,

there is a delay in the arrival time at each depth due to the random distribution of the aggregate model and the variability in sizes (Figure 3.21). This correspondence between the experimental and simulation outcomes reinforces the credibility and effectiveness of the simulation model in accurately capturing the behavior of the inhomogeneous medium. The red and blue dots correspond to the amplitude reflection from the metal plate and the initiation of the metal surface medium.

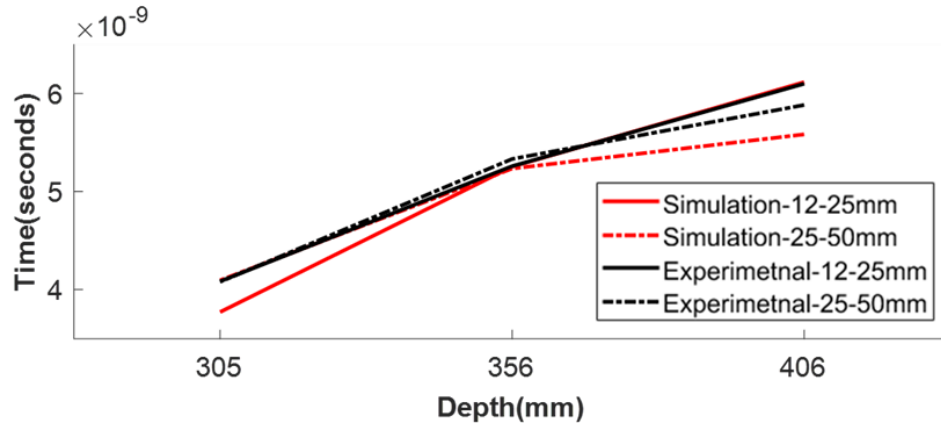


(a)



(b)

**Figure 3.20. Simulation wave responses results of the different size of aggregates (a) 12-25 mm and (b) 25-50 mm at three different depths. The arrival time (blue dot) from the metal surface medium is used for comparison with experimental.**



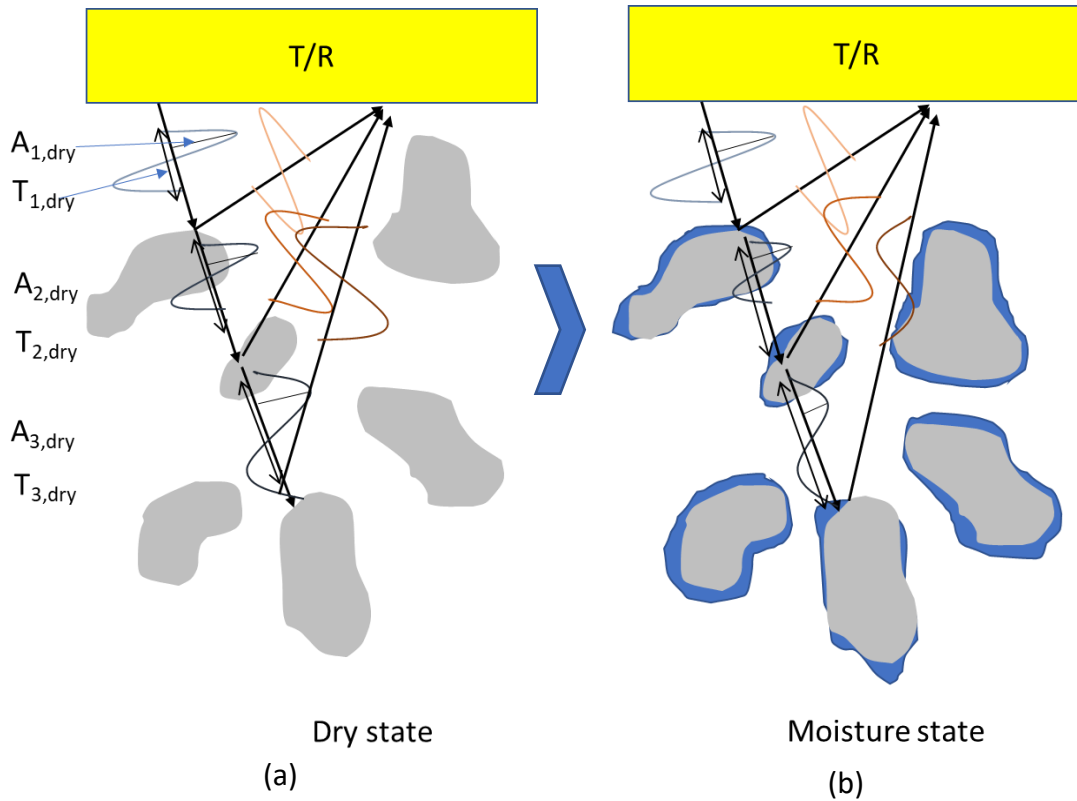
*Figure 3.21. Comparison of time variation at different depths between simulation and experiment depth*

## CHAPTER 4 MOISTURE STUDY

### 4.1 Motivations

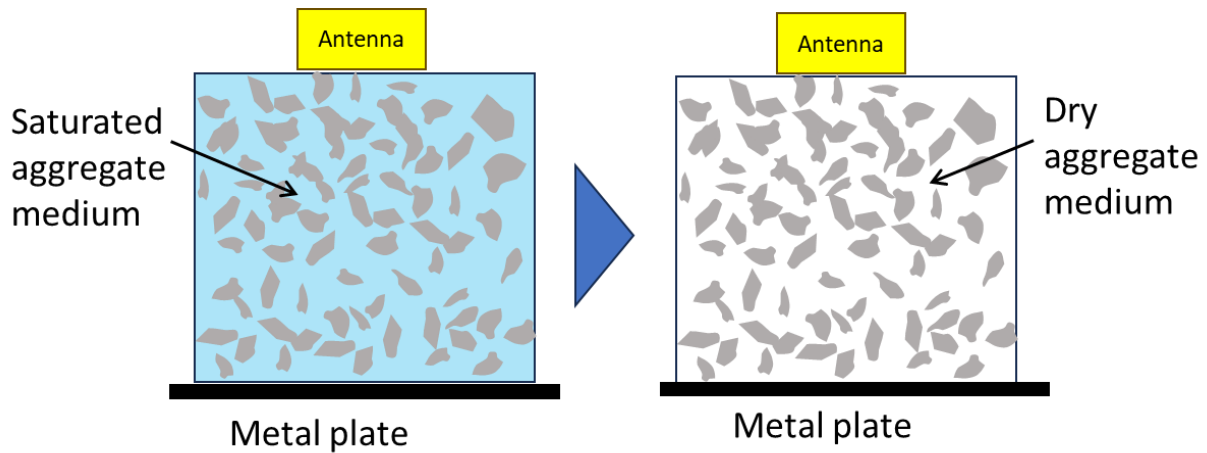
The first objective of this dissertation is to investigate the impact of moisture within inhomogeneous mediums, such as concrete or multiple layers of materials. As highlighted in the background, moisture can give rise to issues such as asphalt stripping, soil erosion in subgrade materials, and an accelerated corrosion process. The examination of existing literature revealed notable effects of moisture on EM waves, including amplitude variation, time delays in metal plate reflections, and variations in positive-to-negative peak magnitudes.

The amplitude variation was found to increase as the medium transitioned from a saturated state to a dry condition (Hugenschmidt, 2008). Similarly, in the case of positive-to-negative peak magnitude variation, attenuation was observed to decrease with rising moisture levels (Patil, 2011). Regions with high rainfall or poor drainage are particularly susceptible to this issue. The stripped areas are vulnerable to further damage from moisture intrusion, which can cause more extensive deterioration, including cracking and potholes. Additionally, the reduction in structural integrity. investigations indicated that moisture presence within the medium could be detected through delays in arrival time concerning the metal plate (Ling, 2022). While some studies employed fast fourier transform (FFT) and short-time FFT analyses of EM waves, our research also incorporates full wave responses involving metal plate reflections for signal processing (Hong, 2014; Laurens, 2005).



**Figure 4.1. Illustration of the transmitted incident wave transformation in an inhomogeneous medium (a) with moisture and (b) without moisture, which in return affects the reflected wave by multiple scattering to the receiver.**

In practical radar scanning applications, the medium's response is often assessed without considering metal reflections. However, our study exclusively focuses on analyzing the medium's wave response for parameter analysis and signal processing. This study hypothesizes that the transmitted incident wave travels through the medium and undergoes attenuation. Additionally, when moisture is introduced, further energy loss is observed, as illustrated schematically in Figure 4.1. During experimental testing, the medium undergoes water saturation for 24-48 hours before testing initiation. The experimental tests involve a transition from a saturated state to a dry state, as depicted in Figure 4.2.



*Figure 4.2. Schematic illustration depicting the proposed experimental setup for transitioning from a saturated aggregate medium to a dry aggregate medium.*

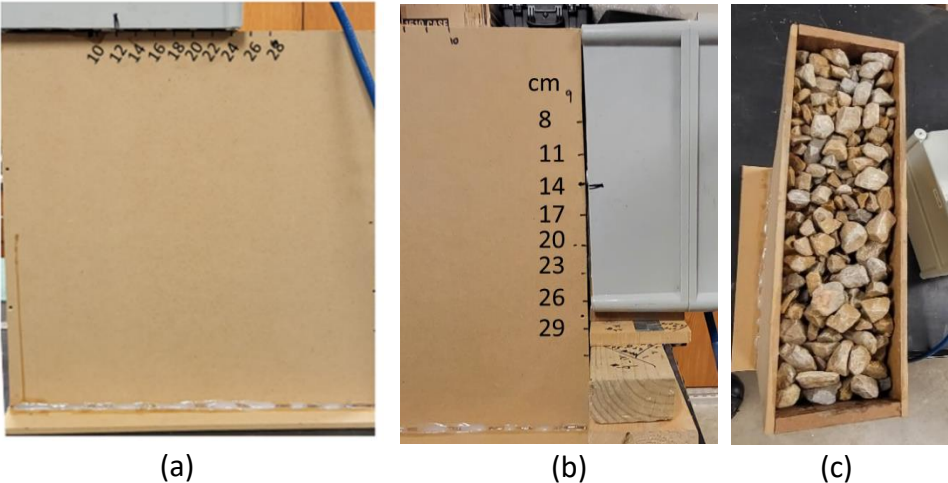
## 4.2 Moisture model investigation

### 4.2.1 Experimental

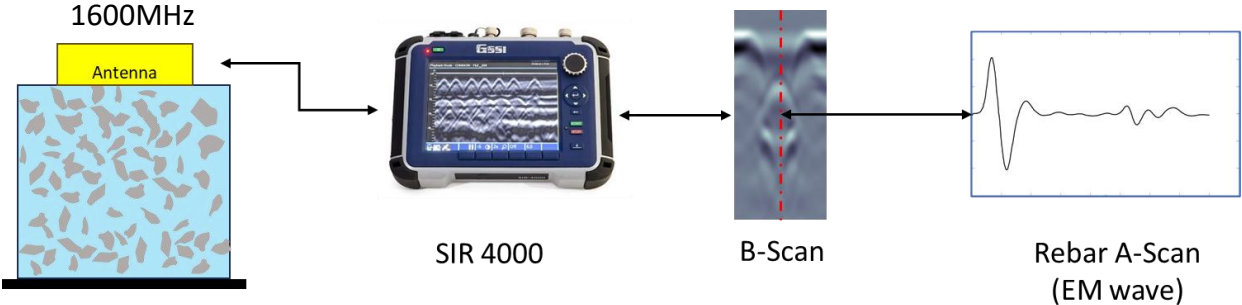
The experimental setup for studying the moisture effect comprises a wooden box measuring 4x16x16 inch<sup>3</sup>, filled with saturated aggregates, as depicted in Figure 4.3 (c). The inner side of the wooden box, where the saturated medium is located, is coated with a waterproof sealer. Regular measurement intervals are established on the top and sides of the wooden box for EM wave scan locations. The top surface is marked at 2 cm intervals (Figure 4.3 (a)), while the side surface is marked at 3 cm intervals (Figure 4.3 (b)).

The EM wave source for this experiment is a GSSI 1600MHz antenna coupled with an SIR 4000 acquisition system, as schematic shown in Figure 4.4. The experiment is conducted as a continuous 24-hour test run. EM wave scans are performed at each location on the top and sides every 30 minutes during the initial 6.5 hours, followed by hourly scans for the subsequent 16 hours, and finally, scans are conducted every 2 hours until the 24-hour mark. The primary objective is to observe the variation in EM wave responses as the medium transitions from a saturated state to a dry state. Additionally, the weight of the wooden box with aggregates is measured before each scan.

The side scan serves to corroborate the theory that the upper section of the aggregate undergoes more significant moisture evaporation when contrasted with the lower portion. This comprehensive setup enables a thorough investigation of the moisture effect on EM wave responses.



**Figure 4.3.** The experimental setup for moisture verification was performed on the (a) top surface and the (b) side surface to assess the evaporation effect. (c) Randomly saturated aggregate, where radar scans are attenuated.



**Figure 4.4.** Schematic representation of the data acquisition system, from the transmitted/received antenna to data processing.

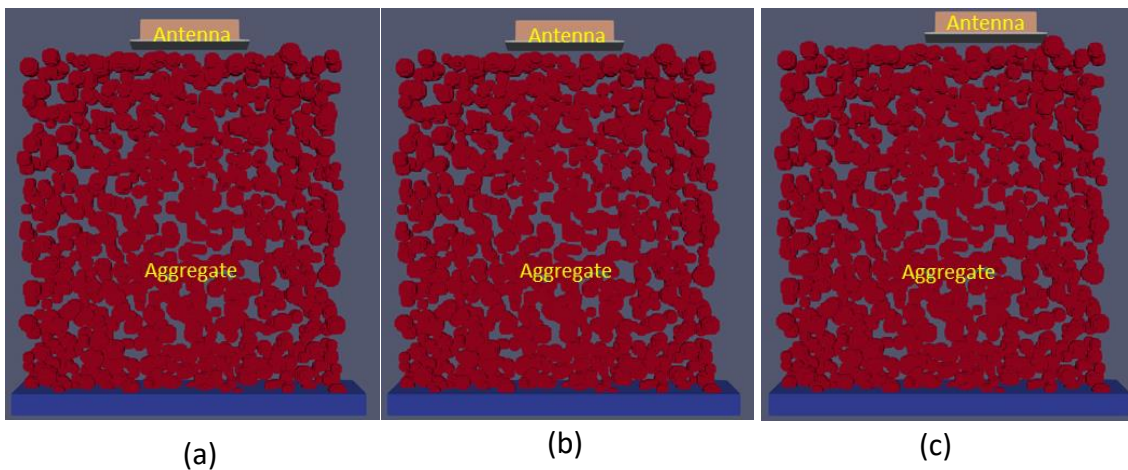
**4.2.2 Numerical simulation**

The randomly distributed aggregate developed in section 3.2.2 is employed for numerical simulations alongside the proposed antenna model, similar to the GSSI 1600MHz setup. Two types of moisture model



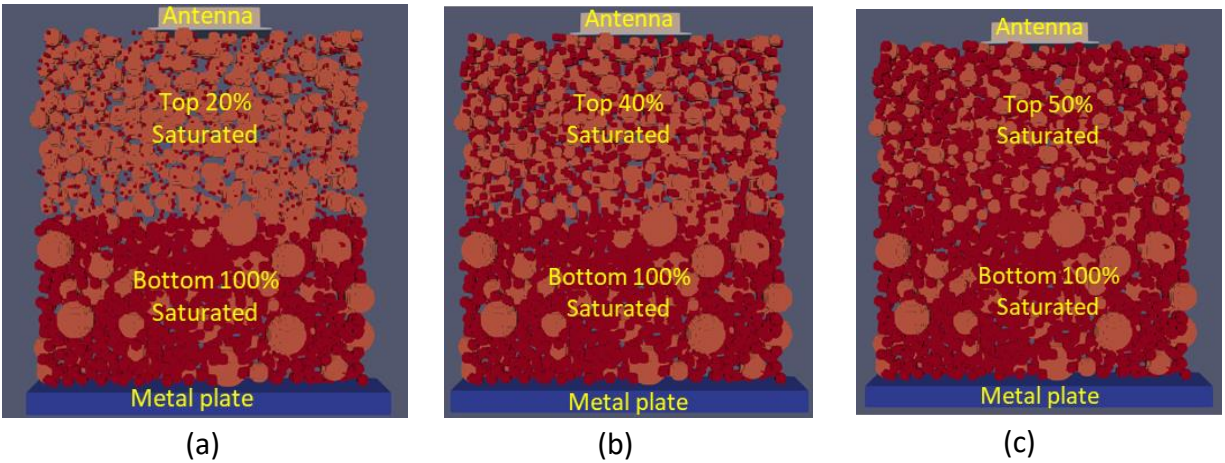
studies were conducted. In the first model, denoted as M1, the electromagnetic properties of the aggregate were altered by varying the conductivity parameter from 0 to 0.2 across the entire aggregate medium. Additionally, simulations were conducted at different scan locations to verify the similarity to the experimental top surface using the same aggregate pattern, as depicted in Figure 4.5.

For the EM parameters, a dielectric constant of 3.5 was considered, and the conductivity values were varied as follows: 0, 0.05, 0.01, 0.1, and 0.2 (Benedetto, 2014). These simulations contribute to a comprehensive understanding of the effects of moisture on EM wave propagation within the aggregate medium.



**Figure 4.5.** The randomly distributed aggregate model M1 was used for numerical moisture studies, with the developed antenna model positioned at various locations: (a) 20 cm, (b) 22 cm, and (c) 24 cm.

The second model, M2, comprises spherical particles of water and aggregate with known radius, filling the same dimensional volume as the experiment. Subsequently, the volume of the upper half of the water spherical particles was incrementally reduced by 50%, 40%, and 20% (Figure 4.6) through a reduction in the radius of the water spheres. This reduction was applied due to the higher evaporation rates experienced at the top surface, thereby reflecting the real-world phenomenon of water volume reduction.

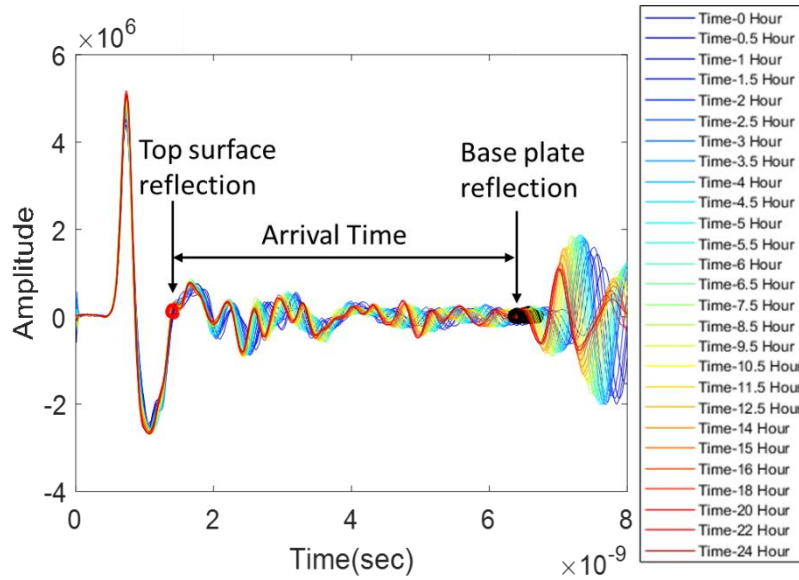


**Figure 4.6.** *The randomly distributed aggregate-water model M2 considered water as discrete particles rather than a continuous property, with a reduction of water volume in the top half of the model: (a) 20%, (b) 40%, and (c) 50%.*

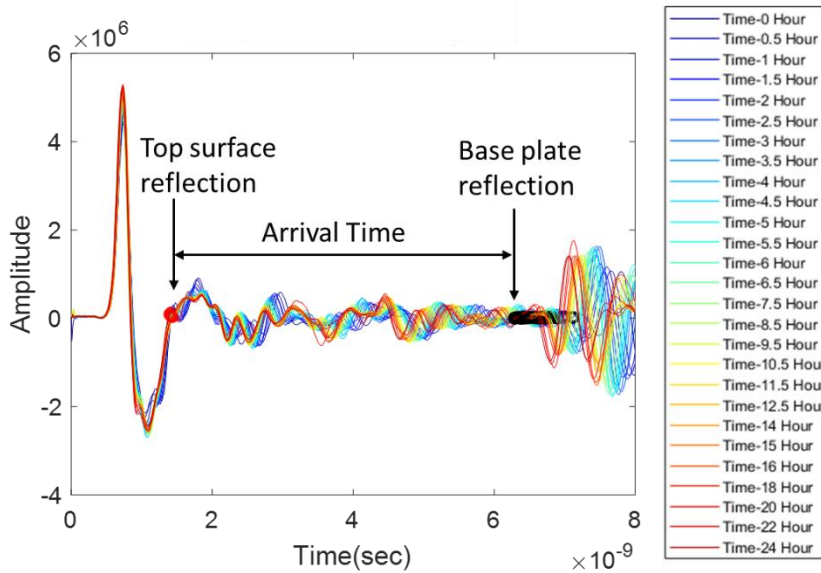
### 4.3 Result and discussion

The conducted experiments indicate discernible frequency shifts of EM wave signals within the aggregate setup due to moisture. These shifts suggest that the evaporation of moisture within the aggregate leads to an expedited EM wave arrival time and a shift in frequency from a lower to higher values.

The EM wave signals acquired from the GSSI 1600 MHz module in the experimental setup, both on the top surface and the side surface, exhibit distinct changes in the wave pattern over the 24-hour testing period. The observable shift in the signal indicates an accelerated time of arrival to reach the bottom of the aggregate setup, providing clear evidence of moisture evaporation (Figure 4.7). This consistent trend is also evident in the side surface scans (Figure 4.8).



*Figure 4.7. The EM wave responses obtained from the top surface at the 26 cm location demonstrate a shift in the arrival time of the bottom surface throughout the 24-hour period.*



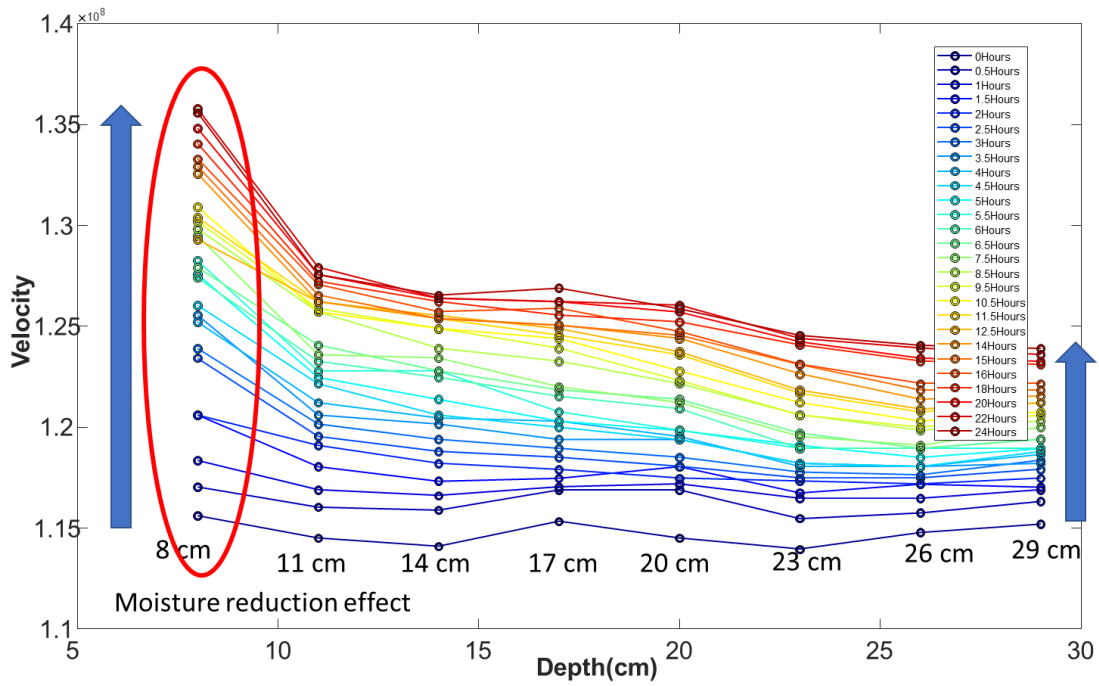
*Figure 4.8. The EM wave responses obtained from the side surface at the 17 cm location exhibit a shift in the arrival time of the bottom surface over the 24-hour period.*

#### 4.3.1 *Analysis of experimental wave responses*

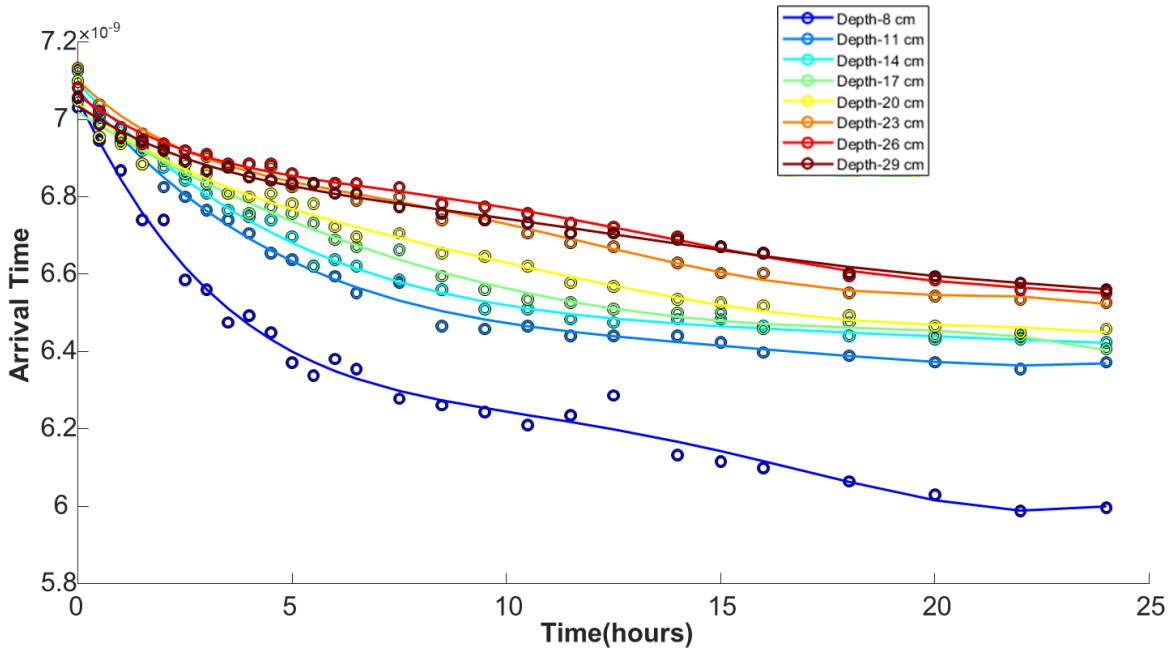
The EM wave response captured by the GSSI antenna distinctly reveals that the side scan responses, as depicted in Figure 4.9, exhibit a lower wave velocity of  $1.15 \times 10^8$  cm/s at 0 hours. This contrasts with the 24-hour measurement, where the velocity experiences a significant increase of 17% to  $1.35 \times 10^8$  cm/s in the case of the 8 cm depth (top region of the aggregate). Similarly, at the 29 cm location (bottom area), a similar trend is observed, albeit with a relatively modest 8% velocity increase compared to the top area (red marking), which displayed a 17% velocity augmentation. This observation points to higher evaporation at the top surface in comparison to the bottom area.

Figure 4.10 illustrates that the wave's arrival time during the early stages of saturation is around 7.2 nanoseconds. After 24 hours, this arrival time notably reduces to a range of 6 to 6.8 nanoseconds. The alteration in arrival time for each depth line in Figure 4.10 provides insights into the evaporation rate per centimeter. This rate of evaporation can be juxtaposed with the change in weight loss measured during the experiment, depicted in Figure 4.12, to discern similarities and discernible trends.

To assess the comparability, the evaporation rate is computed by averaging the arrival times over the 24-hour period, and a curve fit is then applied to these averaged values. Similarly, the measured weight data is plotted in Figure 4.13 alongside a corresponding curve fit. Remarkably, both the curve fits for the evaporation rate and the weight measurements exhibit an R<sup>2</sup> value of nearly 98%, indicative of a robust curve fitting outcome. Combining these two normalized curve fit equations in Figure 4.13, demonstrates striking similarities in patterns. The EM wave signal response corroborates these findings, providing a clear indication of moisture variation changes over time.



**Figure 4.9.** The velocity variation of the signal along the side surface exhibits a gradual decrease as the depth increases. Notably, at the location of 8 cm (red mark), there is a substantial 17% increase in velocity attributed to evaporation occurring at the top surface.



**Figure 4.10.** The arrival time for reaching the end of the aggregate medium, as observed from the side surface, demonstrates a reduction, indicating that the wave propagates faster.

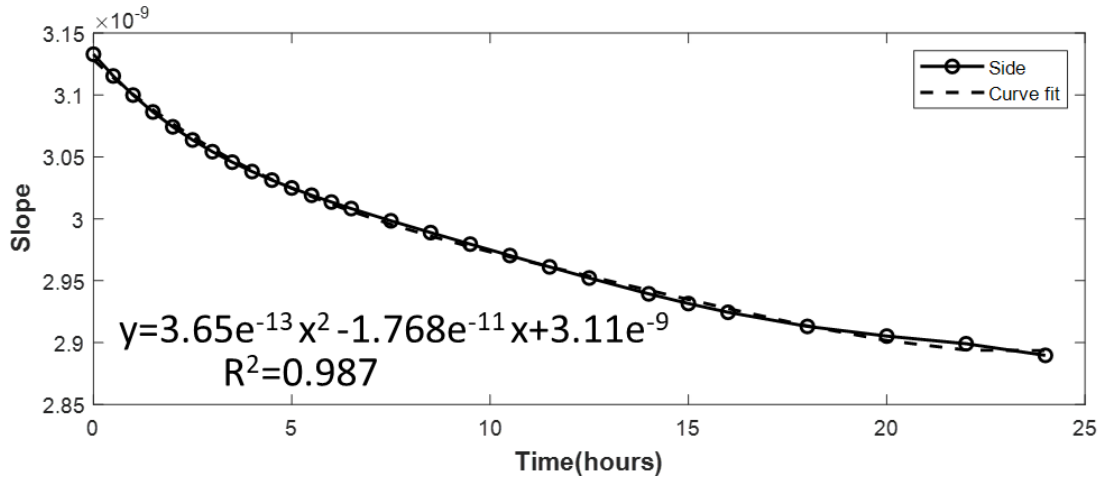


Figure 4.11. The evaporation rate, derived from the EM wave data obtained from the side surface scan, is averaged for each location, and subsequently fitted with a curve.

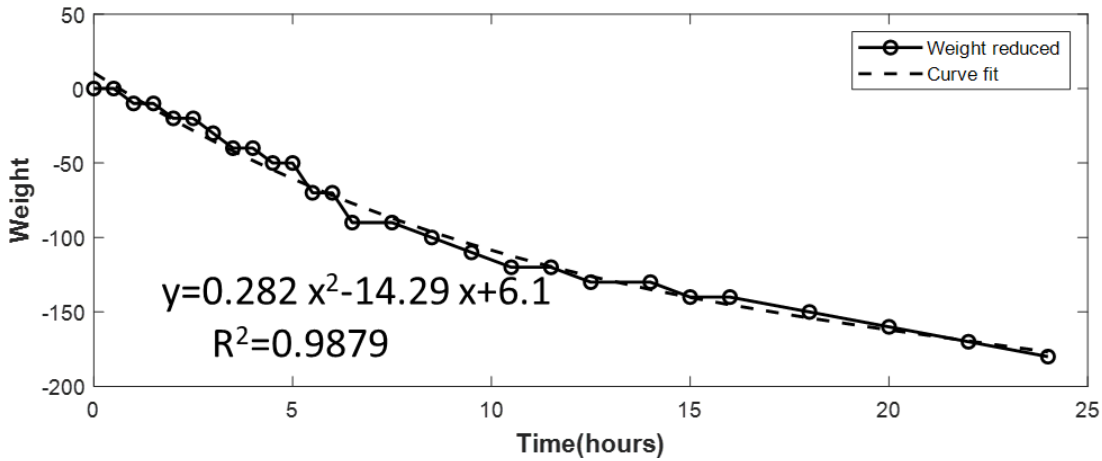


Figure 4.12. Weight measurements of the saturated aggregate experimental setup were taken as it transitioned from a saturated to a dry state, and these measurements were fitted with a curve.

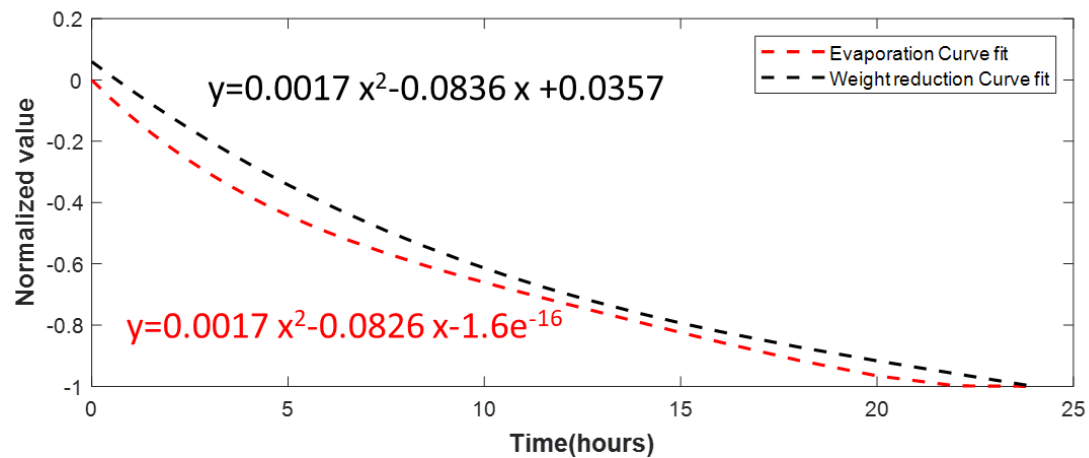
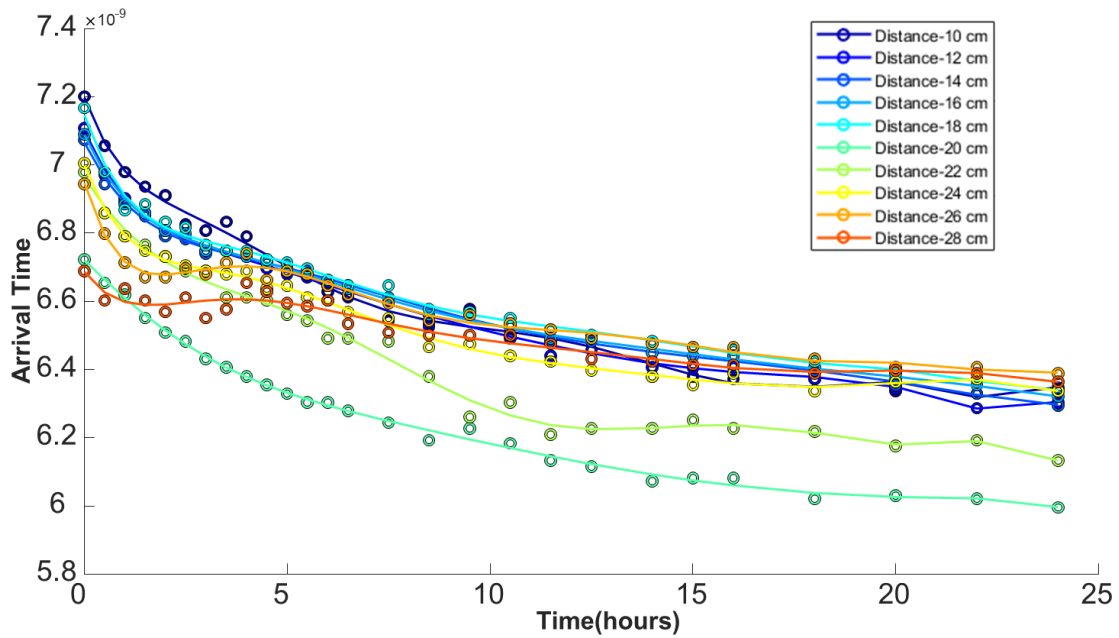


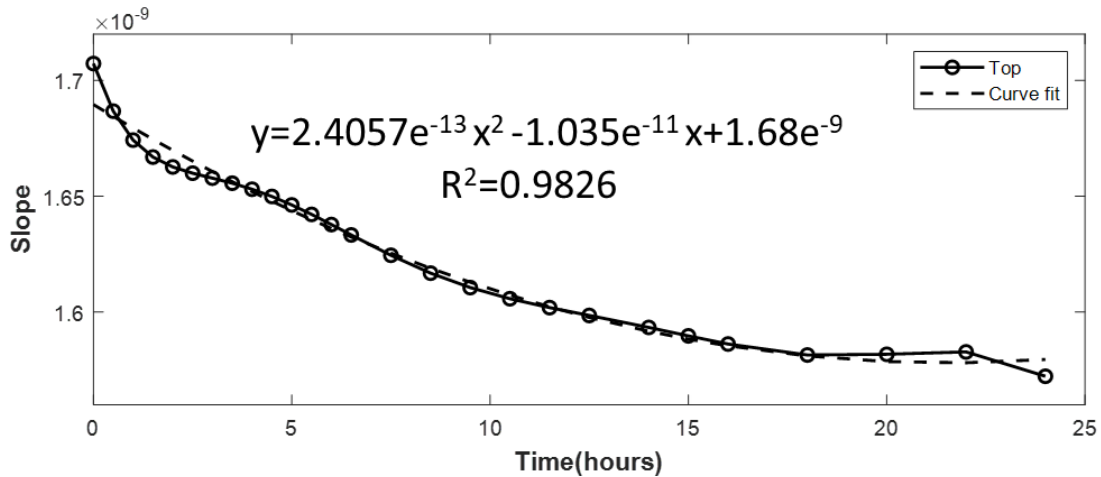
Figure 4.13. Comparing the evaporation rate and the curve fit for weight reduction serves to validate the EM wave signals.

Similarly, the EM wave responses gathered from the top scan shown in Figure 4.14 exhibit a reduction in arrival time as the 24-hour mark is reached. In a manner akin to the side scans, the evaporation rate was charted as presented in Figure 4.15, correlating the alteration in arrival time with the location, as measured by the GSSI antenna. This correlation is illustrated by the curve fit shown in Figure 4.16. Notably, the normalized curve fit of the arrival time for the top surface's wave responses, alongside the measured weight, also presented analogous patterns. These findings collectively underscore the influence of moisture on the EM wave signals acquired from the top scan.

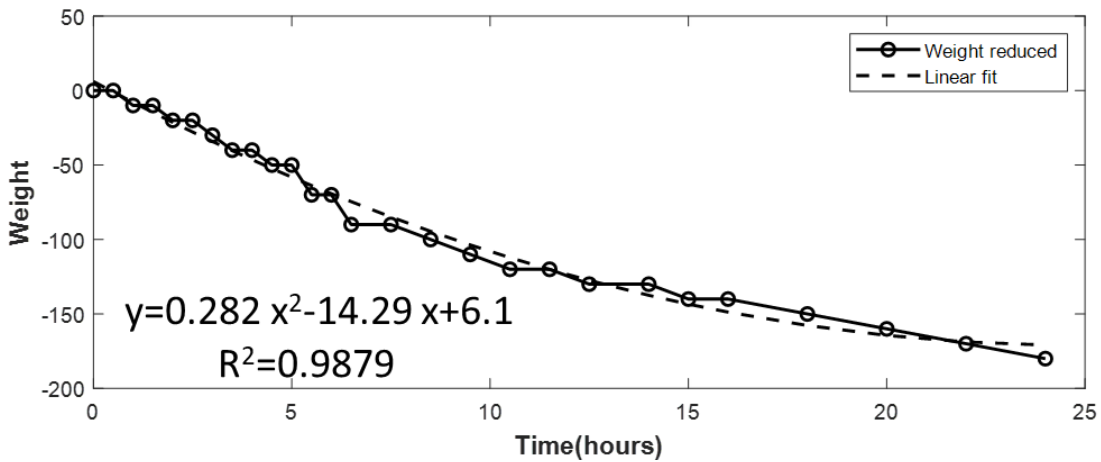


**Figure 4.14.** The arrival time for reaching the end of the aggregate medium, as observed from the top surface, demonstrates a reduction, indicating that the wave propagates faster.





**Figure 4.15.** The evaporation rate, derived from the EM wave data of the side surface scan, was averaged for each location and plotted alongside a curve fit.



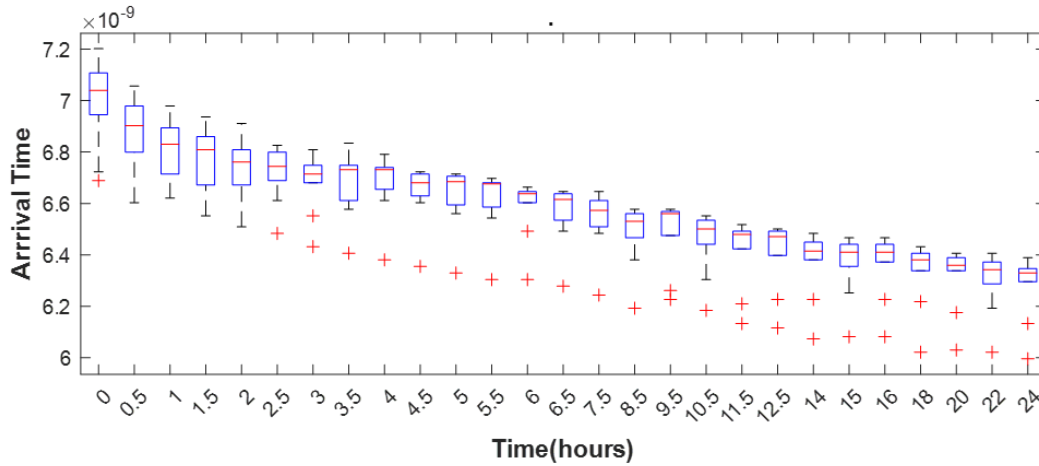
**Figure 4.16.** Comparing the curve fits of the evaporation rate and weight reduction serves to validate the EM wave signals.

After confirming the effects of moisture on the EM wave, statistical parameter studies were conducted to identify any anomalies or trends in the pattern studies. These statistical parameters included the arrival time of the bottom plate, maximum signal amplitude, signal average, signal skewness, and the frequency spectrum evaluated through FFT. As the data was collected over a 24-hour period, all these data points were condensed into box plots for a clearer representation and better understanding.

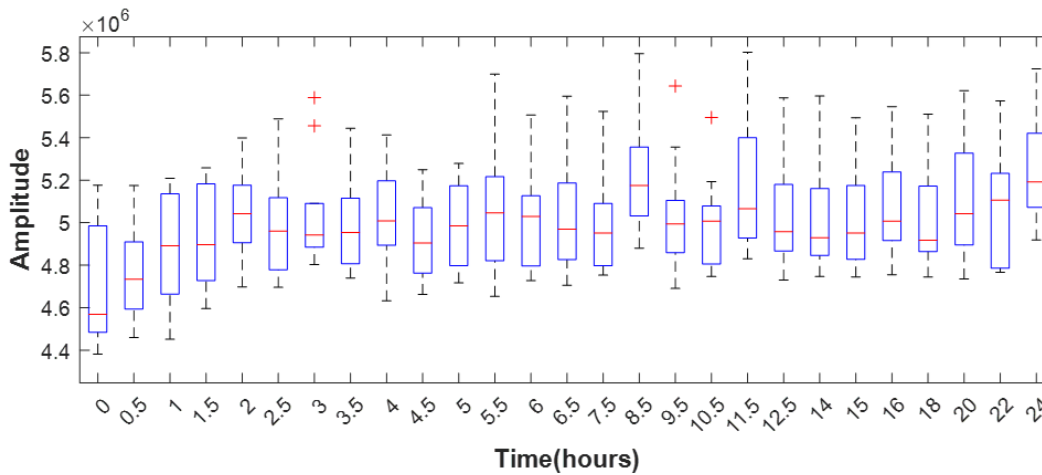
Among these parameters, a significant decrease in arrival time was observed over the test period, as depicted in Figure 4.17. Conversely, both the amplitude and average of the signal increased as time progressed, as



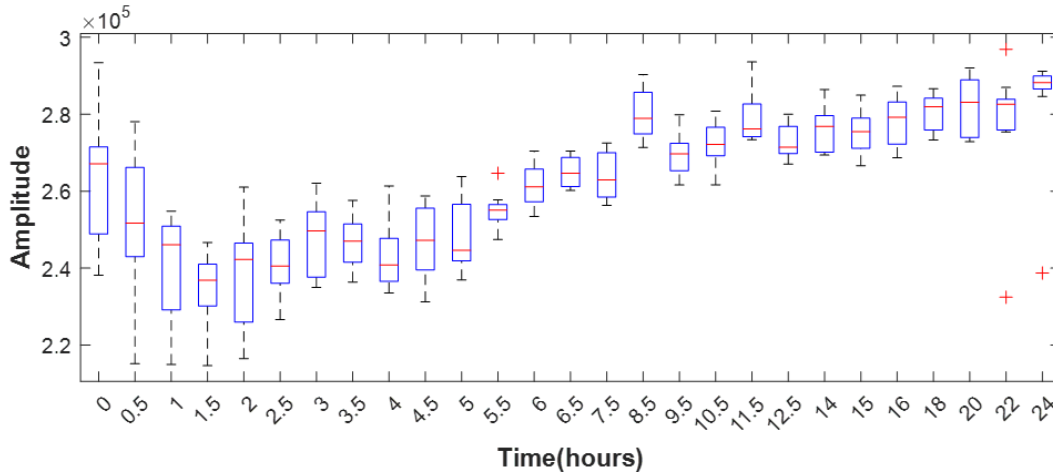
shown in Figure 4.18 & 4.19. In terms of the frequency spectrum magnitude, as illustrated in Figure 4.20, there was an initial high frequency followed by a gradual decrease over the 24-hour period. Consequently, further investigation into the frequency spectrum is conducted in Section 4.3.2.



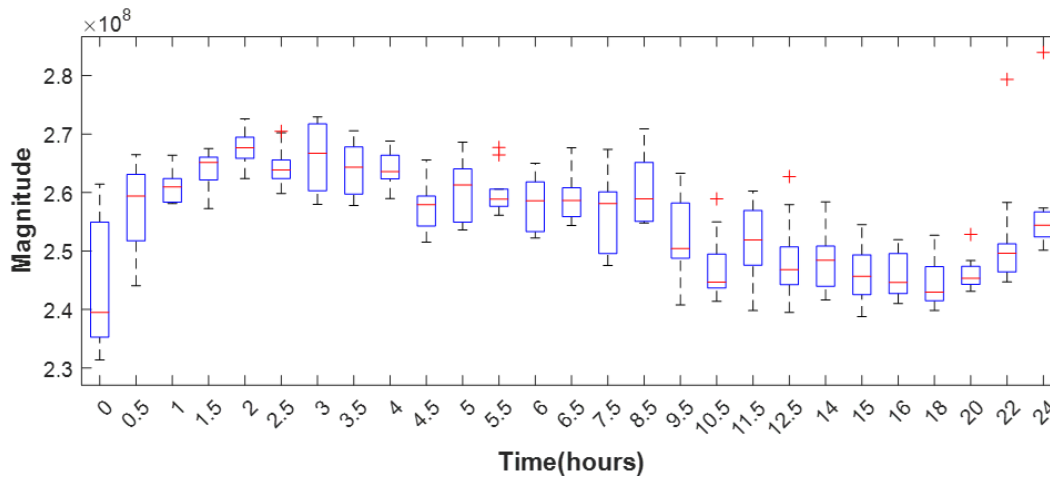
**Figure 4.17.** Box plot illustrating the range and pattern of arrival times recorded throughout the testing period.



**Figure 4.18.** Box plot illustrating the range and pattern of maximum amplitude recorded over the testing period.



**Figure 4.19.** Box plot illustrating the range and pattern of the mean of the EM wave signal recorded over the testing period.

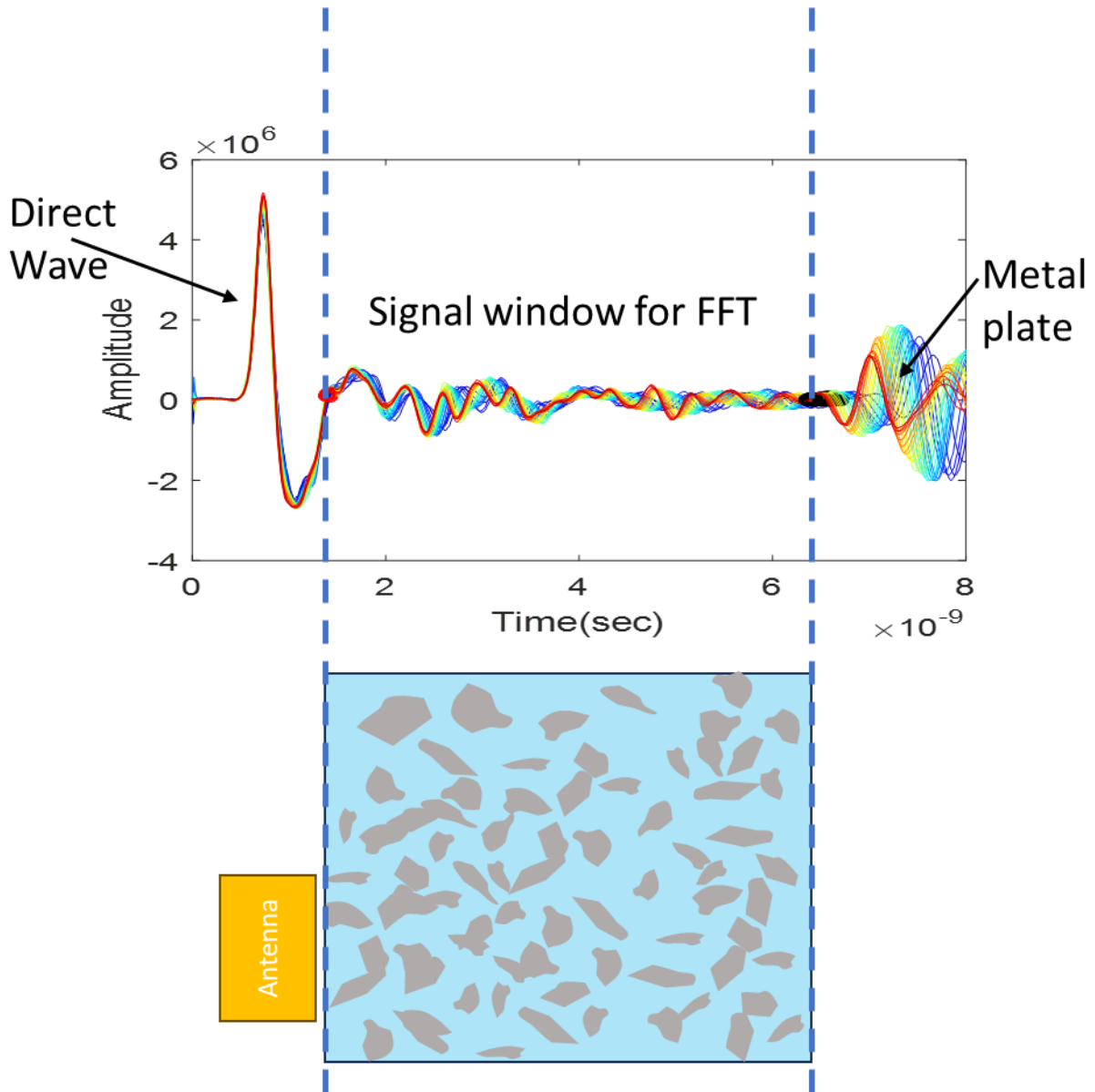


**Figure 4.20.** Box plot illustrating the range and pattern of frequency amplitudes recorded over the testing period.

### 4.3.2 Frequency spectrum analysis

Most of the literature studies have commonly conducted frequency spectrum analysis on the entire signal, encompassing both the direct wave response and the metal plate reflection. The direct wave consists of the signal transmitted directly from the transmitter to the receiver, combined with the reflection from the top surface to the receiver. The metal plate, positioned at the bottom of the setup, exhibits a distinct high peak reflection. However, this peak reflection doesn't directly indicate the moisture level; rather, it serves as a reference point for identifying the boundary of the medium. Both the direct wave and the metal plate

reflection are clearly depicted in Figure 4.21. For a more in-depth investigation of the EM wave responses, the frequency analysis excludes the direct wave and metal plate reflection. This exclusion range is depicted in the figure, denoted as the signal window of FFT.

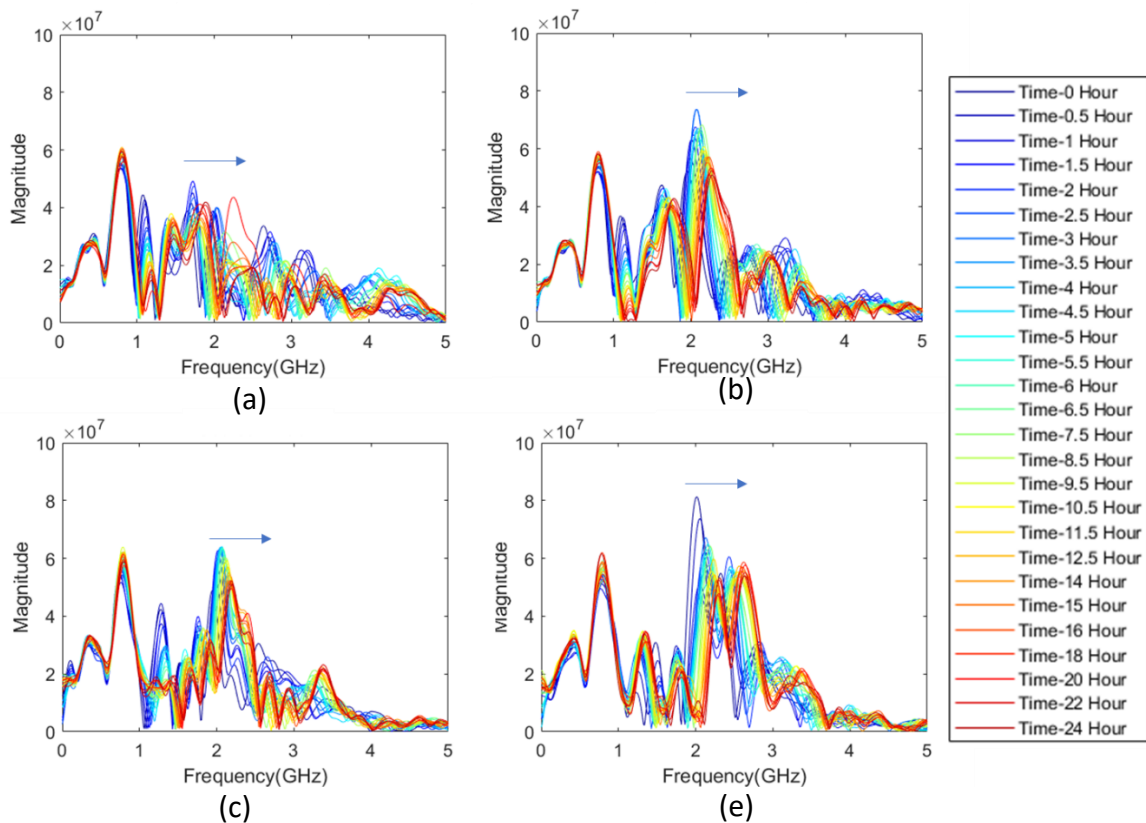


**Figure 4.21.** The EM wave signal encompasses the direct wave response, the wave response within the medium, and the reflection response from the metal plate.

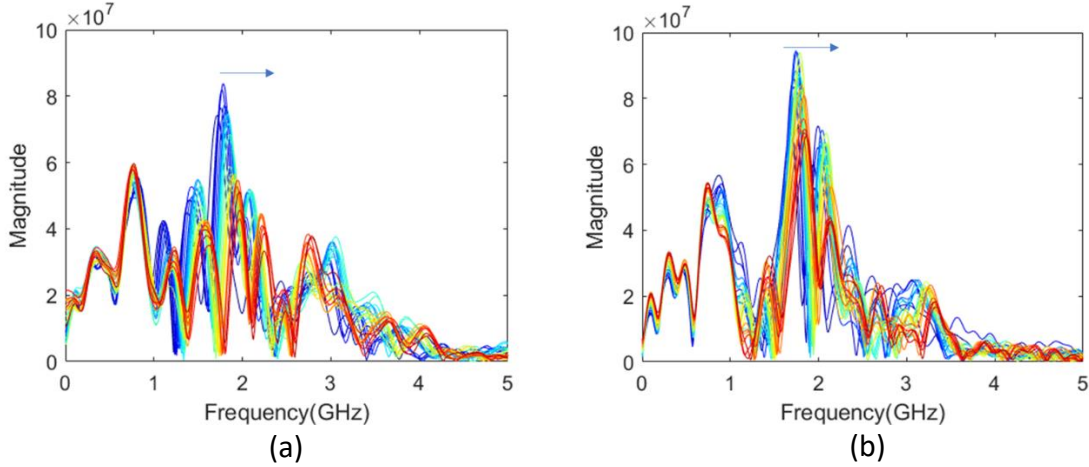
Since the wave responses display alterations in arrival time for the metal plate reflections (Figure 4.7 & 4.8) it is not logical to individually consider the arrival times of each metal plate reflection, as they would

possess distinct time windows for each signal. To mitigate this confusion, a uniform window size is maintained for all signals over the 24-hour period. However, the initiation of the signal is standardized, commencing from the conclusion of the direct wave, which remains consistent across all cases, as depicted in Figure 4.21. This approach ensures that the signals primarily reflect changes in moisture within the medium, excluding the influence of the metal plate or the direct wave.

These windowed signals are subjected to frequency spectrum analysis and processed in MATLAB, revealing a discernible shift in central frequency or peak frequency corresponding to the transition from a moist to a dry state, as depicted in Figure 4.22. This frequency shift is also observed alongside surface scans, as illustrated in Figure 4.23.

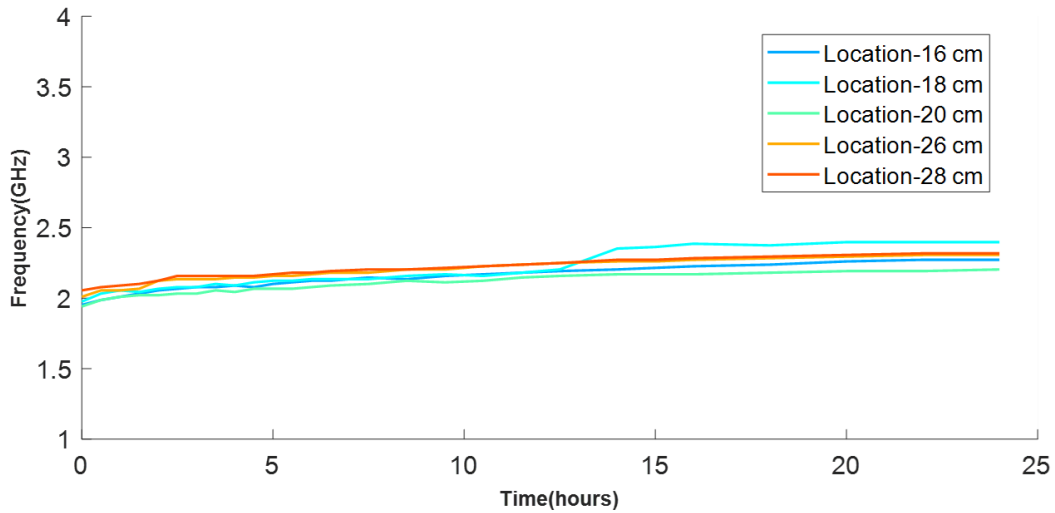


**Figure 4.22.** Frequency spectrum analysis of the windowed EM wave response signal from the top surface reveals shifts in peak frequency at various locations: (a) 14 cm (b) 16 cm, (c) 20 cm and (d) 26 cm.



**Figure 4.23.** Frequency spectrum analysis of the windowed EM wave response signal from side surface reveals shift in peak frequencies at location: (a) 11 cm and (b) 29 cm.

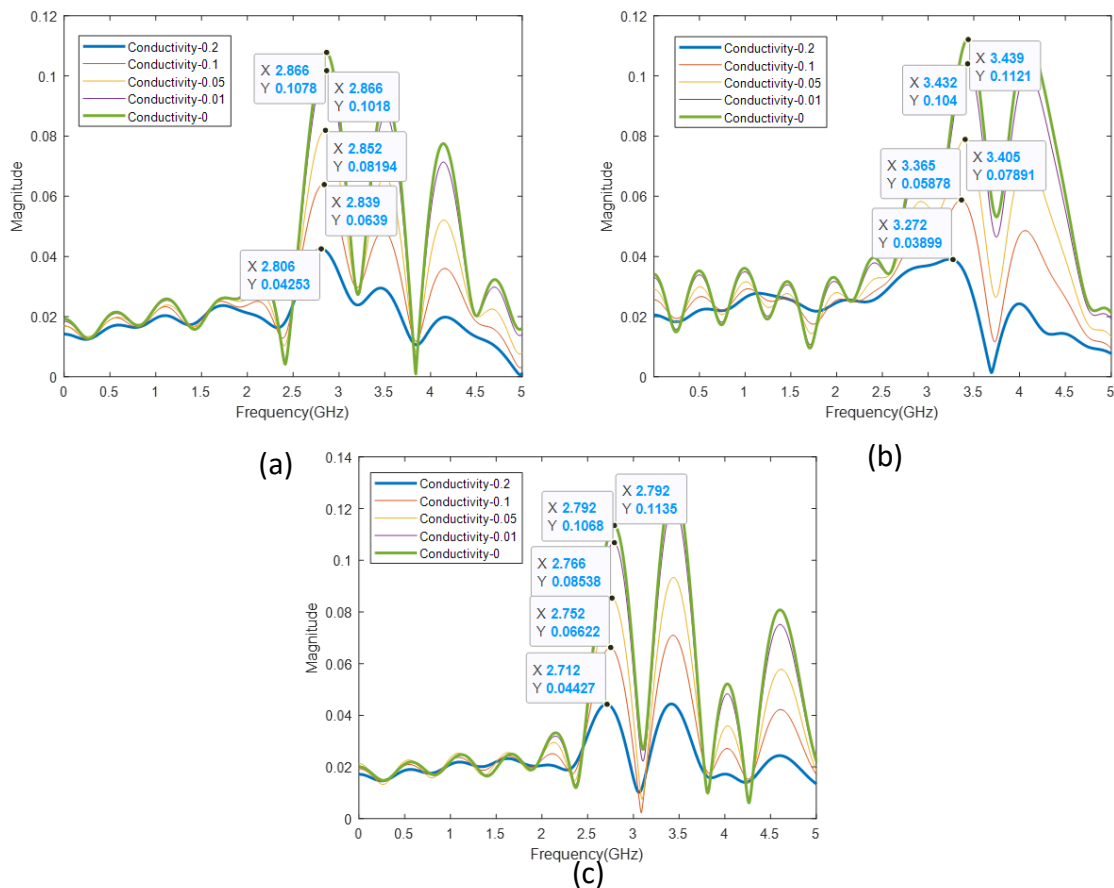
The peak frequencies, acquired through the application of the signal window, are plotted against the time period of the collected data (Figure 4.24). This presentation clearly demonstrates an observable rise in peak frequencies attributed to the presence of moisture. To confirm the observed incremental frequency shift, FDTD models are simulated, as outlined in Section 4.2.2 utilizing the conceptualized random aggregate models described in Section 3.2.2.



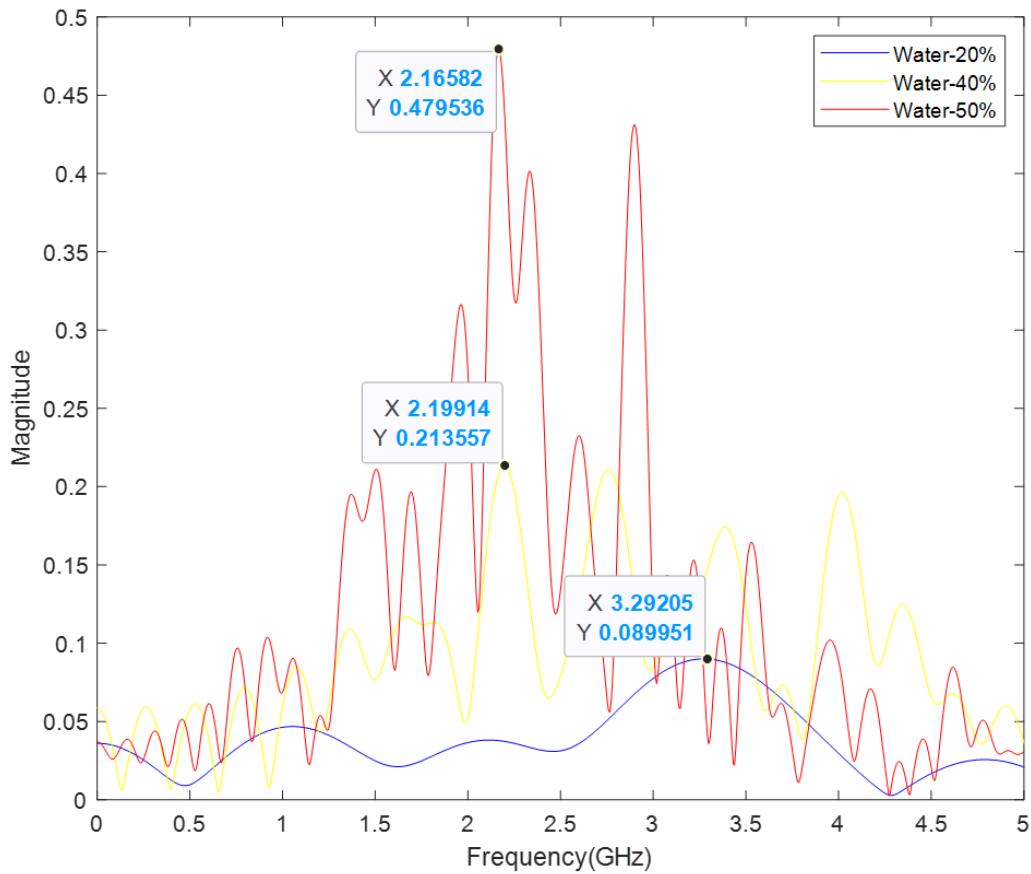
**Figure 4.24.** Variation in central frequency shift across different locations of the experimental EM wave spectral response.

In a manner akin to the experimental approach, the signal window for the simulated EM wave responses of models M1 and M2 was also defined, commencing after the direct wave. Upon subjecting the simulated EM wave responses to frequency spectrum analysis, a subtle alteration in frequency shift was observed for model M1 (Figure 4.25), whereas model M2 displayed a distinct and incremental frequency shift from a saturated state (50% moisture) to a semi-dry state (20% moisture) (Figure 4.26).

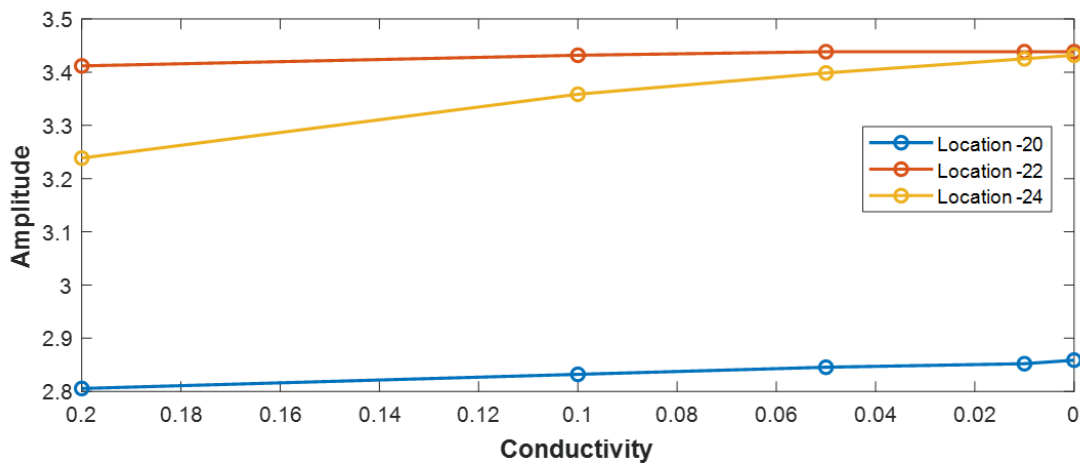
Remarkably, both the experimental (Figure 4.24) and numerical simulation (Figure 4.27 & 4.28) results underscore a novel methodology to distinctly illustrate the shift in peak frequency under varying moisture conditions. This corroborates the notion that the incremental frequency shift within the frequency spectrum, while considering the time window of the signal within the medium, can predict the moisture effect through EM wave responses.



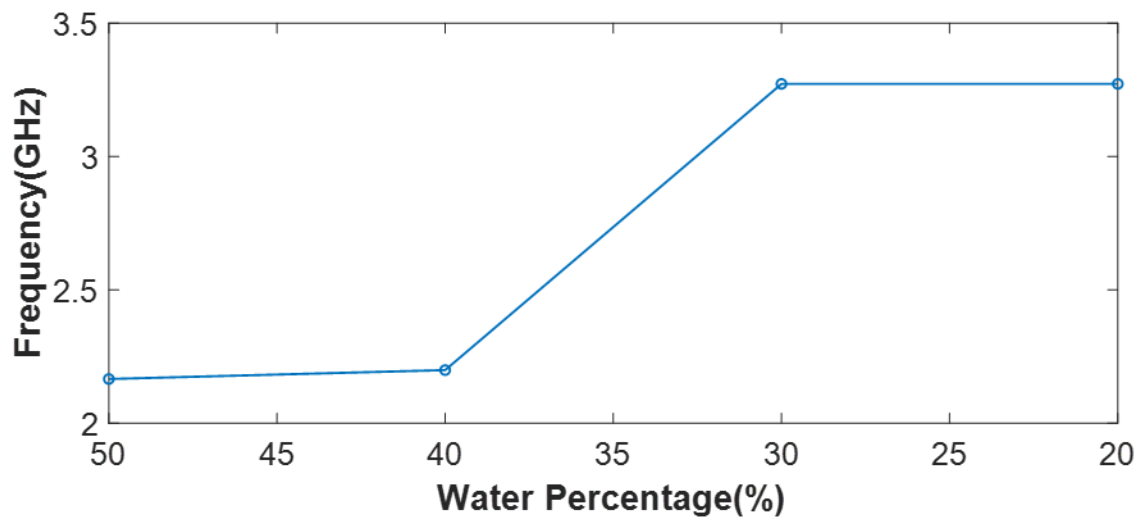
**Figure 4.25. Frequency spectrum analysis of numerical model M1 reveals a subtle peak frequency shift at distinct locations: (a) 20 cm, (b) 22 cm, and (c) 24 cm.**



*Figure 4.26. The frequency spectrum of numerical model M2 exhibits a significant shift in both magnitude and peak frequency. Each distinct frequency and magnitude signify the shift in the central frequency as the drying process progresses.*



*Figure 4.27. Slight increment in peak frequency shift in numerical simulation M1, reflecting the variation in conductivity from 0.2 (saturated) to 0 (dry condition) as obtained from EM wave spectral response.*



*Figure 4.28. Increase in peak frequency shift in numerical simulation model M2, illustrating moisture variation from 50% to 20%.*



### 4.3.3 *Discussion and conclusion*

The frequency spectrum consistently demonstrated variations as the conditions transitioned from saturation to dryness, with predominant evaporation occurring in the upper portion of the container. Analyzing the arrival times of the baseplate indicated a reduction in time, although anomalies were observed at distances of 20 cm and 26 cm, revealing faster times compared to other locations (Figure 4.14). These anomalies might arise from the influence of boundary effects on EM waves or accelerated drying of an uneven medium. This uncertainty underscores the potential effectiveness of investigating the arrival times using the bottom plate as a reference.

Focusing exclusively on the signal window within the medium's EM wave response and analyzing the frequency spectrum, a distinct shift in peak frequency from saturation to dry states became evident (Figure 4.24). This shift was consistently observed in both numerical models, M1 and M2. In the case of M1, slight variations in conductivity resulted in a minor frequency shift, as depicted in Figure 4.27, Conversely, in Model M2, which emulates the upper region of aggregated water particles and incorporates a reduced water radius indicating moisture alterations of 20-50%, a marked shift in frequencies was clearly apparent (Figure 4.28). This consistent pattern of significant frequency shift, observed in both experimental and numerical simulations, underscores the efficacy of utilizing EM wave frequencies for enhanced moisture detection.

## CHAPTER 5 CORROSION STUDY

### 5.1 Motivations

In this chapter, I delve into an examination of rebar corrosion within concrete under the influence of EM waves. This investigation is supplemented by secondary assessments using half-cell potential, surface resistivity, and corrosion rate measurements. The corrosion process is accelerated through the application of constant voltage/current. Our study encompasses both the initial and advanced stages of accelerated corrosion induced by EM waves, employing a combination of experimental analysis and numerical simulation, as outlined in Section 2.3.2 through a brief description of FDTD simulation.

Verification procedures entail employing the ICOR half-cell potentiometer to analyze half-cell potentials, while surface resistivity is gauged using the Proceq surface resistivity meter. To facilitate corrosion rate evaluation, an electric circuit setup is devised to maintain consistent voltage and current levels for the accelerated corrosion protocol. These thresholds are established based on pertinent literature. Analysis of half-cell potential values reveals notable trends: in the preliminary stage prior to significant corrosion progression, values tend to be relatively high, ranging from approximately -150 mV to -350 mV. As corrosion advances, potentials shift to a range of -400 mV to -700 mV (Elsener, 2003; Pratanu, 2015; Stratfull, 1973).

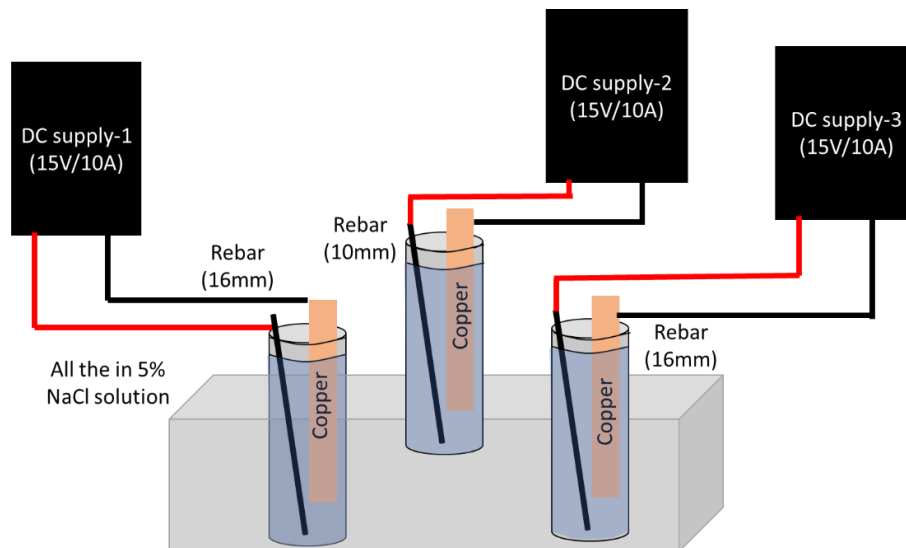
Surface resistivity measurements display a gradual increase until the point where corrosion byproducts infiltrate the surface. This infiltration leads to a subsequent decline in resistivity. The experiments on accelerated corrosion (AC) encompass a series of six tests. In the first and third tests (AC-T1 and AC-T3), the focus is exclusively on rebar corrosion. The second, fourth, fifth, and sixth tests (AC-T2, AC-T4, AC-T5, and AC-T6) address concrete acceleration corrosion. AC-T2's objective is to clarify the impact of high voltage/current on the dynamics of concrete-rebar corrosion. AC-T3 involves understanding the corrosion rate (Lim, 2010), while AC-T4 explores the effects of corrosion on early-age concrete. This corrosion is initiated immediately after concrete casting and without undergoing the curing process. AC-T5 and AC-T6

are conducted after a 28-day curing period for the concrete specimens, allowing for a deeper exploration of corrosion implications.

## 5.2 Corrosion model investigation

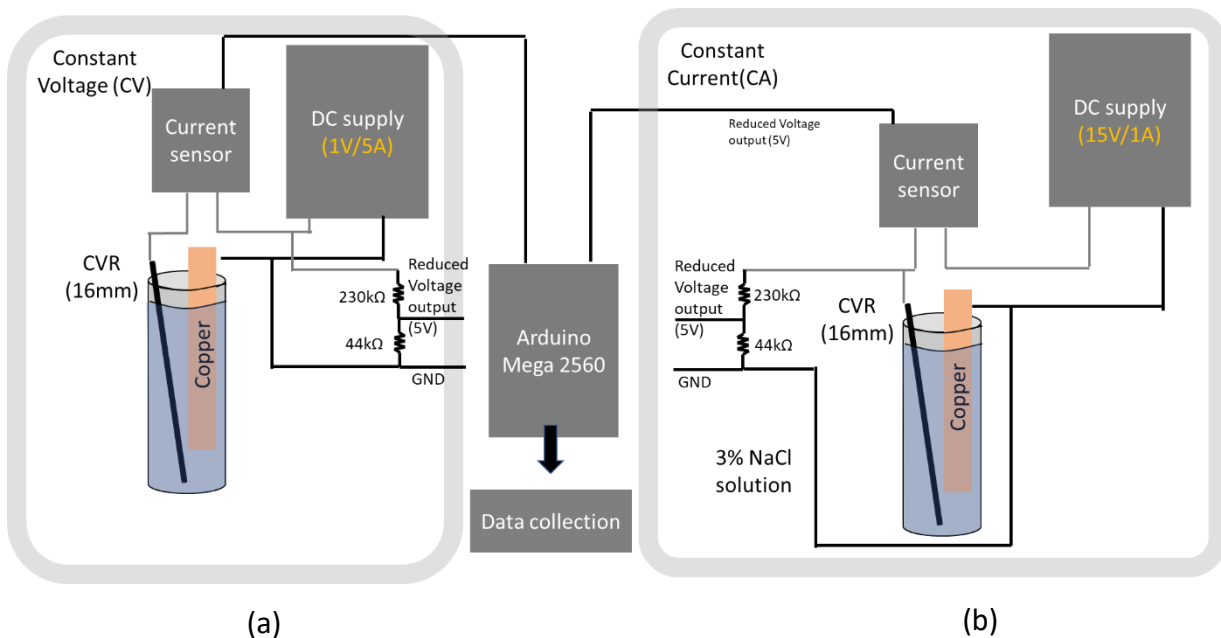
### 5.2.1 *Experimental testing: Rebar*

The initial test, designated as AC-T1, aimed to expedite the corrosion process, contrasting with the protracted timelines often outlined in existing literature, where the corrosion process extends over several months or even years. To facilitate accelerated corrosion, the operation of direct current (DC) supply voltage and current emerged as a pivotal factor. In this specific experiment AC-T1 as shown in Figure 5.1, three rebar specimens were utilized: two measuring 16mm and one measuring 10mm in diameter, each spanning a length of 12 inches. These rebars were immersed within a 5% NaCl electrolyte solution, in conjunction with copper plates. To drive the corrosion process, each rebar was linked to a DC supply unit configured to 15V/10A maintaining a constant voltage/current threshold. Notably, the rebar functioned as the anode, while the copper plate served as the cathode, as depicted in the schematic diagram.



**Figure 5.1.** Schematic representation of AC-T1 testing for rebar corrosion (16 and 10 mm), conducted exclusively without concrete, aimed at providing enhanced clarity.

Throughout the experimental progression, the tracking of half-cell potentials and mass reduction was meticulously planned for each day of the corrosion process. The third test, denoted AC-T3 as shown in Figure 5.2, centered on a pair of 16mm rebars with a length of 14 inches. The objective was to validate the adequacy of the chosen constant voltage/current settings in terms of timeline considerations collected through Arduino mega 2560, documenting the half-cell potential and mass reduction analyses. The constant voltage configuration entailed a DC supply of 1V/5A, thus ensuring that the voltage was consistently maintained at 1V. In the context of constant current, the threshold was set at 15V/1A, signifying that the current remained steadfast at 1A.



**Figure 5.2. Schematic representation of AC-T3 testing, illustrating corrosion of two 16mm rebars in two modes: (a) constant voltage (CV) and (b) constant current (CA), conducted solely without concrete. This depiction aims to offer improved clarity regarding the voltage/current supplied.**

Furthermore, this testing phase featured the development of a specialized setup to capture variations in current resulting from the application of constant voltage through the DC supply. Similarly, alterations in voltage were meticulously recorded when operating under constant current conditions. Employing this dataset on current fluctuations, the corrosion rate calculations were subsequently derived using:

$$\text{Corrosion rate by current} = \frac{iM}{nF} \quad 5.1$$

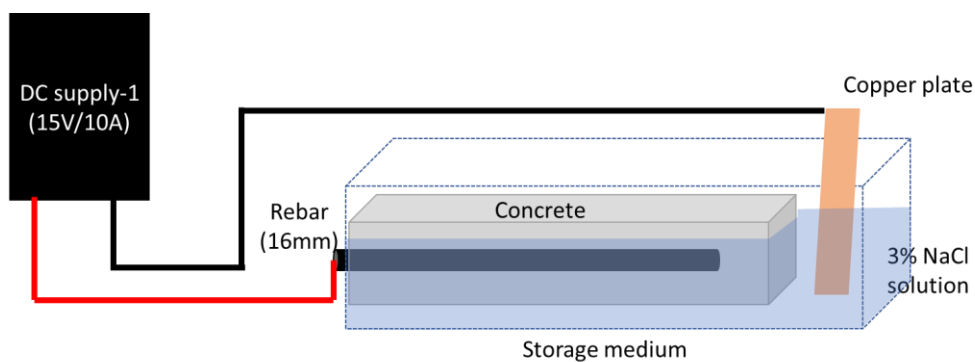
$$\text{Corrosion rate by weight} = \frac{m}{t}$$

5.2

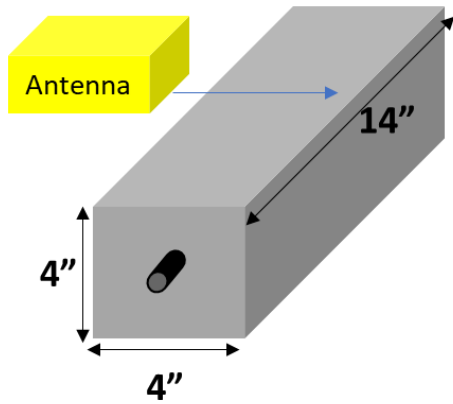
where  $i$  represents the current applied to accelerate corrosion, facilitating the movement of electrons ( $n$ ) from iron.  $M$  denotes the atomic mass of iron, while  $F$  stands for the Faraday constant. In Eq.5.2,  $m$  signifies the mass loss of the rebar over a specific time interval ( $t$ ).

### 5.2.2 Experimental testing: Embedded rebar in concrete

The AC-T2 experiment involved subjecting a concrete rebar specimen measuring 4x4x14 inches to accelerated corrosion within a 3% NaCl electrolyte solution alongside a copper plate. The setup employed a DC power supply with a threshold of 15V/10A, wherein the concrete rebar served as the anode and the copper plate acted as the cathode. The primary aim of this study was to discern the timeframe required for rapid corrosion acceleration. Given the substantial corrosion reactions observed in AC-T1, data collection for AC-T2 included recording of half-cell potential, surface resistivity, and EM wave readings at specific time intervals (Figure 5.4), rather than daily.



**Figure 5.3. Schematic representation of AC-T2 testing for concrete rebar specimens, focused on estimating the duration of corrosion under high voltage and current conditions.**



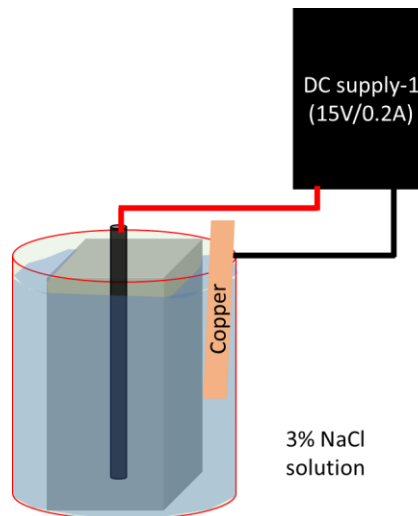
(a)



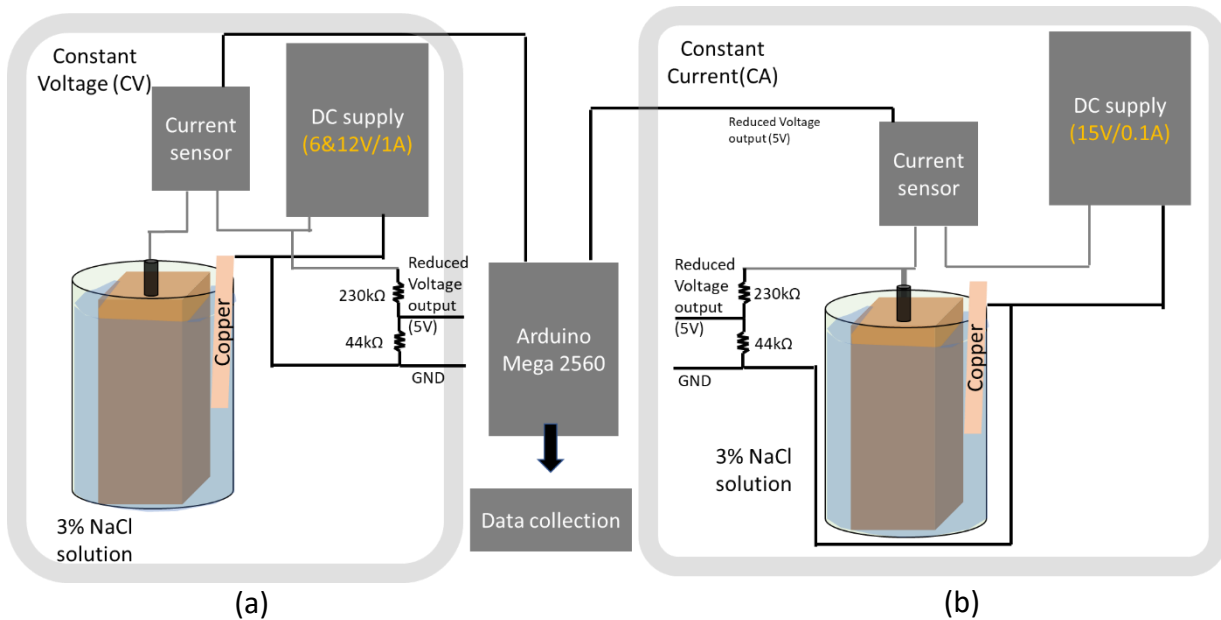
(b)

**Figure 5.4. Testing of AC-T2 (a) schematic diagram of the performed antenna scan direction. (b) experimental setup positioned in the laboratory.**

Building upon insights from AC-T1, T2, and T3, three additional tests focused on the rapid acceleration of concrete rebar corrosion were devised. The initial test, AC-T4, concentrated on early-age concrete corrosion. Concrete-rebar specimens underwent accelerated corrosion immediately after being removed from the casting mold, without any curing. The objective here was to analyze corrosion dynamics in a mature stage where hardening and corrosion occurred simultaneously.

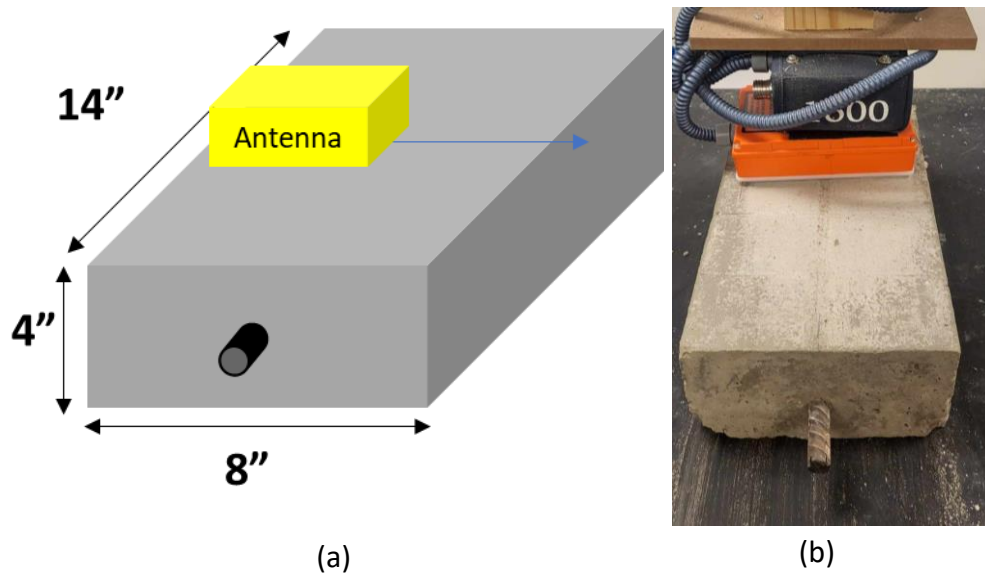


**Figure 5.5. Schematic representation of AC-T4 testing for concrete rebar specimens, aimed at understanding the corrosion effects on early-age concrete without curing.**



**Figure 5.6. Schematic representation of AC-T5 testing, illustrating the corrosion of two 16mm concrete rebar specimens in two modes: (a) constant voltage (CV) of 6 & 12V and (b) constant current (CV) of 0.1A. The aim is to comprehend the corrosion rate's effect on the EM wave.**

AC-T4 as shown in Figure 5.5 involved the examination of two concrete-rebar specimens, each measuring 4x8x14 inches and containing a 16mm (CR16) and a 10mm (CR10) rebar. The rebar was positioned with its center placed 2 inches from the upper surface of the concrete. The total length of the rebar was 14 inches, with 12 inches embedded within the concrete and 2 inches extending outside. These protruding segments were utilized for establishing connections to the DC power supply and for evaluating half-cell potential. The concrete-rebar specimens, acting as the anode, were immersed in separate containers containing a 3% NaCl electrolyte solution, accompanied by copper plates serving as cathodes. The experimental setup involved a DC supply with settings of 15V/0.2A. This deliberately low current level facilitated prolonged testing durations, enabling the observation of rapid corrosion acceleration over an extended period. Measurements of EM wave, half-cell potential, and surface resistivity were taken each day, with an interval of 1 hour allocated for drying after removal from the solution.

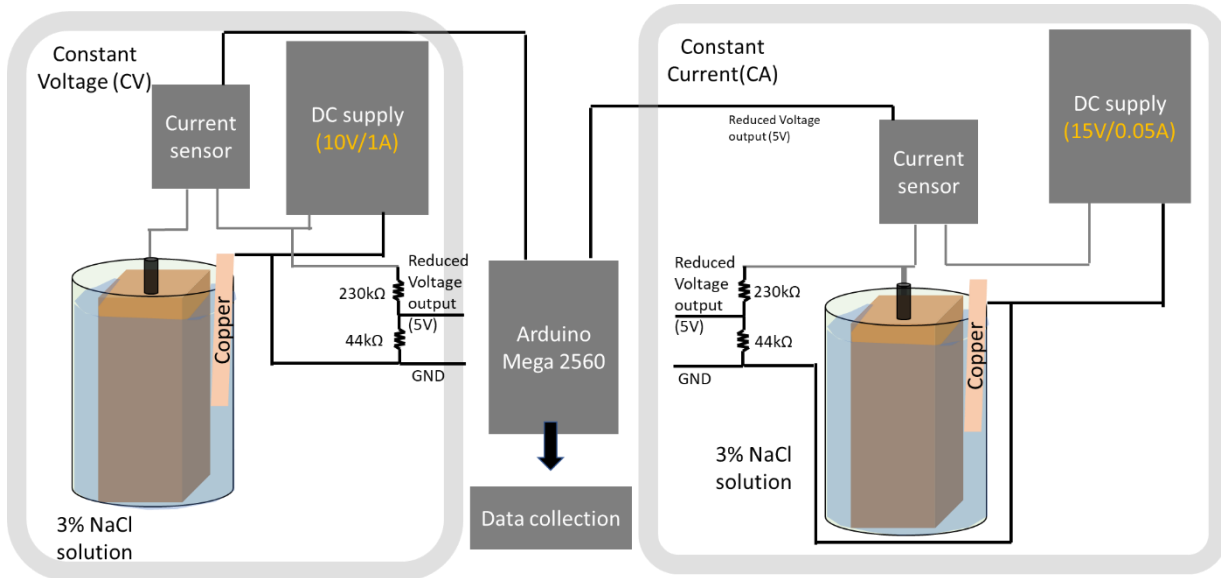


**Figure 5.7. Testing of AC-T4, T5 & T6: (a) schematic diagram of the antenna scan direction performed. (b) experimental setup positioned in the laboratory.**

The testing protocol concluded upon the attainment of consistent half-cell potentials and the visual detection of significant corrosion progression. The tested specimens were subsequently broken down to examine the extent of localized corrosion, as well as to determine any reduction in rebar mass and diameter.

The subsequent two tests, AC-T5 (Figure 5.6) and AC-T6 (Figure 5.8), were performed on specimens subjected to 28 days of water curing, under both constant voltage (CV) and constant current (CA) setups. For AC-T5, the concrete voltage was set at thresholds of 6V and 12V, each with a current of 1A. Alternatively, constant current testing featured a threshold of 15V/0.1A. Similar to AC-T4, concrete-rebar specimens of dimensions 4x8x14 inches, featuring a 16mm rebar positioned 2 inches from the top concrete surface, were employed. The specimens were immersed in separate containers containing 3% NaCl solution, with the concrete rebar serving as the anode and the copper plate as the cathode. Daily measurements of EM wave, half-cell potential, and surface resistivity were taken, accompanied by 1 hour of drying post-removal from the solution.





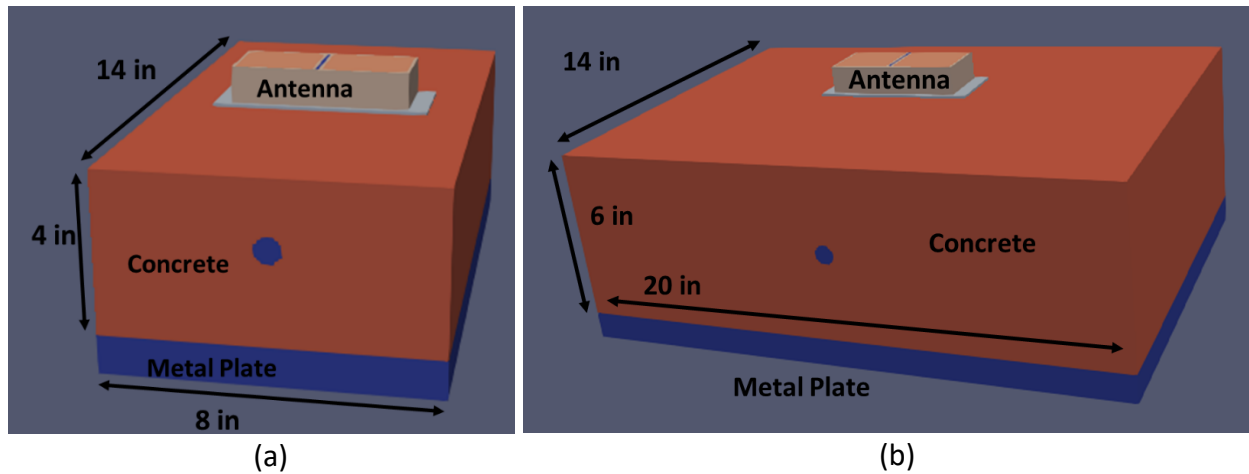
**Figure 5.8. Schematic representation of AC-T5 testing, illustrating the corrosion of two 16mm concrete rebar specimens in two modes: (a) constant voltage of 10V (CV) and (b) constant current (CA) of 0.05A. The aim is to understand the effect of corrosion after 1 hour and 24 hours of drying.**

The AC-T6 test encompassed two specimens tested under CV and CA conditions. The constant current setup utilized a DC supply of 15V/0.05A, while the constant voltage configuration employed 10V/2A. Similar to previous tests, the concrete-rebar specimens measured 4x8x14 inches, with a 16mm rebar situated 2 inches below the concrete surface. Data collection involved alternate-day measurements of EM wave, half-cell potential, and surface resistivity, with drying periods of 1 hour and 24 hours following removal from the solution.

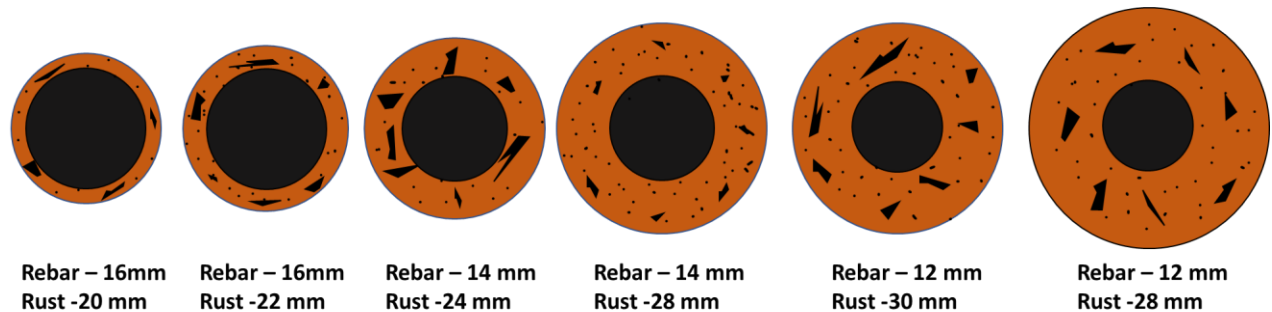
### 5.2.3 Numerical simulation

The numerical simulation of the corrosion FDTD model was predicated on hypotheses derived from the experimental analysis of concrete rebar. The corrosion process was initiated through a linear variation of dielectric constant and conductivity, with differing behavior observed during the passive and active states. Specifically, the dielectric constant ( $\epsilon$ ) exhibited variation ranging from 4 (representing concrete) to 10

(indicative of rust), while the conductivity ( $\sigma$ ) ranged from 0.001 (pertaining to concrete) to 0.077 (characteristic of rust)(Roqueta, 2012). Furthermore, the transition from the passive to active state was simulated by introducing an increase in rust particle presence around the rebar and a corresponding reduction in rebar size ( $R_e$ ) as in Table 5.1. This involved varying rust diameters ( $R_u$ ) from 20mm to 32mm and rebar diameters from 12mm to 16mm. The analysis included three distinct groups with rebar diameter ( $R_e$ ) variations as shown in Table 5.2.



**Figure 5.9. Numerical model developed: (a) resemble the experimental specimen, (b) after considering the appropriate depth for clear rebar reflection.**



**Figure 5.10. Variation in rust and rebar was considered for the numerical model simulation.**

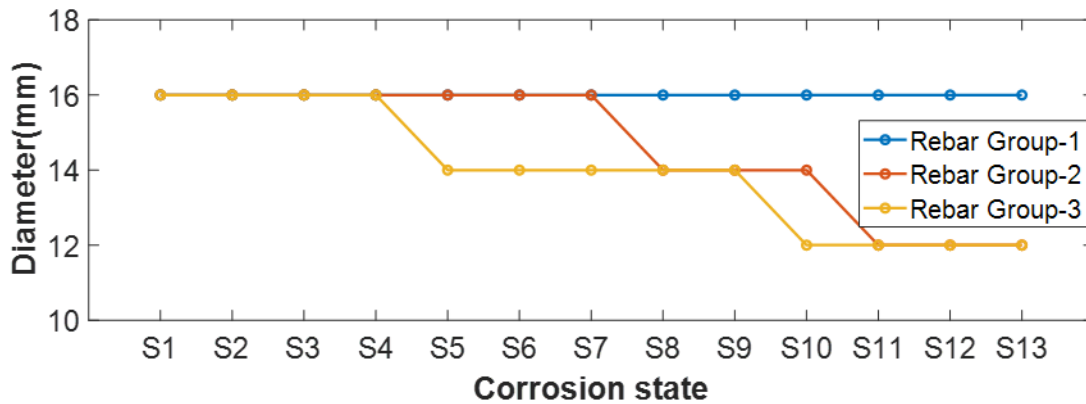
**Table 5.1. Parameter variables considered for corrosion study involving rust and rebar.**

Parameter	Value
Rebar Diameter	12-16 mm
Rust Diameter (Active state)	20-32 mm
Dielectric constant (S1-S7)	4-10
Conductivity (S1-S7)	0.001-0.077
Dielectric Constant (S8-S13)	10
Conductivity (S8-S13)	0.077

**Table 5.2. Collective investigation involving numerical simulations with varying combinations of rebar rust diameters.**

Stages	Group 1				Group 2				Group 3			
	$R_e$ (mm)	$R_u$ (mm)	$\epsilon$	$\sigma$	$R_e$ (mm)	$R_u$ (mm)	$\epsilon$	$\sigma$	$R_e$ (mm)	$R_u$ (mm)	$\epsilon$	$\sigma$
S1	16	20	4	0.005	16	20	4	0.005	16	20	4	0.005
S2	16	20	5	0.017	16	20	5	0.017	16	20	5	0.017
S3	16	20	6	0.029	16	20	6	0.029	16	20	6	0.029
S4	16	20	7	0.041	16	20	7	0.041	16	20	7	0.041
S5	16	20	8	0.053	16	20	8	0.053	14	20	8	0.053
S6	16	20	9	0.065	16	20	9	0.065	14	20	9	0.065
S7	16	20	10	0.077	16	20	10	0.077	14	20	10	0.077
S8	16	22	10	0.077	14	22	10	0.077	14	22	10	0.077
S9	16	24	10	0.077	14	24	10	0.077	14	24	10	0.077
S10	16	26	10	0.077	14	26	10	0.077	12	26	10	0.077
S11	16	28	10	0.077	12	28	10	0.077	12	28	10	0.077
S12	16	30	10	0.077	12	30	10	0.077	12	30	10	0.077
S13	16	32	10	0.077	12	32	10	0.077	12	32	10	0.077

The concrete model was initially established to mirror the experimental dimensions (Figure 5.9 (a)). However, the numerical responses pertaining to the rebar were not sufficiently elucidating. As a result, a minor parameter study was conducted to determine the optimal depth for corrosion analysis. Depths of 100mm (4 inches), 150mm (6 inches), 200mm (8 inches), and 300mm (12 inches) were evaluated. The findings indicated that a depth of 150mm (6 inches) was most conducive to capturing rebar reflections. While greater depths revealed more distinct rebar reflections, the amplitude of these reflections was markedly diminished. Consequently, the chosen model configuration (Figure 5.9 (b)) for further analysis was a concrete model measuring 150x490x350mm (6x20x14 inches), with rebar diameter variations classified as groups 1, 2, and 3 (Figure 5.11).



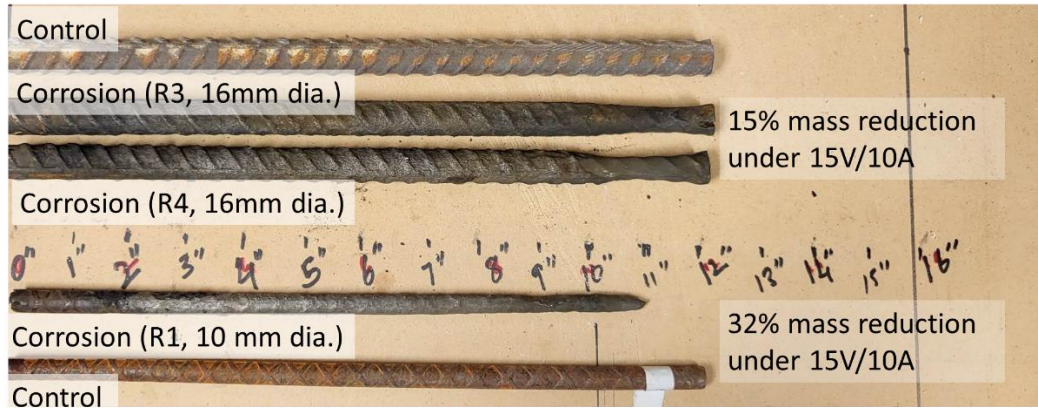
*Figure 5.11. Rebar groups 1, 2, and 3 were employed to represent the variation of rebar placement in the concrete model, illustrating the impact of rust-induced changes.*

### 5.3 Result and discussion

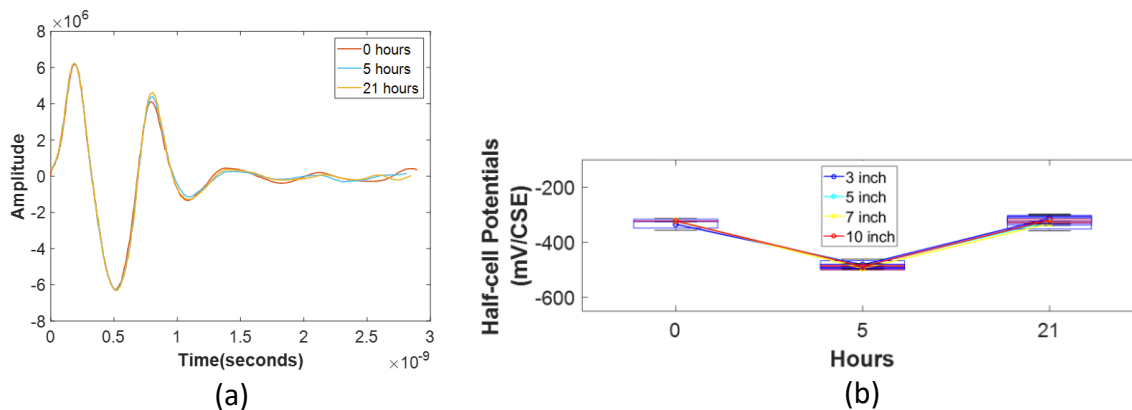
The results from AC-T1, -T2, -T3, -T4, -T5, and -T6 revealed the significant influence of the applied current on accelerating corrosion. In AC-T5 and AC-T6, specimens subjected to constant voltage exhibited reduced values in the signal processing analysis parameters, including EM wave energy, amplitude, peak frequency, and center frequency. A similar trend was also observed in the numerical simulation of the model developed in Section 5.2.3. This confirms that EM wave behavior can be representative of the variations in both active and passive states of rebar corrosion.

#### 5.3.1 Experimental data analysis: AC-T1, -T2 & -T3

The accelerated corrosion test, AC-T1, exhibited a rapid corrosion occurrence within a single day, manifesting with visible corrosion particles adhering to the rebar upon removal from the electrolyte solution. Following cleaning as shown in Figure 5.12, weight measurements revealed a 15% mass reduction for the 16mm rebar and a 32% reduction for the 10mm rebar. These findings underscore the efficacy of employing higher constant voltage/current for acceleration, bypassing the need for extended corrosion periods spanning years. Due to the swift corrosion progress, EM wave data collection at the 24-hour mark, including half-cell potential, could not be completed.

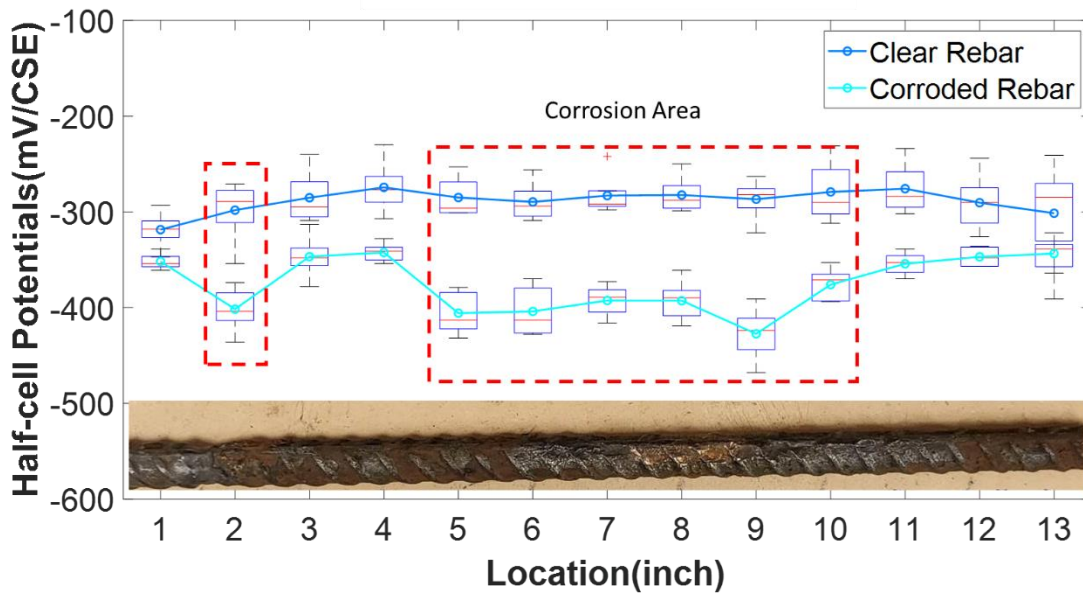


**Figure 5.12.** Rebar obtained after AC-T1 accelerated corrosion testing, showing a mass reduction of 15% for 16mm and 32% for 10mm.



**Figure 5.13.** Data obtained from different locations and times for AC-T1 testing: (a) EM wave response and (b) half-cell potentials.

In AC-T2, corrosion products were observed within 1.5 days, accompanied by fluctuations in half-cell potentials and surface resistivity. While EM wave measurements taken at 0, 5, and 21 hours did not display significant amplitude changes as shown in Figure 5.12(a), a comprehensive understanding of concrete rebar corrosion stages necessitated a more nuanced comprehension of the DC power supply, which prompted a deeper exploration of current and voltage literature for concrete rebar. Notably in Figure 5.14, half-cell potential measurements taken on the rebar after the concrete specimen breakdown exhibited a significant potential reduction within the corrosion-affected region.

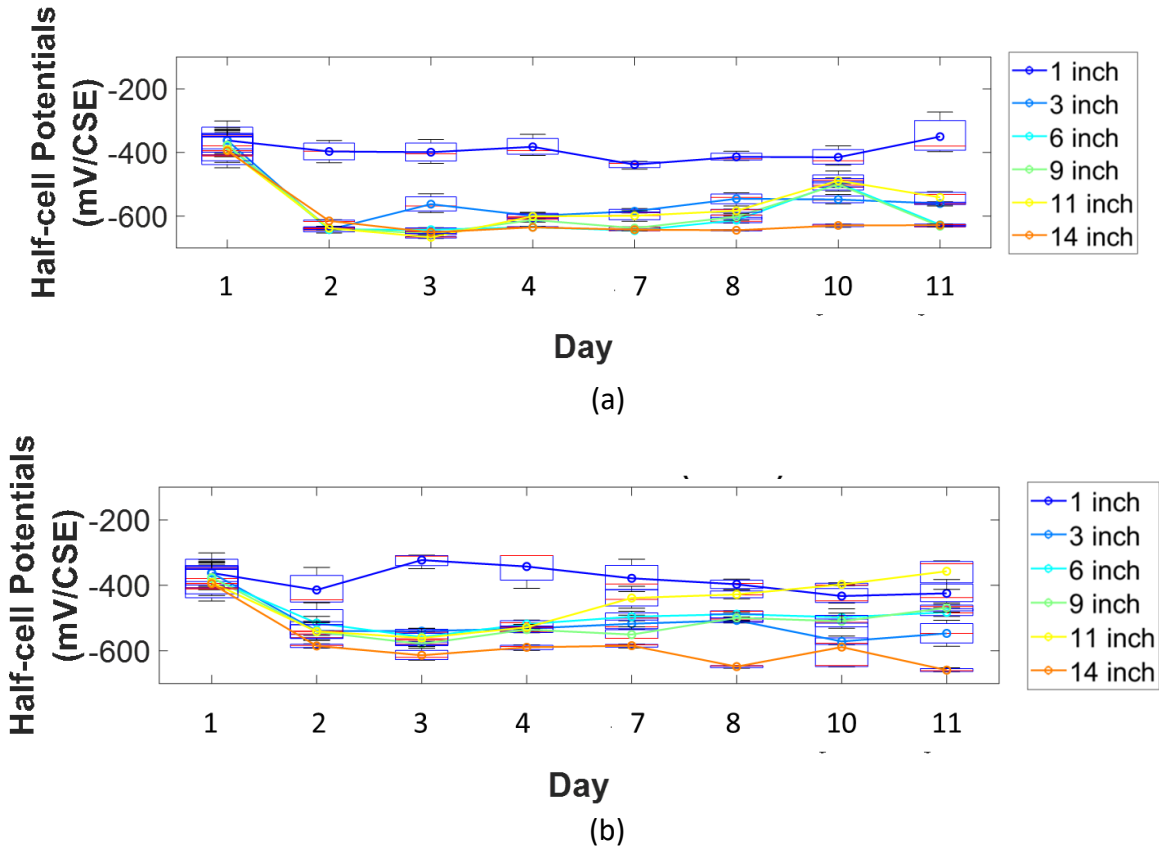


**Figure 5.14.** Half-cell potential evaluation of the rebar revealed a significant reduction in potential within corroded areas.

This literature review emphasized the importance of applying lower currents for controlled accelerated corrosion and considering specimen size for the applied current. These insights informed AC-T3, which resulted in desirable outcomes following a week of corrosion processes.

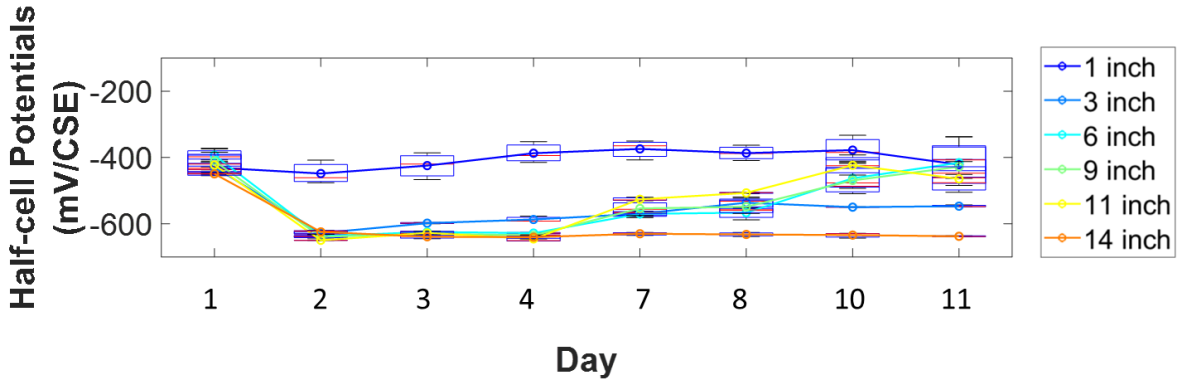


**Figure 5.15.** AC-T3 rebar with (a) rust particles attached to it, and (b) the rebar after the rust particles were cleaned.

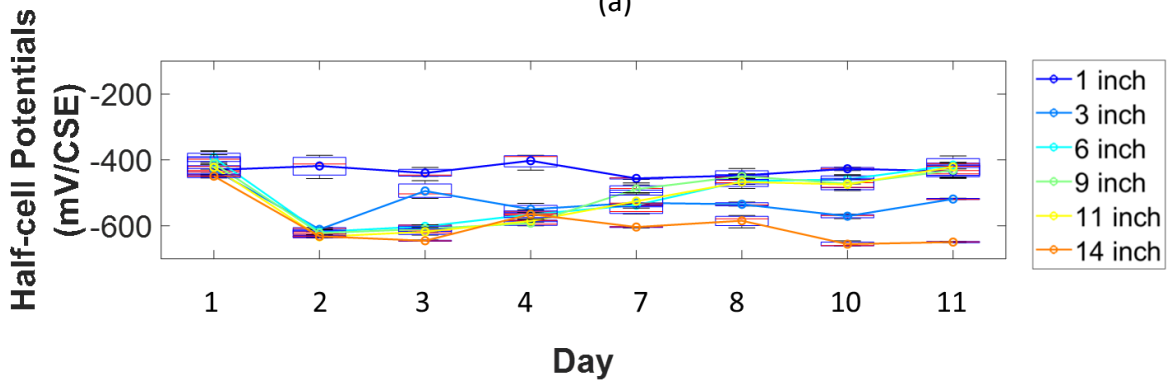


**Figure 5.16. Half-cell potential variation for the constant current rebar tested in AC-T3: (a) before cleaning and (b) after cleaning the rebar, highlighting the potential variation after the 7th day.**

AC-T3 demonstrated accelerated corrosion over 14 days. Half-cell potentials and rebar weight were measured post-cleaning, with potential values taken at 1, 3, 5, 7, 9, and 11 inches along the rebar length before and after cleaning (Figure 5.15). The potential reduction from -400mV to -600mV before cleaning, except at the 1-inch location, indicated a clear corrosion progression as shown in Figure 5.16 (a) & 5.18 (a). Post-cleaning, a similar pattern persisted until the 7th day (Figure 5.16 (b) & 5.18 (b)), after which the potential began to rise, suggesting the emergence of uncorroded rebar steel.



(a)



(b)

**Figure 5.17. Half-cell potential variation for the constant voltage rebar tested in AC-T3: (a) before cleaning and (b) after cleaning the rebar, highlighting the potential variation after the 7th day.**

Corrosion rates were computed based on current (Figure 5.18) and weight measurements (Figure 5.19), revealing an initial increase till 50<sup>th</sup> hour and subsequent decrease in corrosion rate under constant voltage till 300<sup>th</sup> hour, aligning with rebar mass reduction (Figure 5.20). Constant current, on the other hand, maintained a consistent corrosion rate.



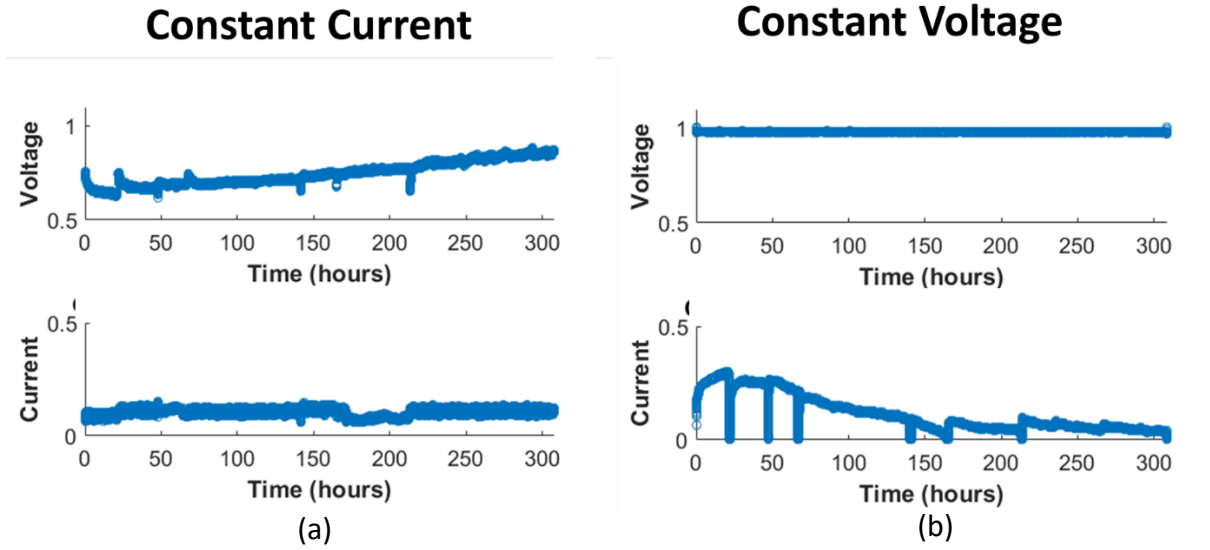


Figure 5.18. Voltage and current data were gathered using an Arduino Mega board for both (a) constant voltage and (b) constant current configurations. In the case of constant voltage, a reduction in current flow was observed as corrosion advanced, whereas under constant current conditions, the current remained stable while voltage varied in response to corrosion.

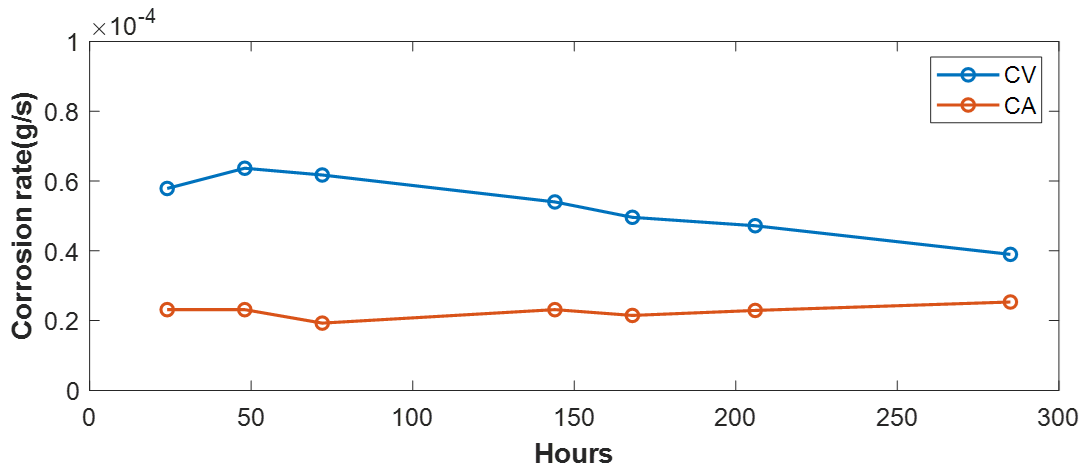
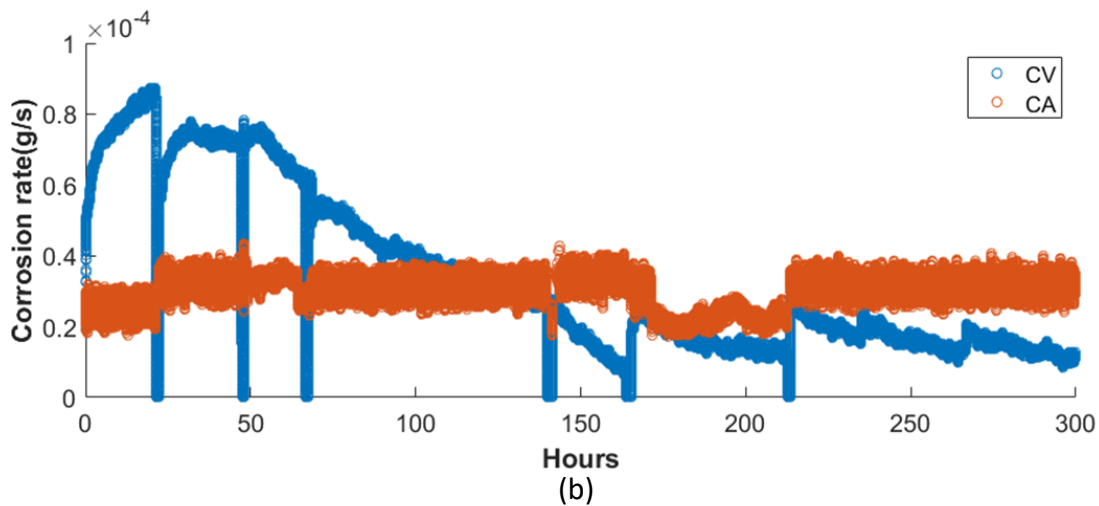
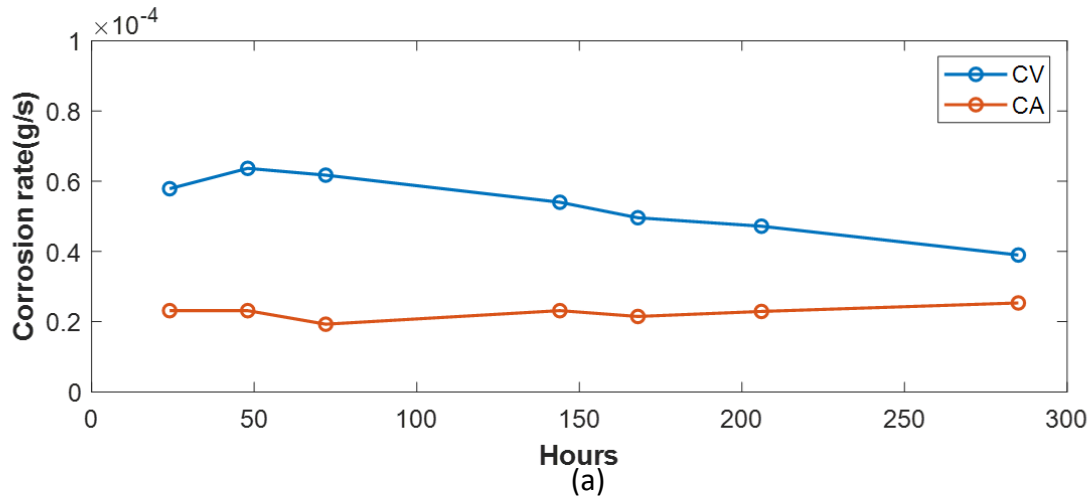


Figure 5.19. The measured weight of the clean rebar during AC-T3 testing is depicted by the blue line for constant voltage and the red line for constant current.



**Figure 5.20.** Corrosion rates obtained through (a) weight measurement and (b) current variation for AC-T3 reveal that in the case of constant voltage (CV), (c) the corrosion rate decreases (blue line), whereas in the constant current scenario, the rate remains relatively consistent (red line).

### 5.3.2 Experimental data analysis: Early age concrete

AC-T4 entailed 18 days of accelerated corrosion for CR10 and 36 days for CR16. Both specimens were halted upon abrupt declines in half-cell potential values of -600mV. Early cracks were visible on the 9th and 16th days for CR10 and CR16, respectively, accompanied by corrosion particles emanating from the rebar tops. Concrete breakage on the 36th day disclosed severe, localized corrosion along the rebar length as shown in Figure 5.21 and also variation in rebar diameter (Figure 5.23), with CR10 exhibiting more

pronounced corrosion, reflecting a mass reduction of 24% compared to CR16's 9.25% (Figure 5.22). Visual inspection revealed corrosion primarily leaking through cracks rather than adjacent aggregate areas.

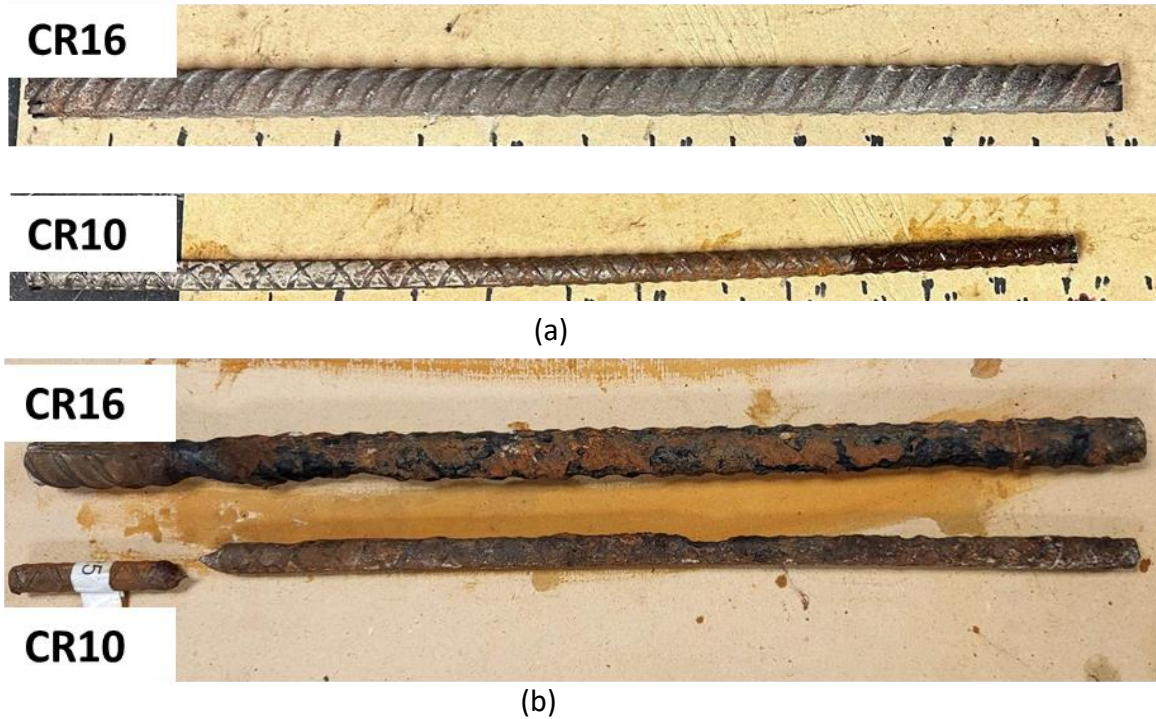


Figure 5.21. Photos indicate corrosion progression in the rebar embedded within the concrete (a) before corrosion and (b) after corrosion for CR10 and CR16 specimens of AC-T4 testing.

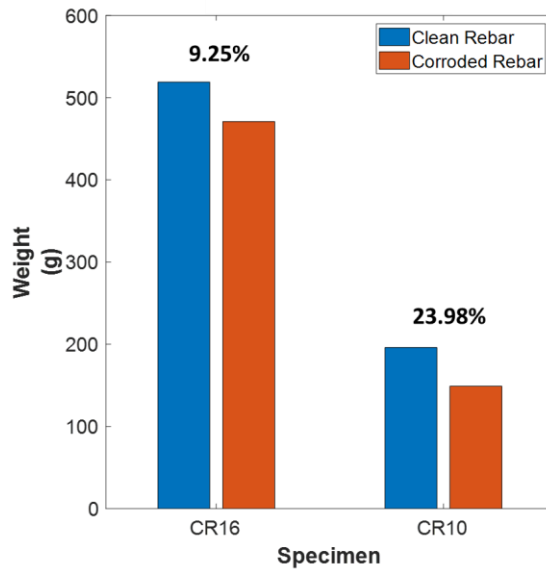
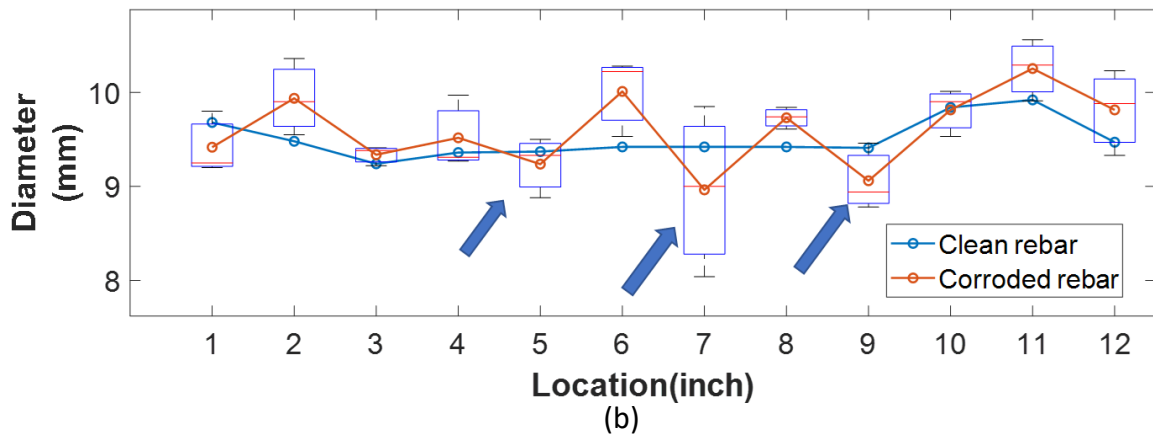
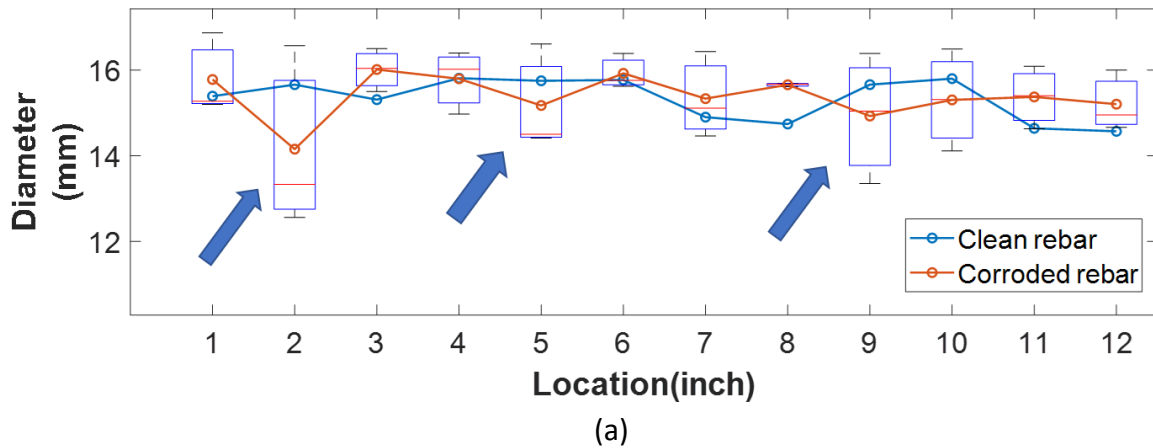


Figure 5.22. Mass reduction of the rebar due to accelerated corrosion in AC-T4.



**Figure 5.23. Rebar diameter variation of (a) CR10 and (b) CR16, with the observed reduction in diameter marked by arrows when measured around the rebar.**

EM waves, half-cell potential, and surface resistivity were collected at four specified locations for each specimen: A, B, C, and D. These locations were strategically chosen at 3, 6, 9, and 11 inches, covering the top, middle, and bottom sections of the rebar within the concrete. In both cases, the half-cell potential exhibited a gradual increase over time as shown in Figure 5.24. Even as cracks began to form, CR10 showed a decline in half-cell potential values after the 14th day, while CR16 displayed a more significant reduction after the 22nd day, potentially indicating the onset of heavy corrosion.

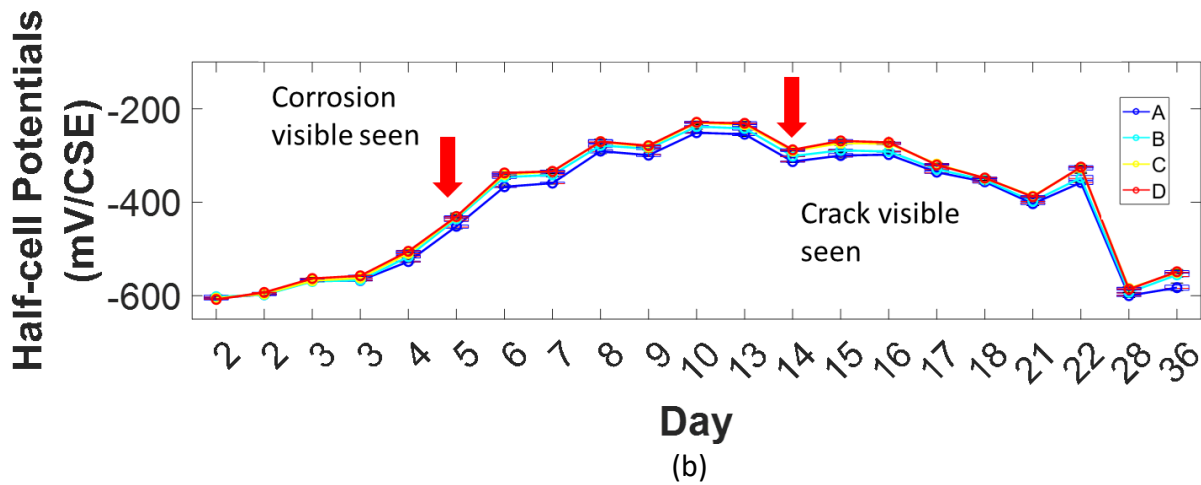
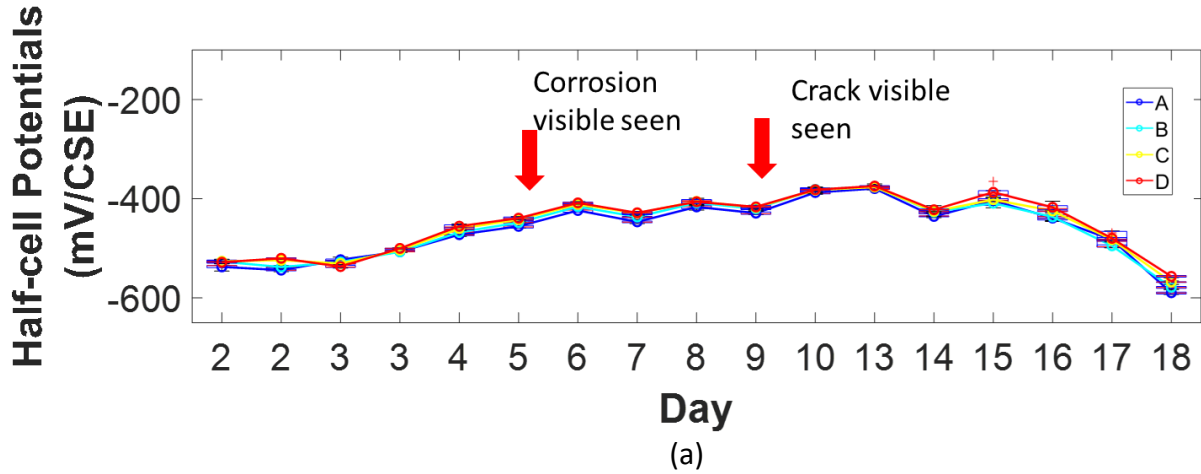
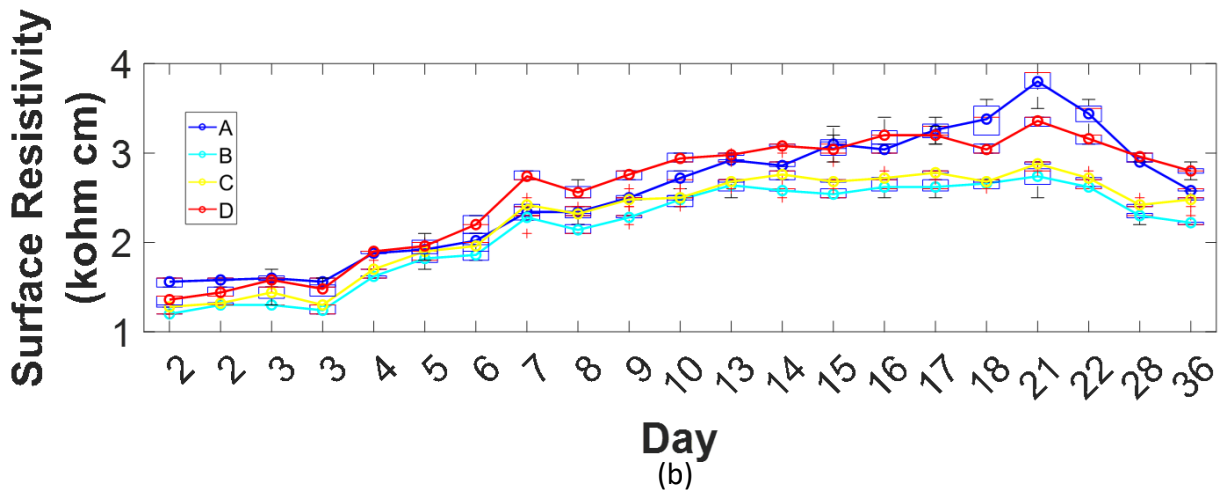
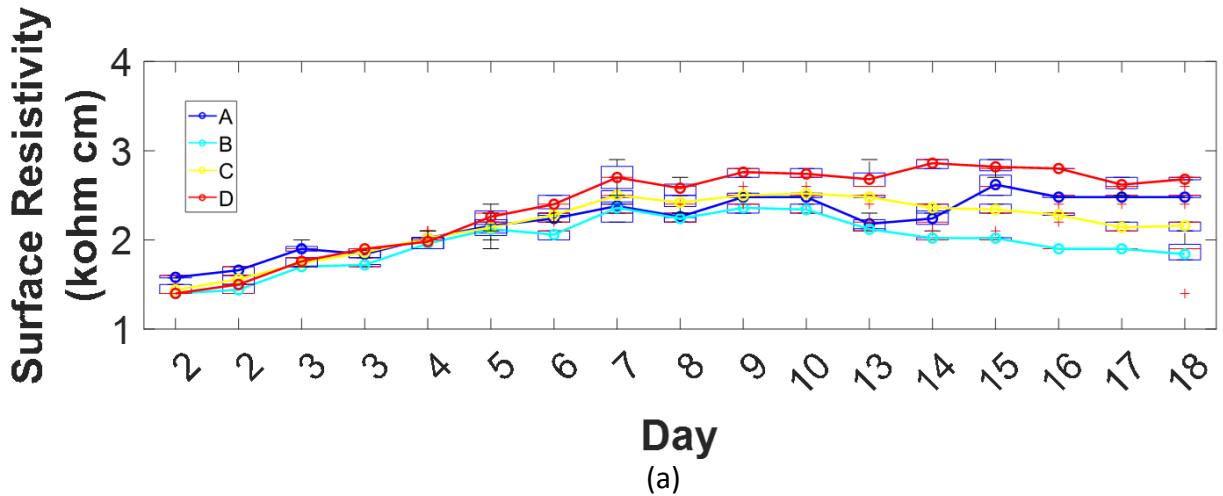


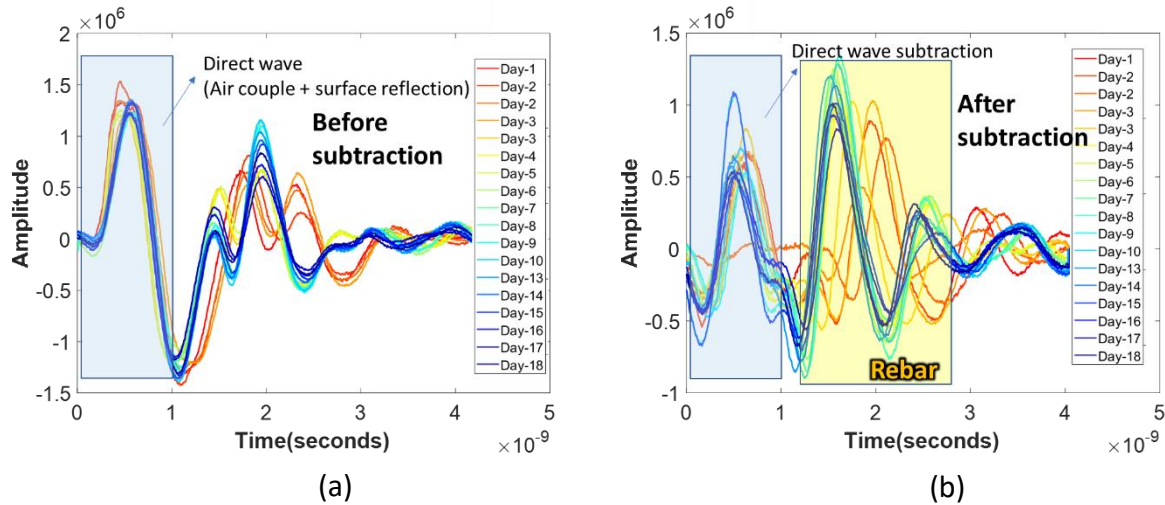
Figure 5.24. Collected half-cell potential data at locations A, B, C, and D are presented over the testing period for (a) CR10 and (b) CR16 specimens of AC-T4

Similarly, the surface resistivity (Figure 5.25) for both CR10 and CR16 demonstrated a gradual increase during the concrete hardening period. However, an abrupt decline in resistivity, similar to the potential drops observed on the 14th and 22nd days for CR10 and CR16 respectively, was also noted.

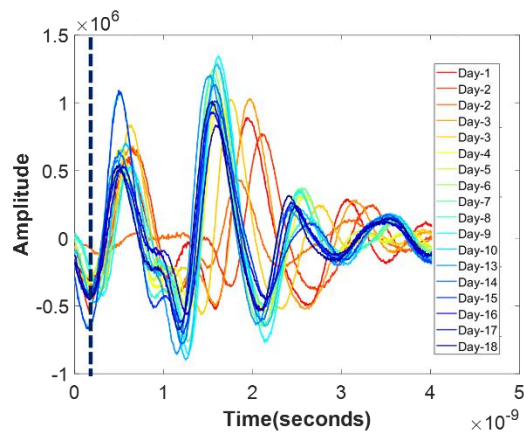


**Figure 5.25.** Surface resistivity data collected at locations A, B, C, and D are plotted over the testing period for (a) CR10 and (b) CR16 specimens of AC-T4.

Subsequent signal analysis of the EM waves collected at each location was performed using MATLAB. The initial step involved assembling the A-scans corresponding to the rebar reflections from each B-scan obtained throughout the experiment. After grouping the A-scans for each day of CR16 and CR10, signal subtraction was applied to mitigate signal attenuation as the EM waves passed through the medium. This subtraction effectively eliminated noise and surface reflections, enhancing the clarity of the rebar signal (Figure 5.26). Synchronization was then performed to align all EM wave responses with respect to the first negative peak (Figure 5.27), ensuring accurate time alignment and preventing any misalignment in time readings.

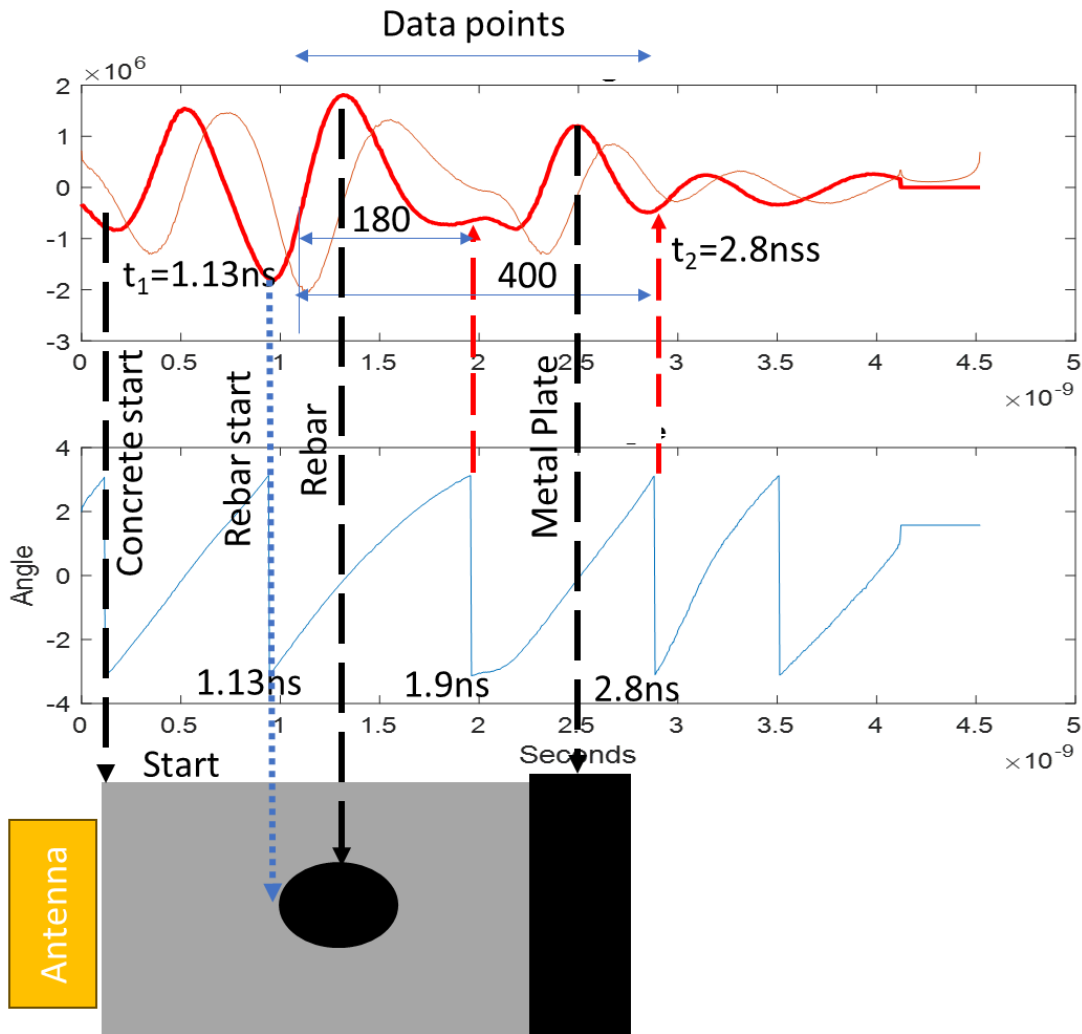


**Figure 5.26. Illustrating the EM wave signal transformation (a) before subtraction and (b) after subtraction, acquired for CR10 at location B. This process effectively eliminates noise and direct wave, providing a clearer resolution of the rebar reflection.**



**Figure 5.27. The EM waves were synchronized with the first negative peak (dotted line) to obtain a clear variation in the rebar responses.**

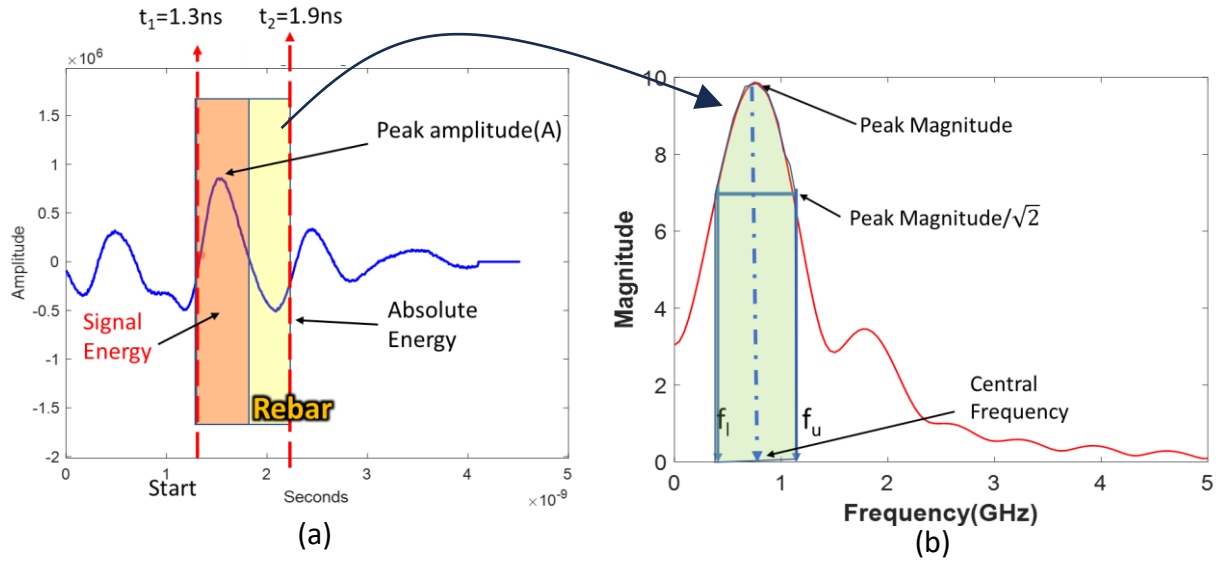
The post-processing analysis utilized the obtained signals after subtraction. The first analytical step involved determining the optimal time window for the signal, essential for statistical parameter study. This time window was identified through phase shift analysis of the signal using the Hilbert transform. By plotting the angle of phase shift alongside the signal, the desired time window for post-processing EM wave analysis was identified as shown in Figure 5.28.



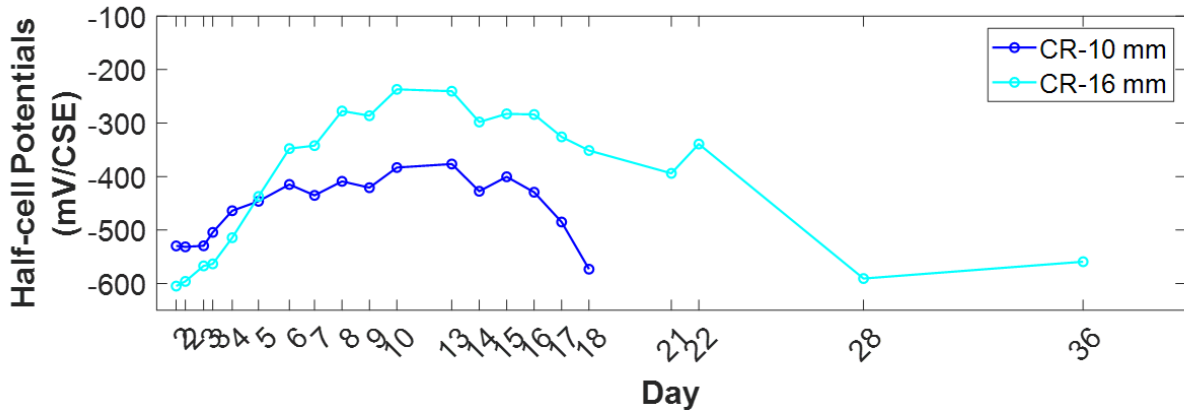
**Figure 5.28.** Phase angle analysis of the EM wave is conducted to identify the optimal time window corresponding to the medium transition. This selected time window is then employed for the subsequent signal post-processing.

Within this selected time window, a range of signal attributes were examined, encompassing signal energy, maximum amplitude, peak frequency magnitude, center frequency, and half-bandwidth of the peak frequency, as illustrated in Figure 5.29. This extensive analysis sought to provide deeper insights into the characteristics and dynamics of the EM wave responses in connection with the corrosion process. Given the substantial dataset, averaging was conducted for each location to enhance the clarity of signal processing and facilitate a better understanding. An illustrative example is presented where the data in Figure 5.24 are averaged and combined into a single plot, as shown in Figure 5.30.



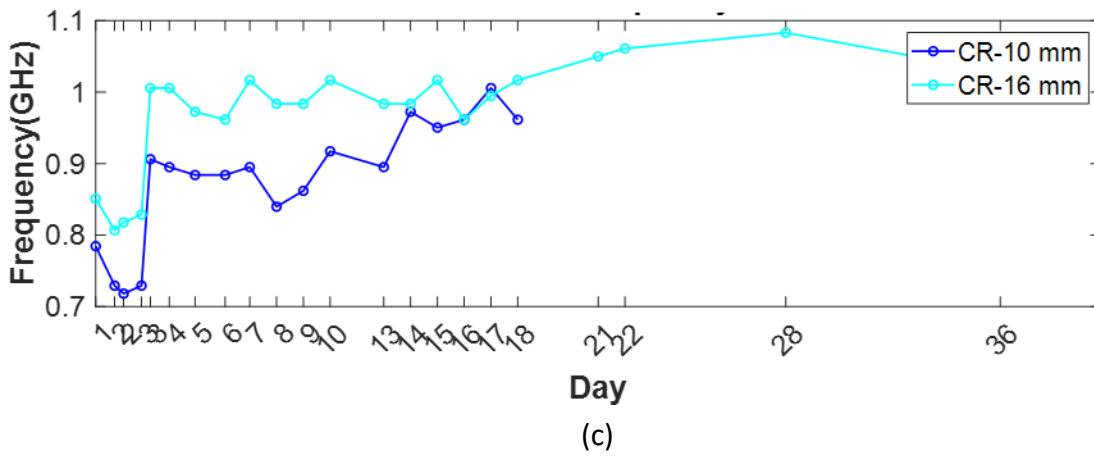
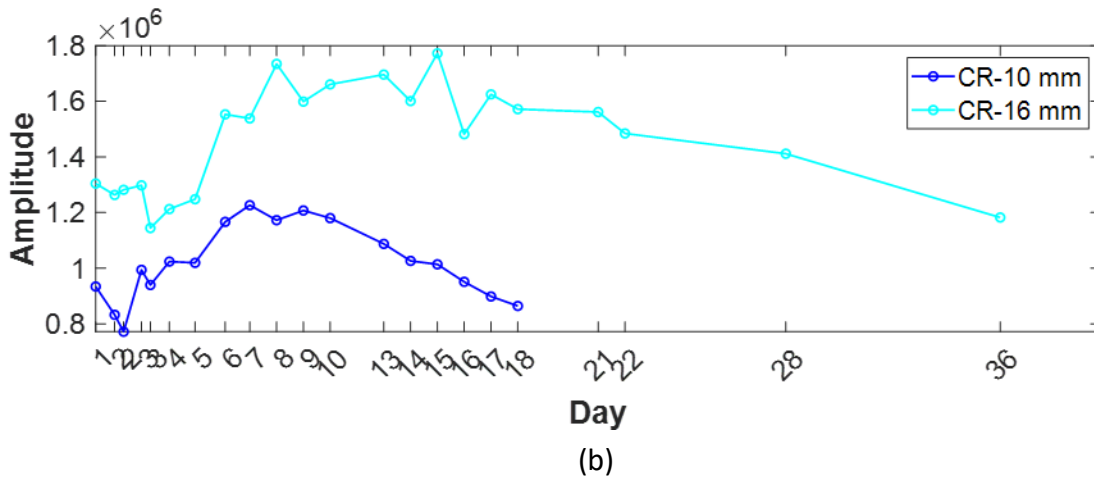
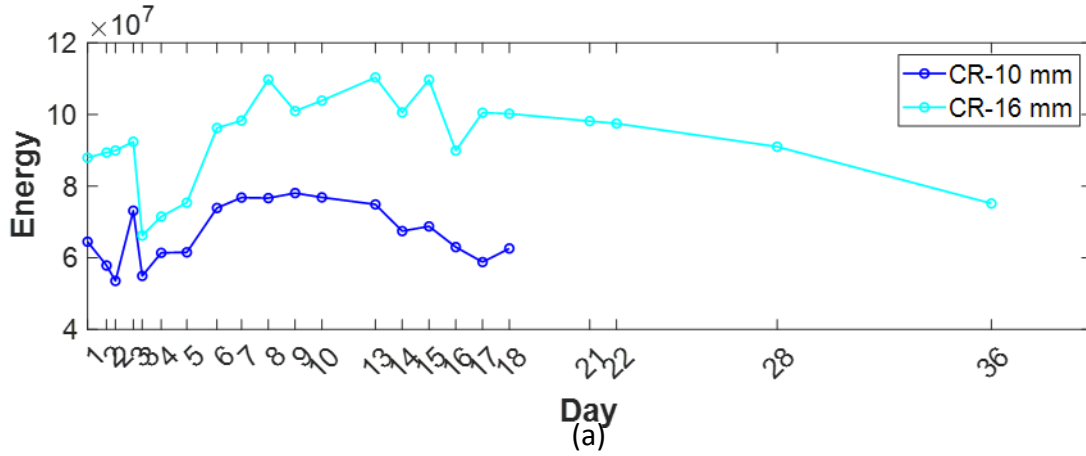


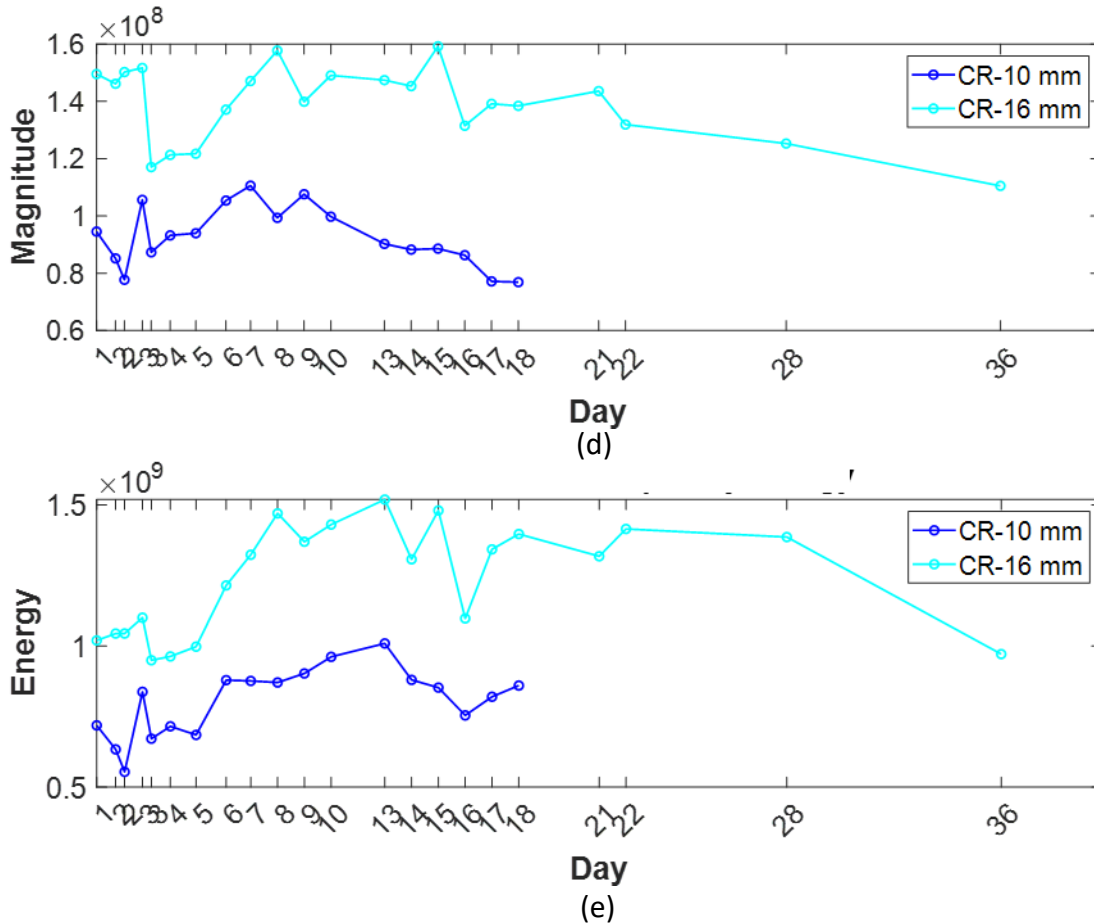
**Figure 5.29.** Signal post-processing analysis of (a) single EM wave involves determining the amplitude, signal energy, and time window for the respective (b) FFT. Spectrum analysis yields the half-bandwidth and central frequency.



**Figure 5.30.** Averaged half-cell potential data grouped by locations for CR10 and CR16 specimens of AC-T4.

EM waves, half-cell potentials, and surface resistivity were gathered at four locations (A, B, C, D) on each specimen, covering top, middle, and bottom sections of the rebar within the concrete. Half-cell potentials displayed gradual increases until the 13th day, thereafter, showing declines similar to energy, frequency, and amplitude, consistent with rebar corrosion stages as illustrated in Figure 5.31. EM wave analysis revealed its utility in determining passive and active corrosion states, even in early-age concrete undergoing corrosion.



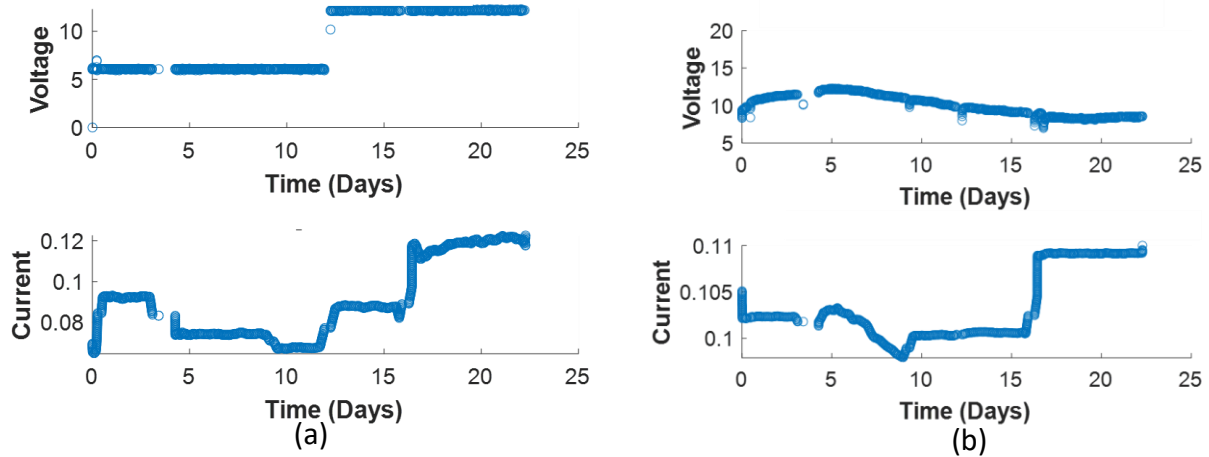


**Figure 5.31.** Signal post-processing analysis of the EM wave reveals the variations in signal attributes for the specimens tested in AC-T4. These attributes include (a) signal energy, (b) signal maximum amplitude, (c) center frequency, (d) peak frequency magnitude, and (e) half-bandwidth of frequency energy. This analysis provides insights into the dynamic behavior of EM wave responses in correlation with the corrosion process.

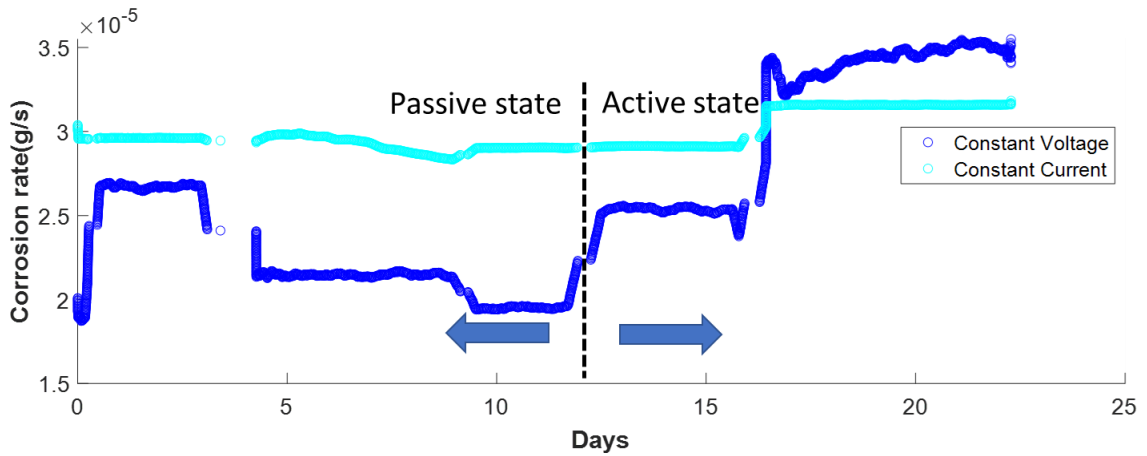
### 5.3.3 Experimental data analysis: Mature concrete

AC-T5 involved an accelerated corrosion process spanning 23 days, continuing until visible cracks emerged. Data collection occurred at four designated specimen locations: A, B, C, and D. An additional control specimen was introduced for reference, aiding the observation of variations in half-cell potential and surface resistivity. Similarly, to AC-T3, the voltage and current measurements conducted during AC-

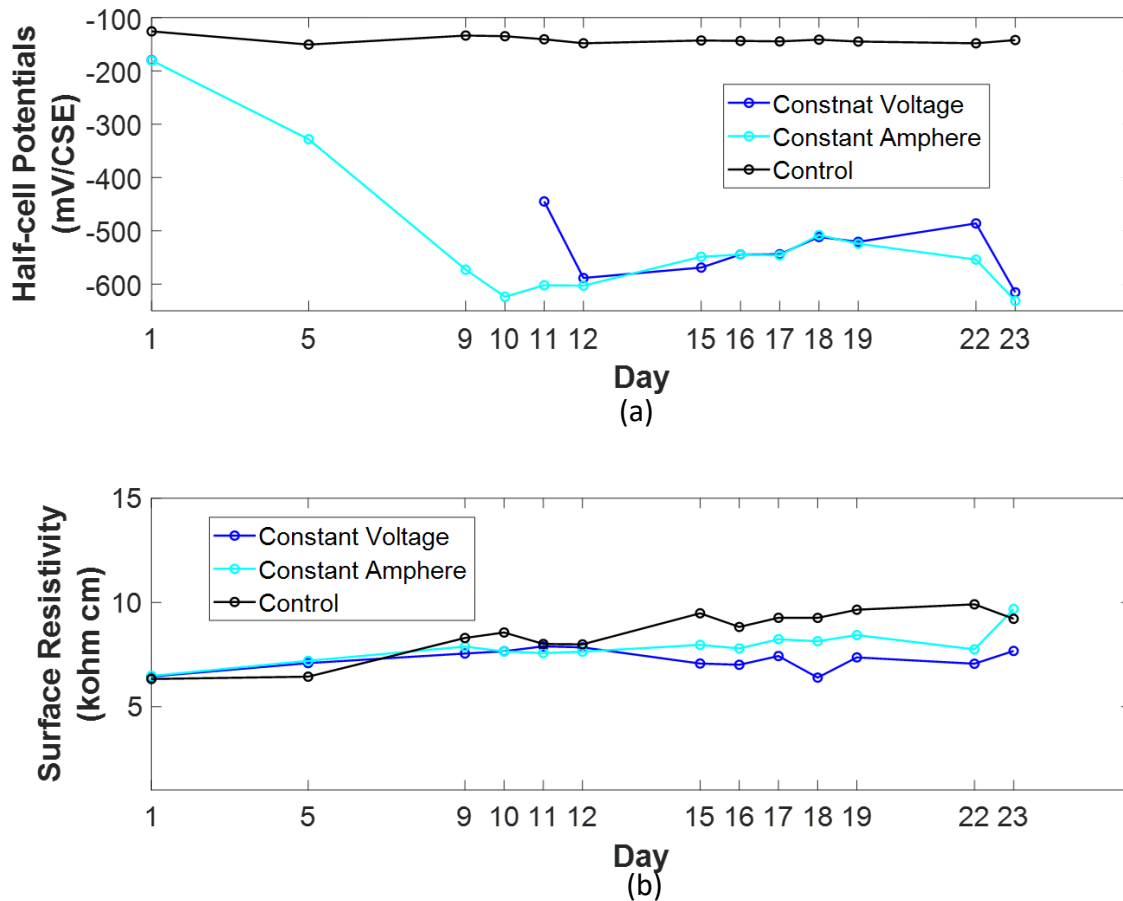
T5 demonstrated changes in current within both the constant voltage (CV) and constant current (CA) settings, indicating a clear transition from passive to active corrosion states.



**Figure 5.32.** Voltage and current data were collected for AC-T5: (a) constant voltage and (b) constant current configurations.



**Figure 5.33.** Corrosion rates obtained from current variation in AC-T5 reveal that in the case of constant voltage (blue line), the corrosion rate remains passive until the 10th day and then progresses to an active corrosion state, whereas in the constant current scenario, the rate remains relatively consistent (red line).

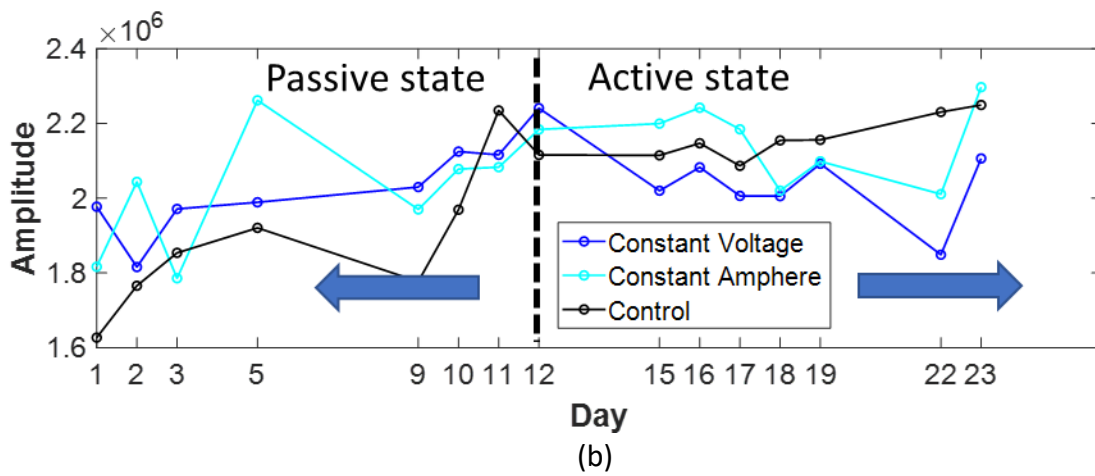
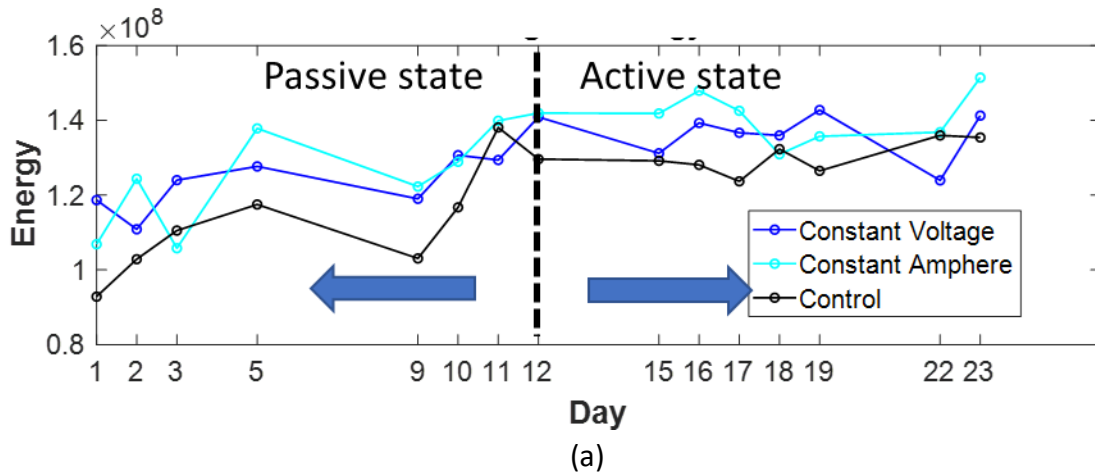


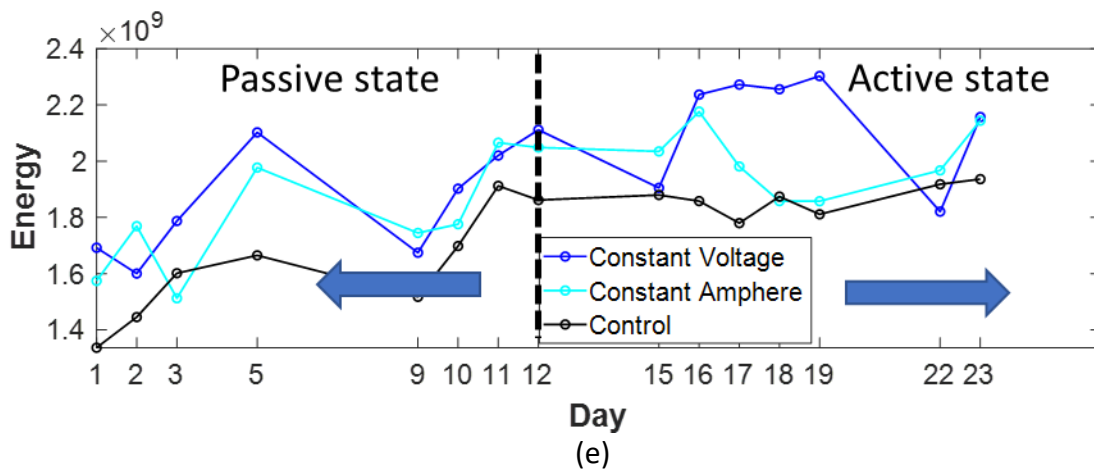
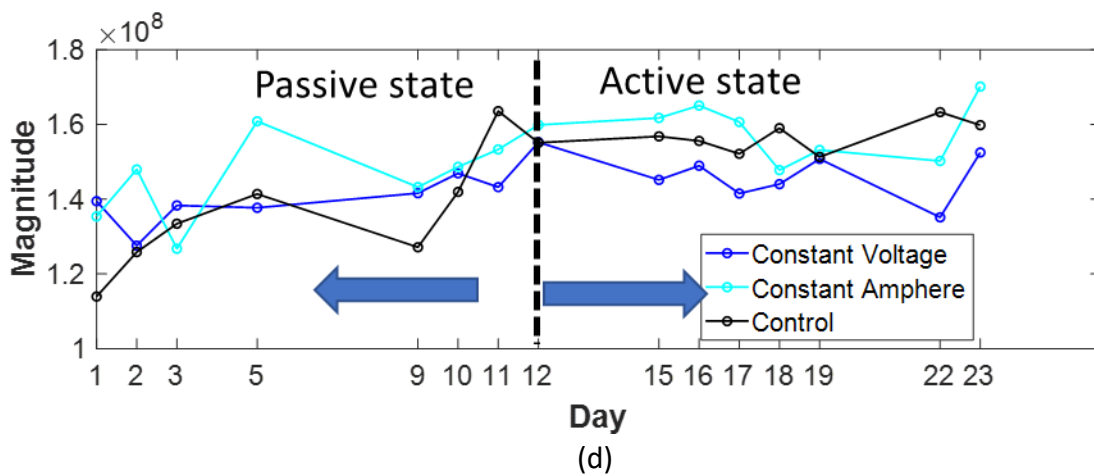
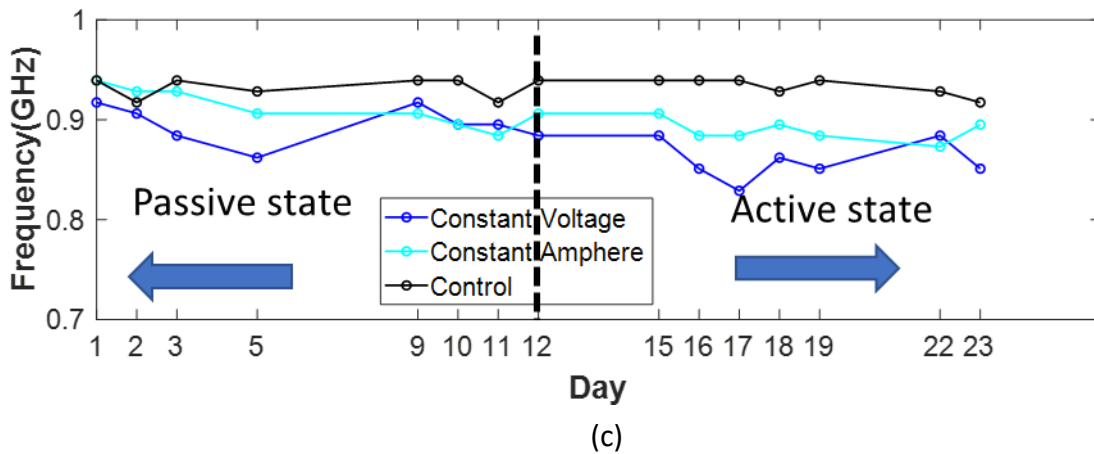
**Figure 5.34. Specimens subjected to accelerated corrosion in AC-T5 for constant voltage and current along with reference control specimen measured: (a) half-cell potentials and (b) surface resistivity measured for specimens of AC-T5. Half-cell potential indicates that the specimen undergoes active corrosion after the 12th day, consistent with the corrosion rate trend.**

However, assessing half-cell potentials during passive corrosion stages proved challenging due to substantial potential fluctuations between the cathode and anode. This led to inaccuracies in measurements, necessitating extended drying periods for improved data collection, which commenced on the 5th day (Figure 5.34(a)). Beyond the 9th day, half-cell potential evaluations became more reliable, although readings approached the active corrosion state.

The analysis of half-cell potential proved instrumental in identifying the onset of the specimen's active corrosion state. The examination of voltage and current data during this phase yielded clear results,

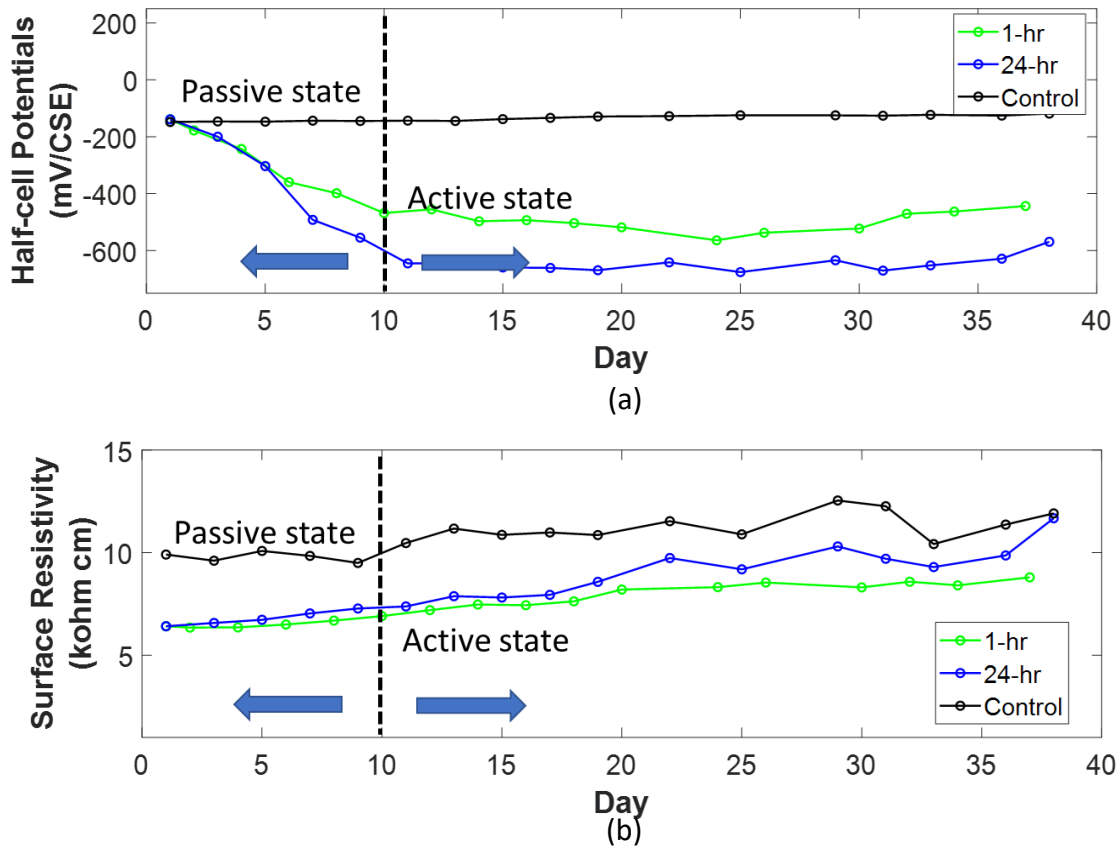
indicating a significant shift in corrosion rate from passive to active corrosion on the 12th day (Figure 5.33), especially pronounced in the constant voltage scenario. The EM wave analysis also demonstrated a gradual decrease in the duration of the active corrosion state for both constant voltage and current scenarios as illustrated in Figure 5.35. Nonetheless, it is important to acknowledge that while this analysis offers valuable insights, practical challenges may arise when attempting to obtain corrosion rates under real-world field conditions.





**Figure 5.35.** The signal post-processing analysis of the EM wave provides insights into the changes in signal attributes for the specimens tested in AC-T5 during both the passive and active corrosion states. These attributes encompass (a) signal energy, (b) signal maximum amplitude, (c) center frequency, (d) peak frequency magnitude, and (e) half-bandwidth of frequency energy.

Similar to AC-T4, AC-T6 involved testing at four distinct locations over a span of 38 days to simulate accelerated corrosion. Considering the challenges encountered during AC-T5, the evaluation of half-cell potential and surface resistivity readings was undertaken at 1-hour and 24-hour intervals (Figure 5.36). The surface resistivity data indicated a consistent increase in values throughout the experiment for both constant voltage (CV) and constant current (CA) specimens, suggesting that concrete hardening effects may affect surface integrity compared to AC-T4. In the case of the CV specimen, the half-cell potential exhibited an initial passive state for a few days before gradually transitioning into an active corrosion state. On the 10th day, the CV specimen entered a pronounced active corrosion state, with a notable -100mV difference between the 1-hour and 24-hour measurements. Both the 1-hour and 24-hour readings displayed a similar trend in potentials.

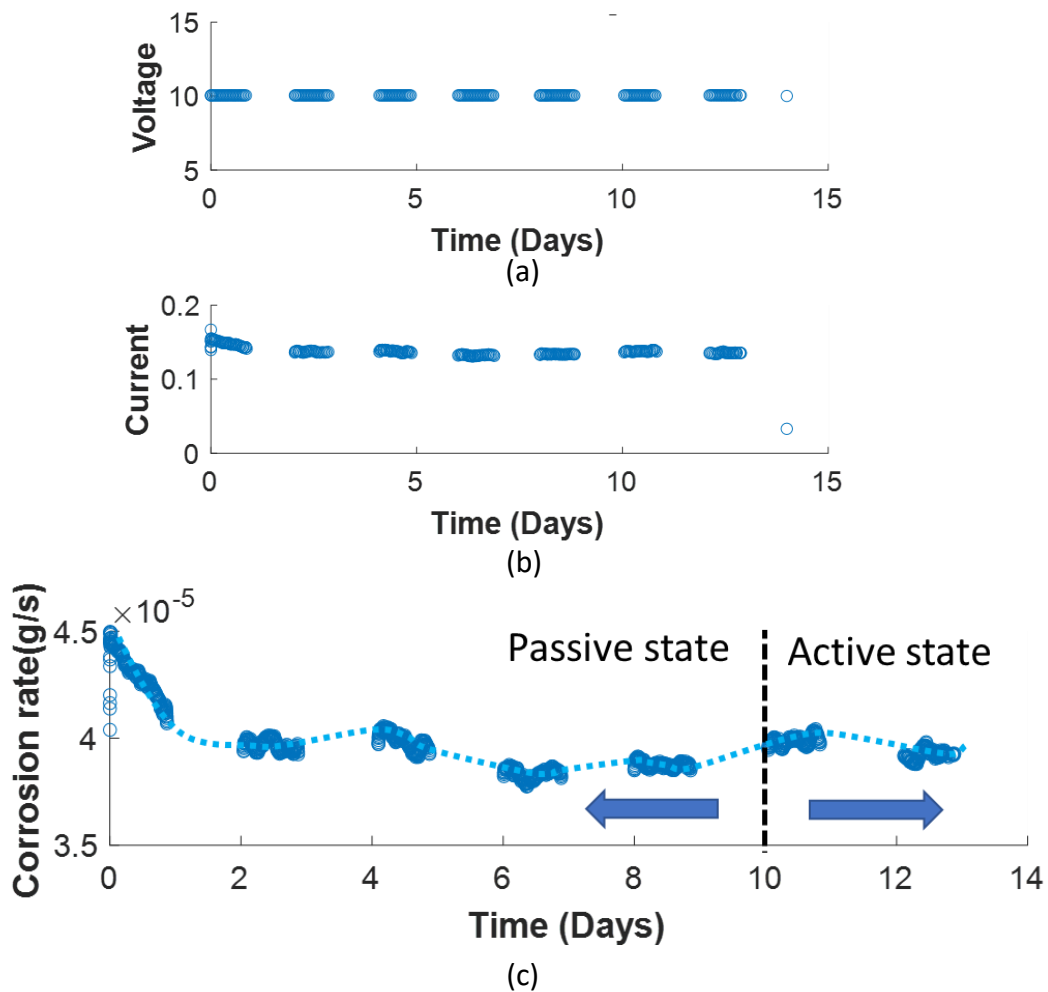


**Figure 5.36.** Specimens subjected to constant voltage in AC-T6 at both 1-hour and 24-hour intervals along with reference control specimen measured: (a) half-cell potentials and (b) surface resistivity. The half-cell potential data indicates that the specimen transitions into an active corrosion state after the 10th day.

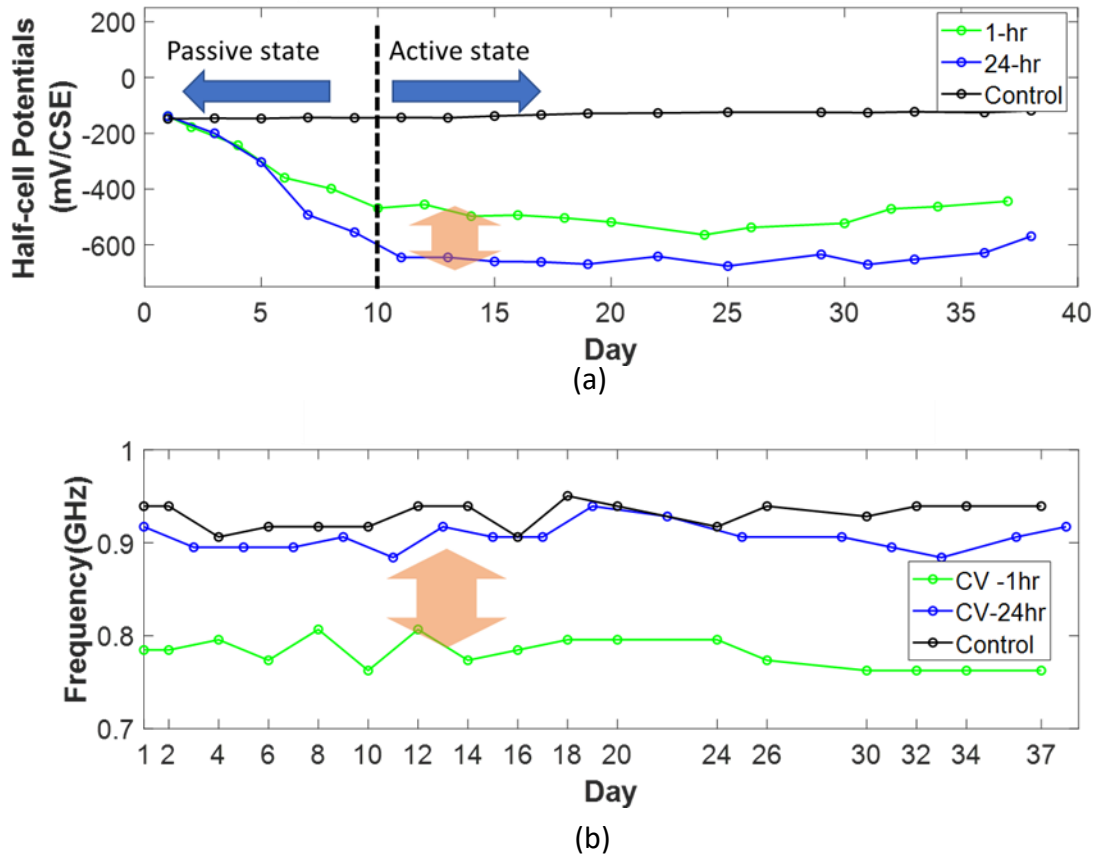


The EM wave analysis for AC-T6 followed the steps outlined in the post-processing method used for AC-T4 EM wave analysis. The analysis was conducted separately for CV and CA. Notably, when assessing the impact of moisture, the EM wave analysis of AC-T6's embedded rebar under various conditions – involving one-hour and 24-hour dry periods to mitigate moisture effects – revealed consistent trends in terms of half-bandwidth energy and central frequencies during active corrosion phases (Figure 5.38).

Given the moisture elimination achieved through the 24-hour drying period, this EM wave response was chosen for subsequent analysis. In the context of constant voltage, the corrosion rate displayed an initial decline during the passive state. However, upon entering the active corrosion state, the corrosion rate exhibited an ascending trend (refer to Figure 5.37).



**Figure 5.37.** AC-T6 under constant voltage: (a) voltage data collected (b) current data collected (c) variation in corrosion rate between the passive and active states.



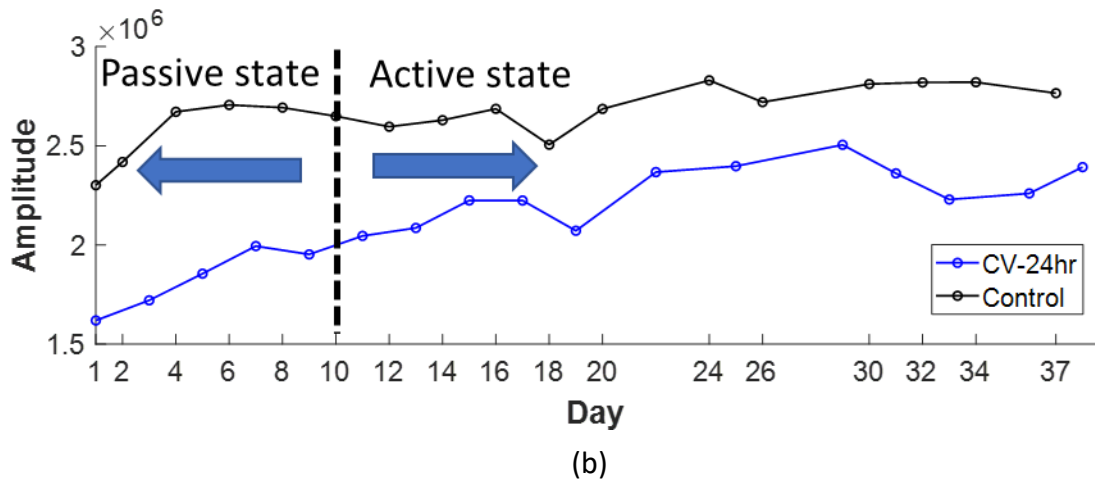
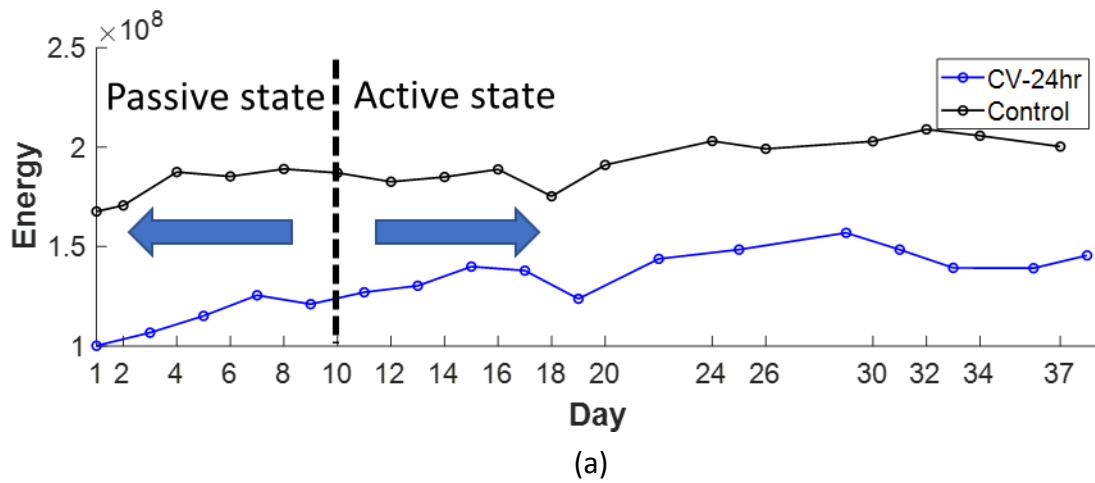
**Figure 5.38: The impact of moisture variation of AC-T6 between a 1-hour drying period and a 24-hour drying period is depicted in: (a) half-cell potentials, and (b) center frequency.**

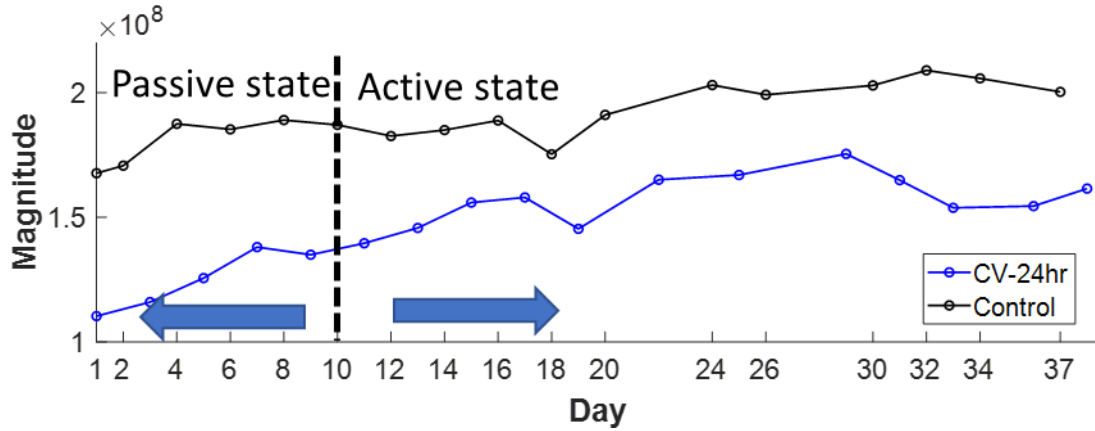
The EM waves reveal an interesting trend: the signal energy, amplitude, peak frequency magnitude, and center frequency all demonstrate a consistent increase during the initial hour of drying. This trend persists and extends until the 20th day, even during the active corrosion state, as depicted in (Figure 5.39). Following this 20-day period, these values undergo a gradual decline, akin to the response observed in AC-T5.

However, a notable distinction arises when comparing the 24-hour readings with those of the control specimen. In the case of the 24-hour drying period, the amplitude (Figure 5.39 (b)), signal energy (Figure 5.39 (a)), and peak frequency magnitude (Figure 5.39 (d)) exhibit a more pronounced disparity between them. This discrepancy could potentially be attributed to the increased impedance resulting from the higher

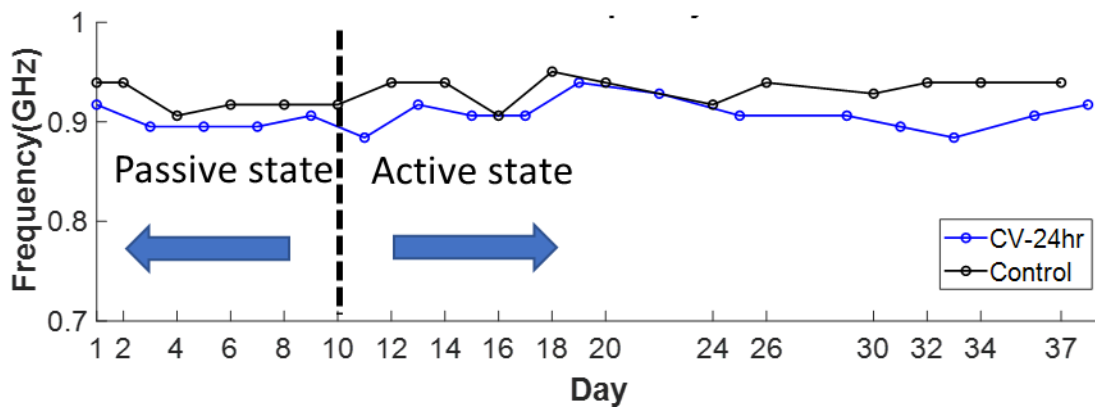
surface resistivity observed in the 24-hour specimens (Figure 5.36 (b)), when contrasted with the control specimen.

Remarkably, it's worth highlighting that solely the half bandwidth energy (Figure 5.39 (e)) and central frequency (Figure 5.39 (c)) exhibit a parallel alignment on day 1 within the experimental phase, observed in both the control and 24-hour specimen cases. As the experiment unfolds, these two parameters then begin to vary consistently throughout the duration. Undoubtedly, these specific parameters hold a significant role in comparing and validating both the passive and active corrosion states.

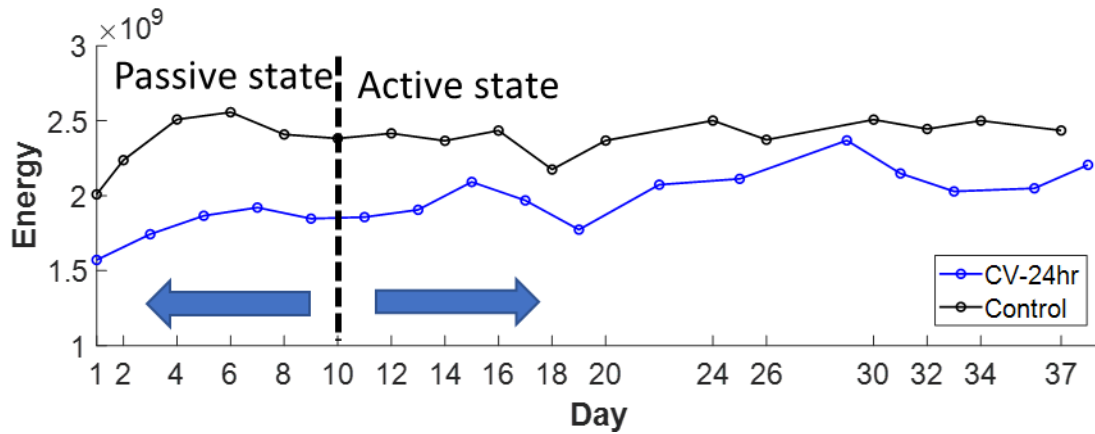




(c)



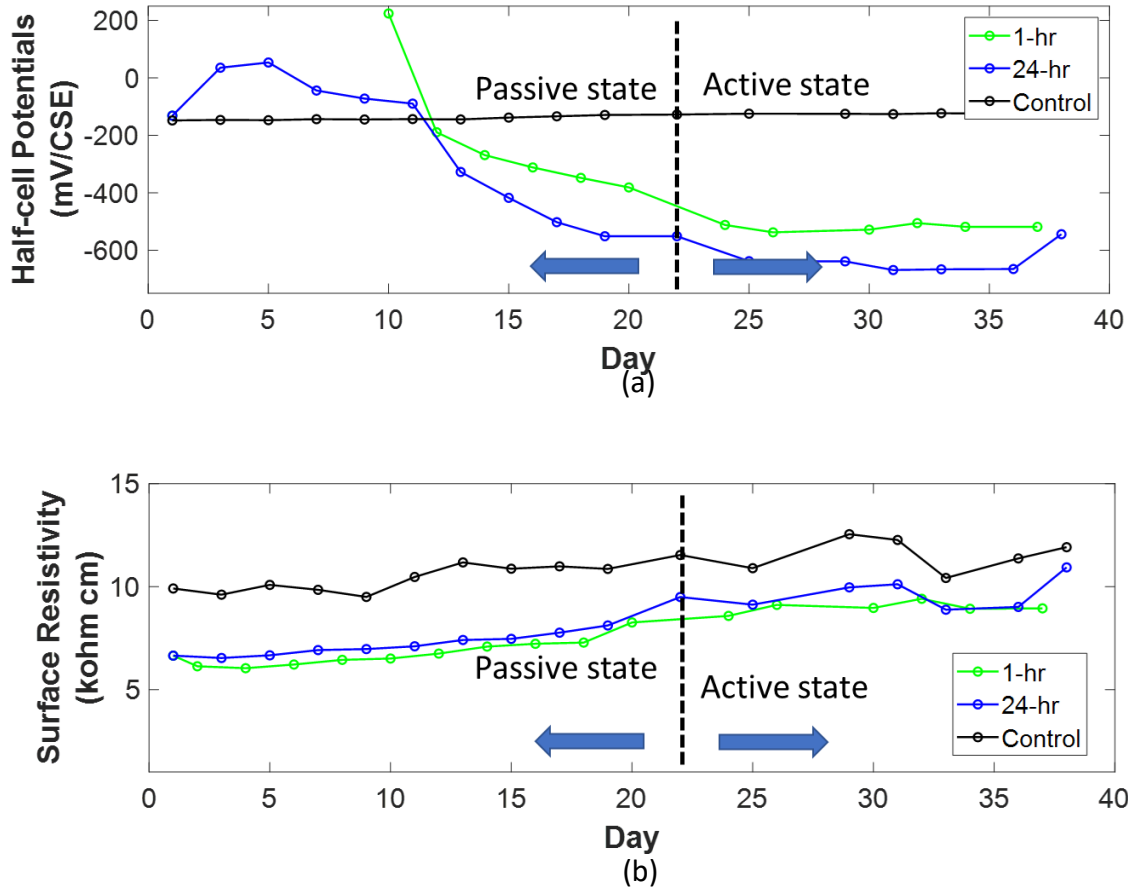
(d)



(e)

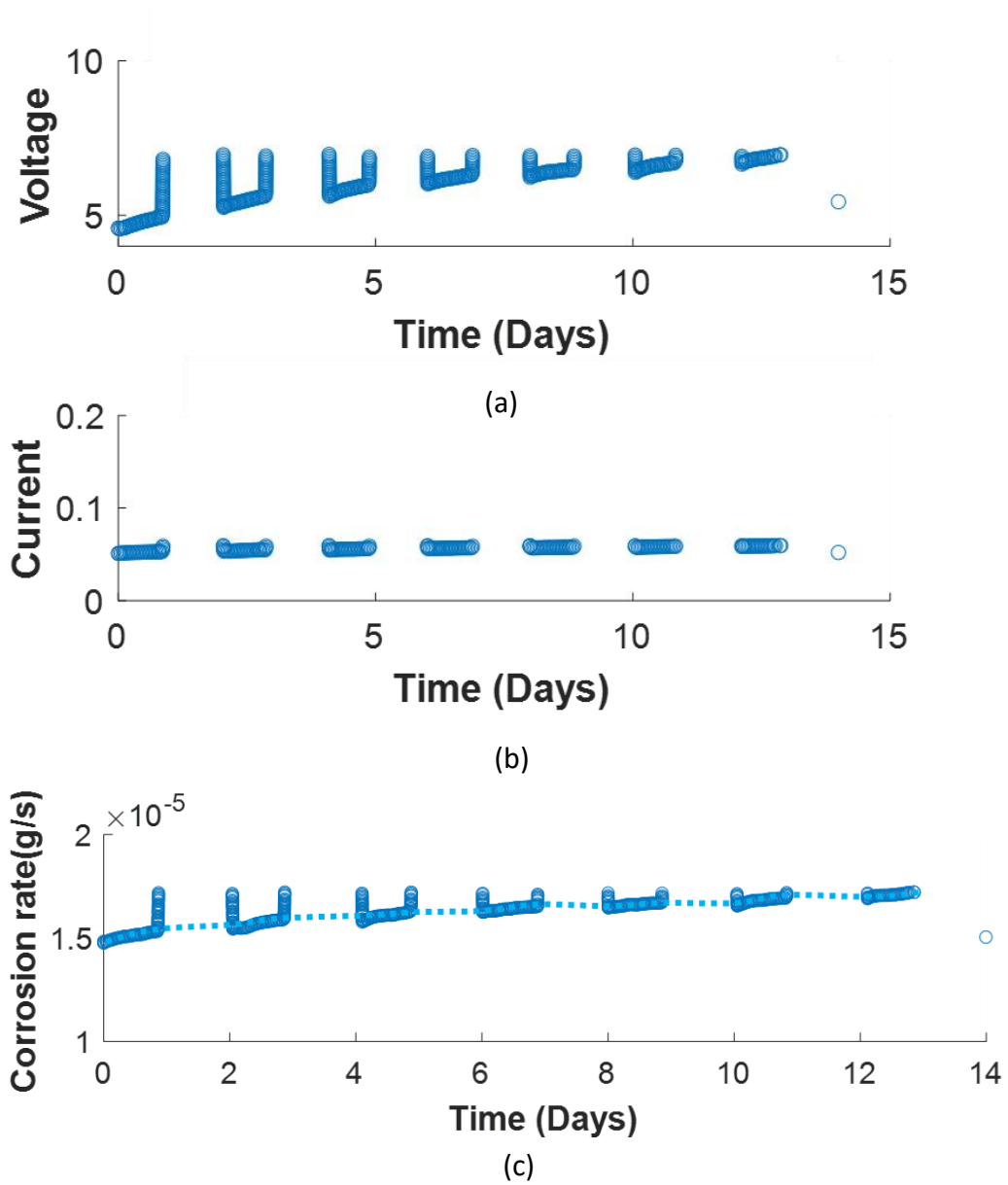
**Figure 5.39.** The signal post-processing analysis of the EM wave under constant voltage provides insights into the changes in signal attributes for the specimens tested in AC-T6 during both the passive and active corrosion states. These attributes encompass (a) signal energy, (b) signal maximum amplitude, (c) center frequency, (d) peak frequency magnitude, and (e) half-bandwidth of frequency energy.

For the CA specimen, the 1-hour half-cell potential readings were not measurable due to its high passivity until the 10th day (Figure 5.40). Subsequently, the evaluation became attainable. However, the 24-hour readings exhibited a clear passive state, consistent with findings from the literature review.

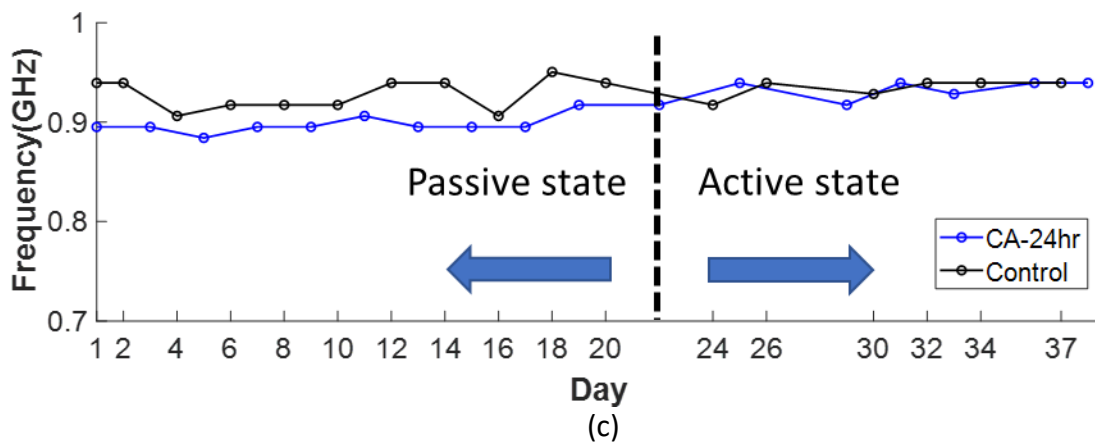
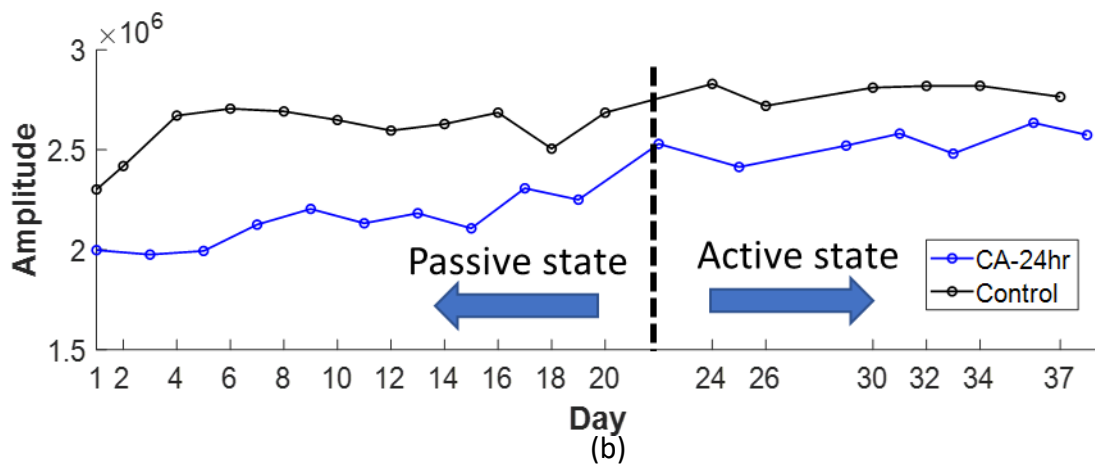
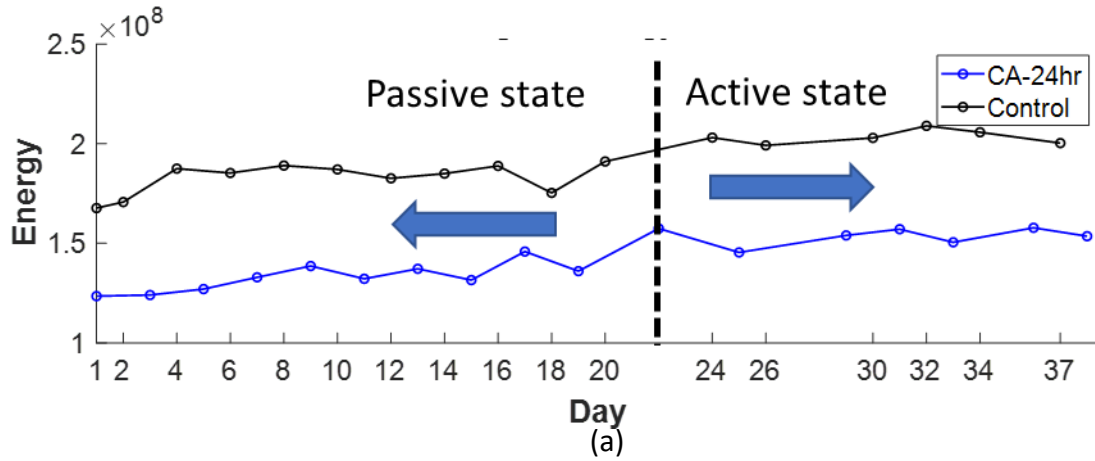


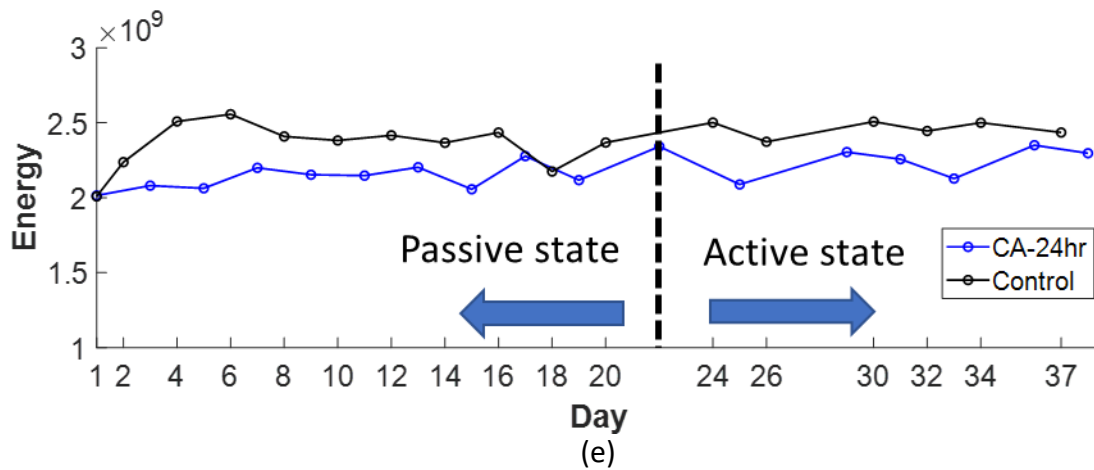
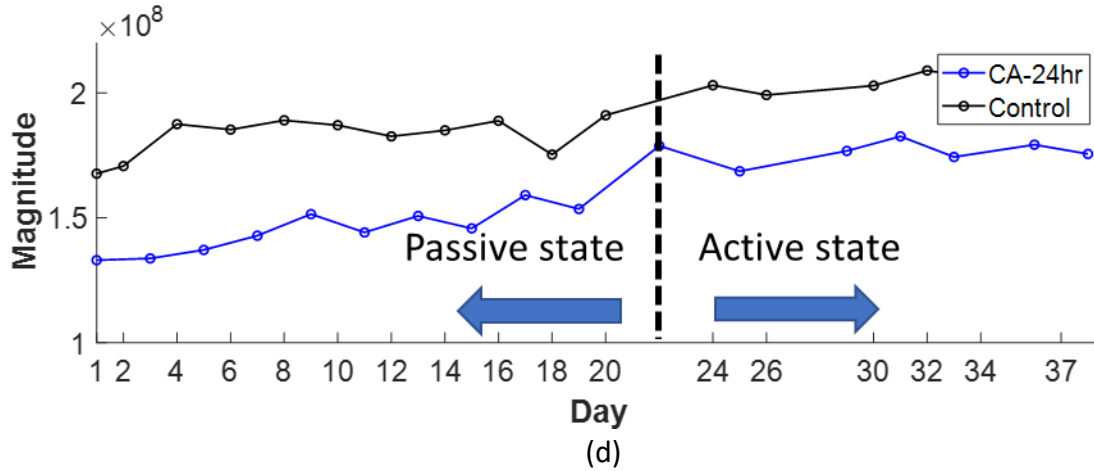
**Figure 5.40.** Specimens subjected to constant current in AC-T6 at both 1-hour and 24-hour intervals along with reference control specimen measured: (a) half-cell potentials and (b) surface resistivity. The half-cell potential data indicates that the specimen transitions into an active corrosion state after the 21st day.

In the case of the constant current specimen, both the 1-hour and 24-hour drying periods show a comparable increase in energy, amplitude, and magnitude (Figure 5.42). This observation is attributed to the slow corrosion rate associated with the constant current state (Figure 5.41), potentially necessitating extended corrosion analysis over an extended period.



*Figure 5.41. AC-T6 constant current study depicting: (a) voltage data collected, (b) current data were collected (c) steady state with corrosion rate.*





**Figure 5.42.** The signal post-processing analysis of the EM wave under constant current provides insights into the changes in signal attributes for the specimens tested in AC-T6 during both the passive and active corrosion states. These attributes encompass (a) signal energy, (b) signal maximum amplitude, (c) center frequency, (d) peak frequency magnitude, and (e) half-bandwidth of frequency energy.

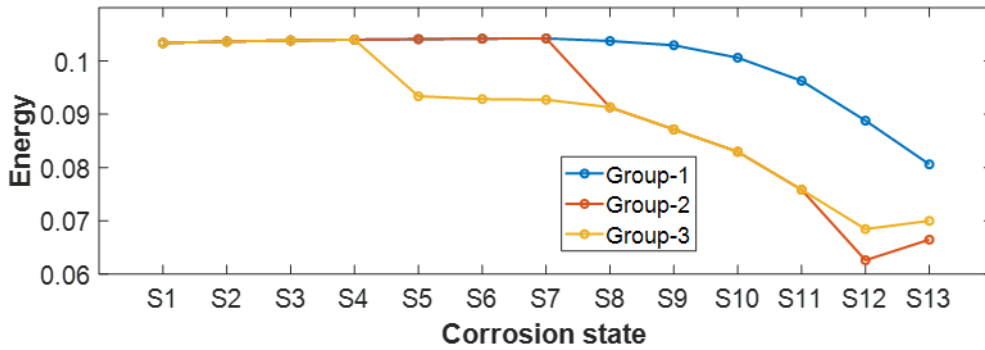
Collectively, the findings from AC-T4, AC-T5, and AC-T6 demonstrate that EM wave responses effectively capture and illustrate the different stages of corrosion, both in the active and passive states of the corrosion process.

### 5.3.4 Numerical simulation: Corrosion indications

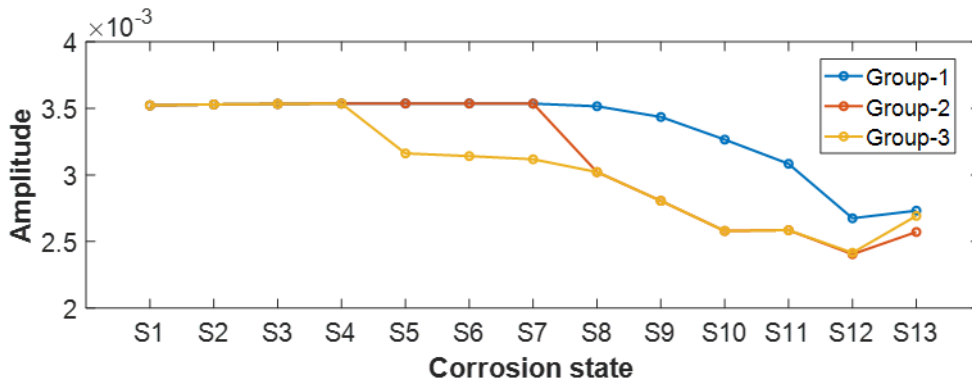
Numerical EM wave responses are being subjected to direct wave subtraction, time window determination for the rebar-rust area, and Fast Fourier Transform (FFT) analysis on the corresponding wave data. The



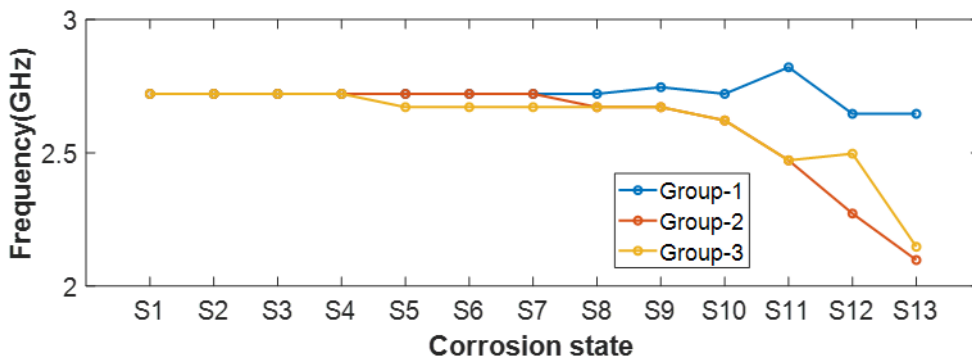
signal analysis reveals a distinct rise in signal energy, maximum amplitude, peak frequency magnitude, center frequency, and half-bandwidth of the peak frequency during the passive state (Figure 5.43). Conversely, these parameters exhibit a gradual decrease during the active state, mirroring the patterns observed in the experimental EM wave responses.



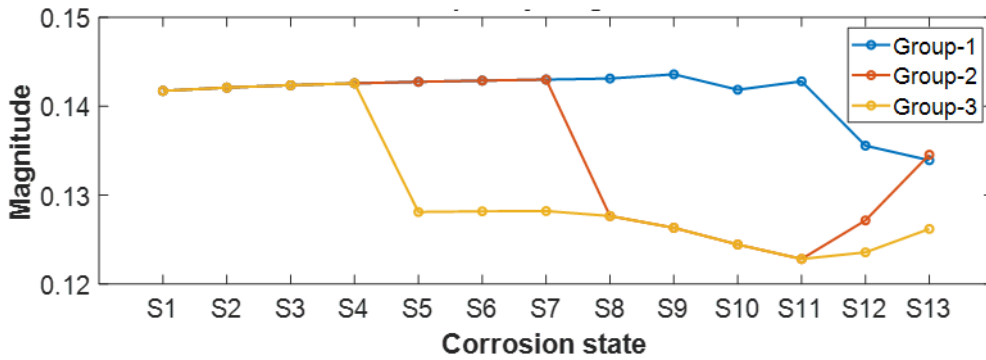
(a)



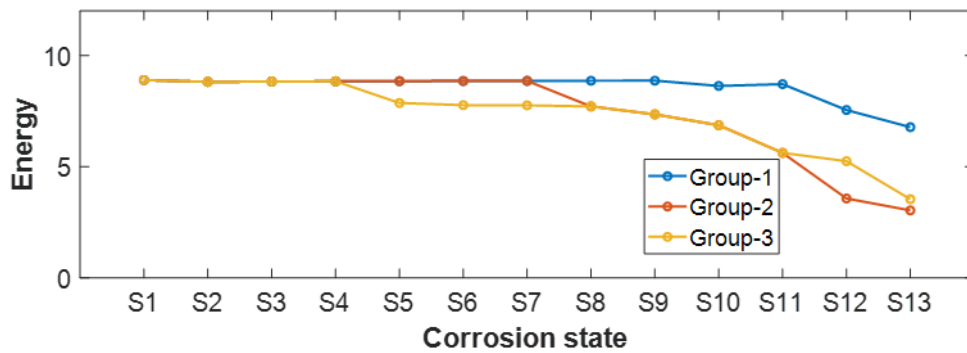
(b)



(c)



(d)



(e)

**Figure 5.43.** The signal post-processing analysis of the EM wave for numerical simulation provides insights into the changes in signal attributes for different groups 1,2 & 3 during both the passive and active corrosion states. These attributes encompass (a) signal energy, (b) signal maximum amplitude, (c) center frequency, (d) peak frequency magnitude, and (e) half-bandwidth of frequency energy.

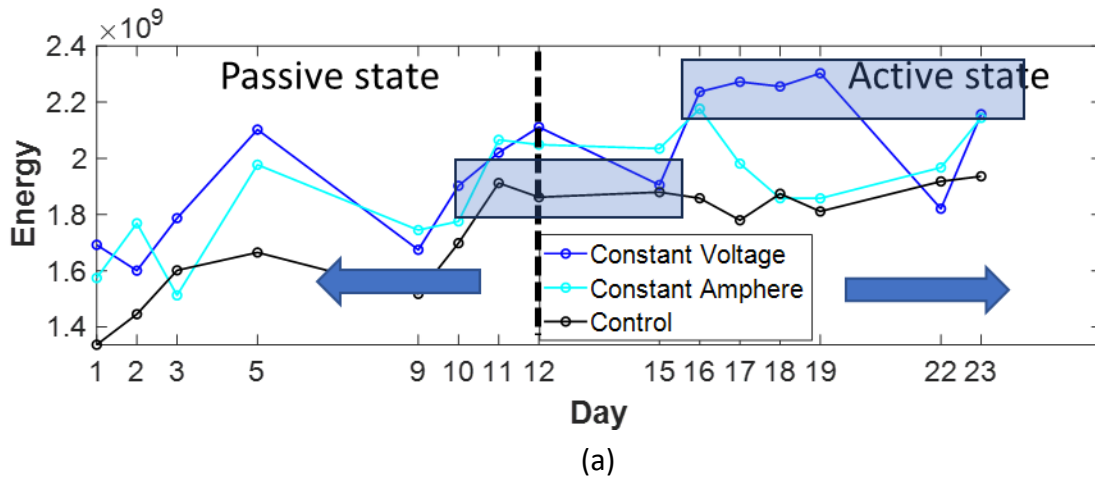
The cumulative findings from AC-T4, T5, and T6, combined with the outcomes from numerical EM wave analysis, strongly indicate that EM wave responses hold the capability to accurately delineate various stages of corrosion progression in both active and passive states of the corrosion process.

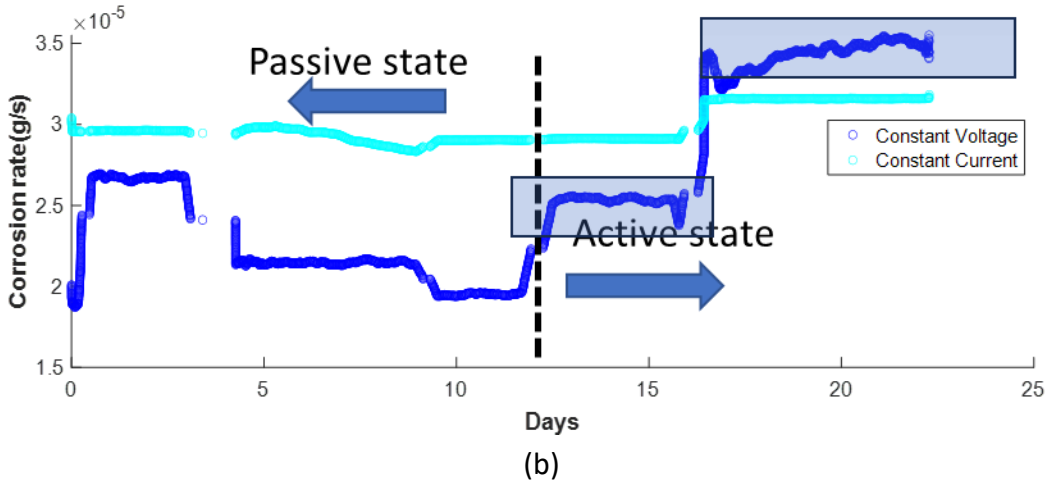
### 5.3.5 Discussion and conclusion

The series of six accelerated corrosion experiments yielded valuable insights into leveraging EM wave responses for discerning active and passive states during corrosion progression. The initial experiments, AC-T1 and AC-T2, illuminated the swift corrosion progression of rebar and embedded rebar in concrete within a span of just a day or two. This rapid corrosion was attributed to the robust 10A current supply from

the DC power unit. This revelation prompted a modification in the experimental setup to extend the duration to a month by reducing the applied current, recognizing its pivotal role in accelerating corrosion. The experiment AC-T3, focused solely on rebar, demonstrated that varying corrosion rates could be correlated with applied current, revealing greater mass reduction with constant voltage compared to a constant current setup (Figure 5.19). This highlighted the impact of corrosion rate on acceleration, where a gradual weight loss is seen in constant current conditions.

Determining corrosion rates through field testing is a challenging task, yet it's crucial to assess these rates to prevent the failure of bridge decks due to damage. Establishing a connection between corrosion rates observed in laboratory settings and the EM wave response proves invaluable in understanding the impact of corrosion in both passive and active states. The utilization of setups involving constant current and voltage provides a notable advantage, allowing for the quantification of corrosion rates in ways that are not feasible during real-world rebar corrosion in field conditions. This comprehension of corrosion rates further aids in distinguishing between active and passive states, leveraging half-cell potential measurements, and significantly enhancing the effectiveness of EM wave analysis.

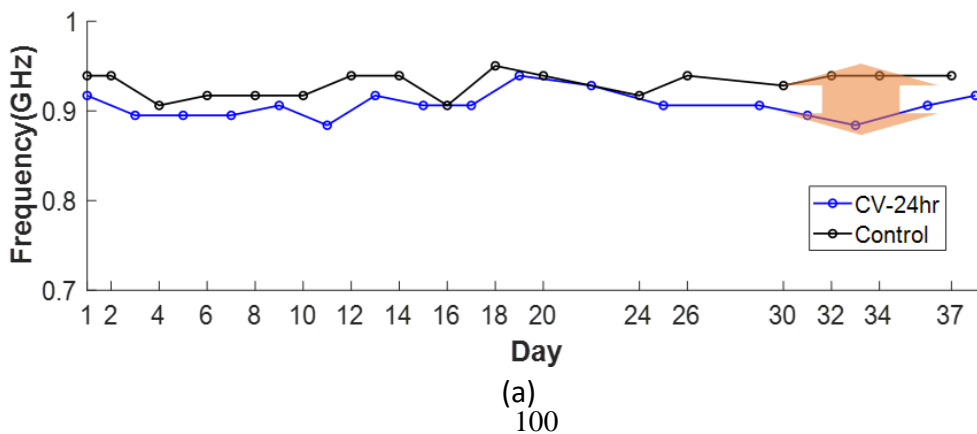




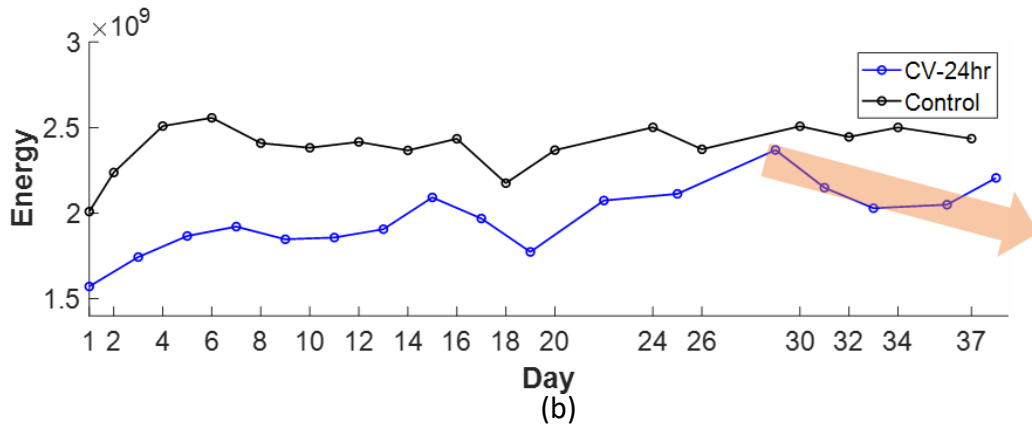
**Figure 5.44.** A parallel energy shift is observed in AC-T5 both: (a) half bandwidth frequency energy extracted from EM waves and (b) corrosion rate applied to the specimen.

Moving to experiment AC-T5, the evaluation of embedded rebar corrosion under a constant voltage/current system unveiled dynamic corrosion rate changes. Half-bandwidth energy derived from EM wave analysis exhibited a consistent trend during constant corrosion rates (Figure 5.44), followed by a sudden surge during active corrosion, aligned with similar observations in central frequency shifts. These findings showcased the potential of EM waves to detect early corrosion stages.

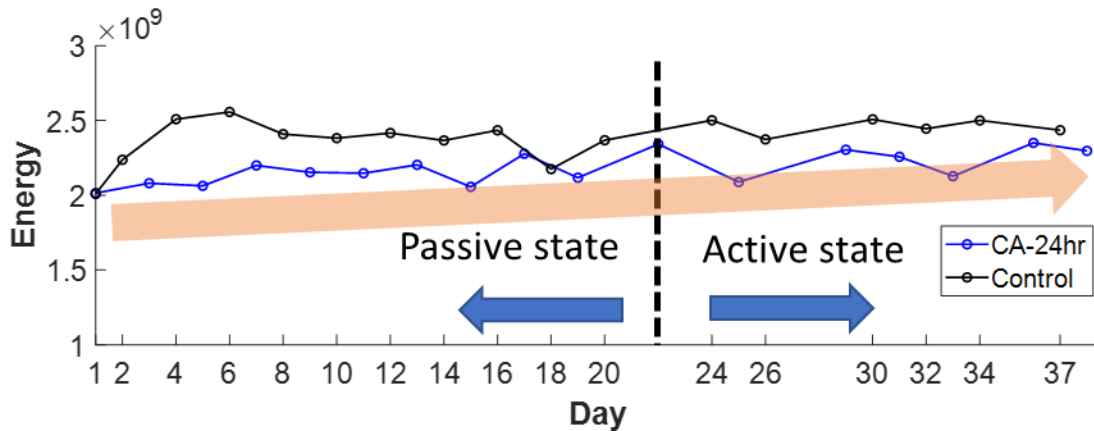
Upon scrutinizing the outcomes of AC-T6, it becomes evident that the constant current analysis merely presented a consistent rise across all signal features, lacking notable significance, as depicted in Figure 5.46. In contrast, when evaluating AC-T6's waveform response under constant voltage, a noteworthy shift in the pattern emerges, marked by fluctuations in both the center frequency and half-bandwidth energy, as illustrated in Figure 5.45.



(a)  
100

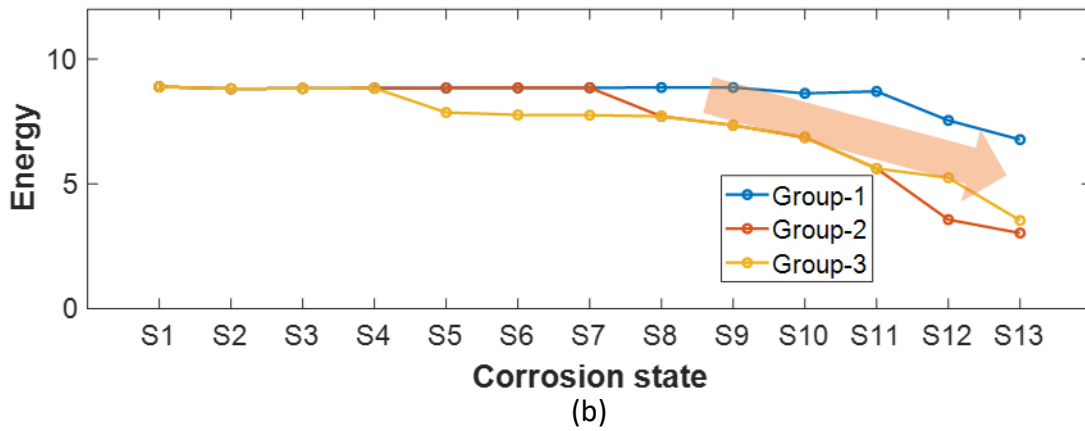
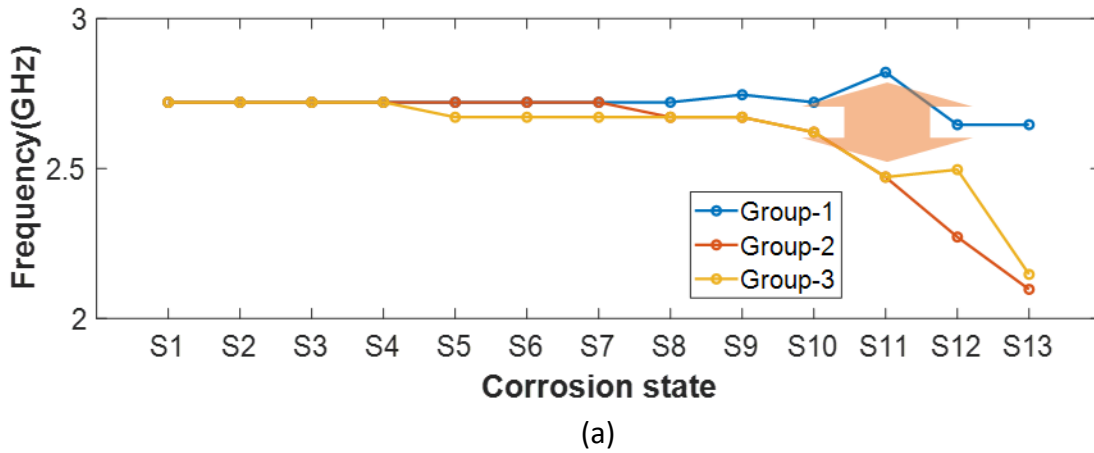


**Figure 5.45. Comparative study of the experimental EM wave analysis in AC-T6: (a) center frequency and (b) half bandwidth energy.**



**Figure 5.46. The analysis of AC-T6 constant current with EM waves exhibited a discernible but primarily upward trend without substantial significance.**

Regrettably, data collection was halted after day 14 due to technical issues, limiting conclusive EM wave signal processing analysis. To corroborate these responses, numerical simulations were conducted in AC-T6, modeling corrosion stages by varying dielectric constants, conductivity, and rebar reduction diameters as discussed in section 5.2.3. Simulation results reflected similar to experimental EM wave analysis of center frequency and half bandwidth energy as illustrated in Figure 5.47, underscoring the viability of numerical simulations for corrosion study.



**Figure 5.47. Comparative study of the numerical EM wave analysis: (a) center frequency and (b) half bandwidth energy.**

In summation, this chapter underscores how analyzing EM wave responses over the corroded rebar medium can effectively discern stages of corrosion progression. Additionally, numerical simulations serve as valuable supplementary tools for corrosion analysis, enriching our understanding of this intricate process,

## CHAPTER 6 FIELD STUDY

### 6.1 Motivation

National bridge inspections and Department of Transportation (DOT) requirements necessitate a rapid nondestructive testing method that doesn't disrupt traffic flow. The goal is to rapidly scan the bridge and promptly analyze the obtained results. DOTs primarily focus on assessing the bridge decks, many of which are around 30 to 40 years old and exhibiting initial signs of structural deterioration. The primary objective is to pinpoint localized damages in these bridge decks.

One of the most critical concerns in bridge monitoring is the occurrence of delamination and cracks due to corrosion. Such issues can lead to structural failure before the expected lifespan of the bridge. Typically, corrosion within bridge decks results from the reaction of chloride ions with rebar, triggered by moisture from rain and snow (Hugenschmidt, 2014; Parrillo, 2006; Senin, 2016). This chloride-ion-induced corrosion process generates corrosion byproducts around the rebar area, initiating delamination and cracks. The verification of delamination and cracks caused by corrosion often entails core extraction tests (Hong, 2014).

Over the years, various nondestructive testing methods have been developed and adopted in accordance with American standards, including dragging, hammer impact tests, and ground-penetrating radar (GPR) (Oh, 2013). Existing literature reveals the presence of single or multiple unit GPR systems capable of collecting data at slow speeds, typically ranging from 1 mph to 5 mph (Al-Qadi, 2005; Chen, 2014; Dong, 2016; Gucunski, 2015). However, these systems' low scanning speeds necessitate road closures, causing significant traffic disruptions on highways.

While 3D GPR systems have been previously developed, they entail high installation costs and computational analysis (Gui, 2020; Hoegh, 2016; Kang, 2019). Moreover, they require slow data collection speeds, leading to bridge closures, traffic congestion, and safety concerns. The focal point of my dissertation is the design and creation of a high-speed 3D GPR scanning system that can be mounted onto a vehicle.

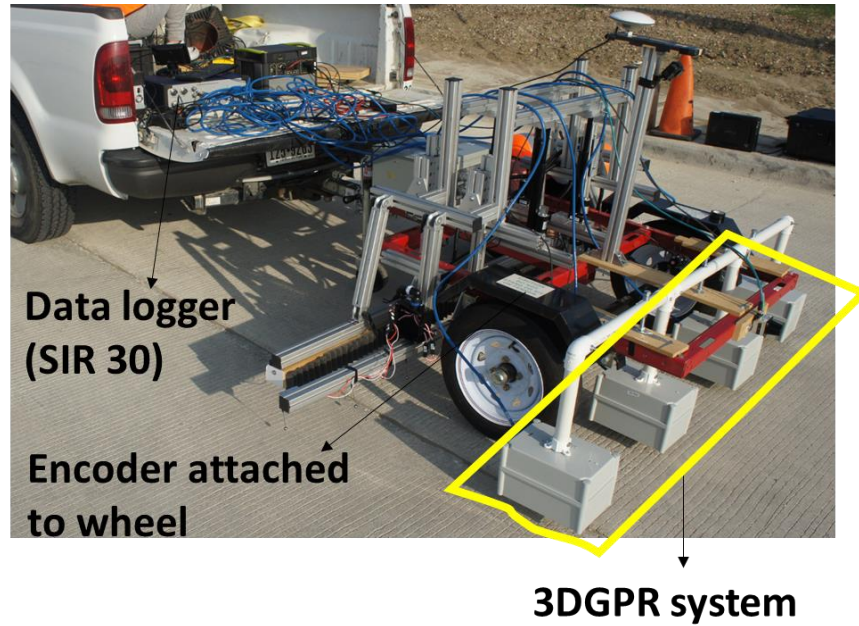
The primary challenge lies in developing a cost-effective, sustainable 3D GPR data acquisition system capable of capturing high-resolution data while the vehicle is in motion, ranging from speeds of 10 mph to 40 mph. Additionally, an economic analysis of the captured electromagnetic wave is undertaken. Furthermore, this system aims to generate a corrosion map by detecting amplitude attenuation around the rebar area, with the assistance of an encoder.

## **6.2 Advancement of a continuous 3DGPR scanning system**

The objective of the 3DGPR scanning system design is to achieve a high-speed scanning system utilizing four EM wave antennas operating at a frequency of 1600 MHz. These antennas are interconnected through the GSSI SIR 30 data acquisition system. To ensure the integrity of the system while it operates at high speeds, the four antennas are securely housed within a robust plastic polymer enclosure, as depicted in Figure 6.1. This strategic choice of utilizing a plastic polymer enclosure is made to prevent any interference or signal reflections that could arise from the enclosure itself during the data acquisition process.

To enhance the functionality of the system, two additional encoders are affixed to the trailer. These encoders serve the purpose of meticulously recording distance data from the commencement of the scan to its conclusion. The entire process is meticulously controlled by a laptop interface, ensuring precise management of the scanning procedure.





*Figure 6.1. The field-testing setup involves the 3DGPR system, incorporating the SIR 30 data acquisition logger along with an encoder affixed to the rotating wheel.*

### 6.3 Algorithm for post-processing rebar identification

#### 6.3.1 Direct wave and noise subtraction

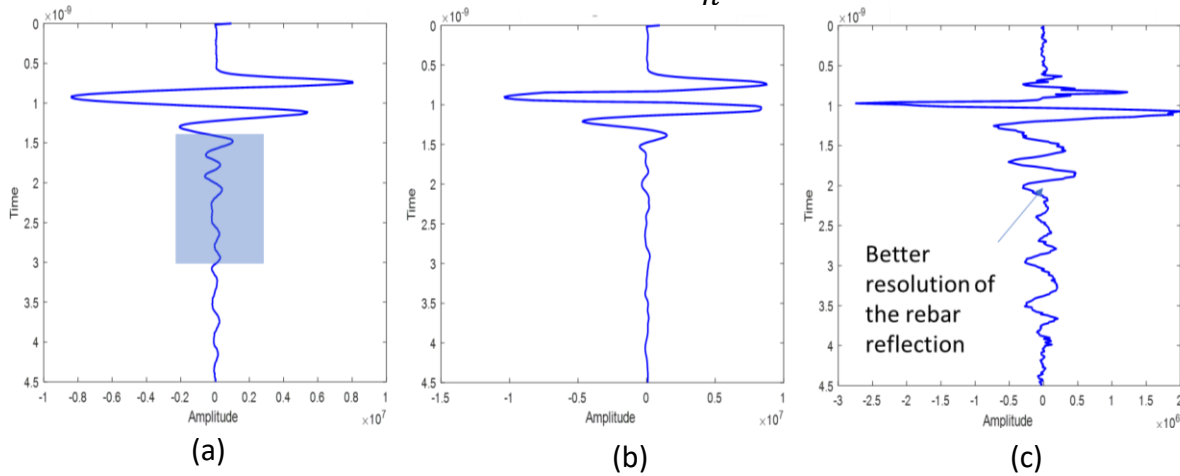
EM waves exhibit a notably strong reflective reaction to metal objects, as elucidated in the preceding Section 2.4.1. When antennas are positioned near the surface, the direct wave responses exert an influence on both the study of surface conditions and signal energy. Let us consider the EM wave A-scan response a  $S_i(t)$ , where  $i$  is Time step,  $i=1 \dots n$ . Here,  $n$  denotes the data size. The signal is expressed as:

$$S_i(t) \tag{6.1}$$

where  $t$  is the time. For a more comprehensive comprehension of rebar reflections, it is advantageous to eliminate the direct wave and noise stemming from environmental factors. This can be achieved by employing the average subtraction method outlined in Eq.6.2 on the collected data. The process of average subtraction ( $X_i(t)$ ) entails calculating the mean of all A-scan data acquired for each antenna and subsequently subtracting this mean from the corresponding data signals of said antennas. Through this

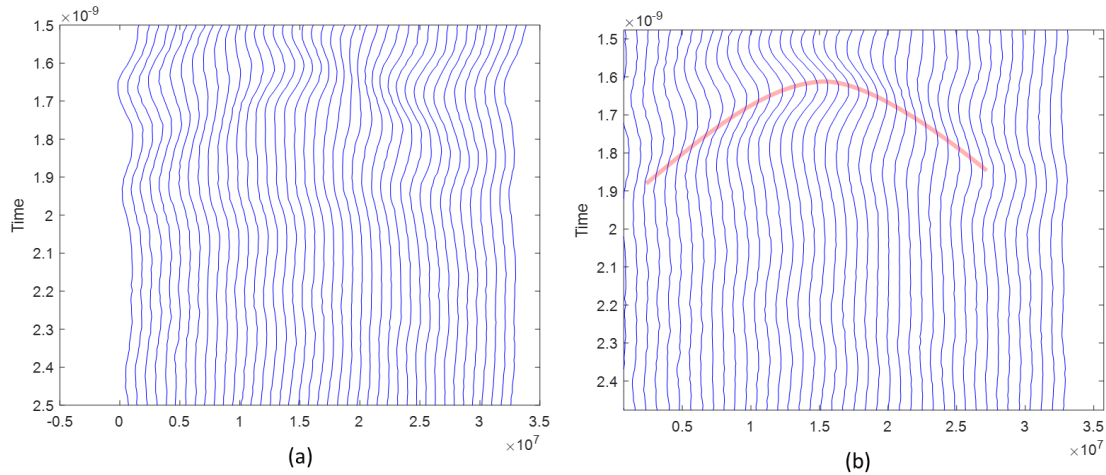
signal subtraction, the reflection from the top surface as well as the noise resulting from echoes can also be mitigated, resulting in a distinct peak response of the rebar reflections. The signal subtraction is expressed as:

$$X_i(t) = S_i(t) - \frac{\sum_{i=1}^n S_i(t)}{n} \quad 6.2$$

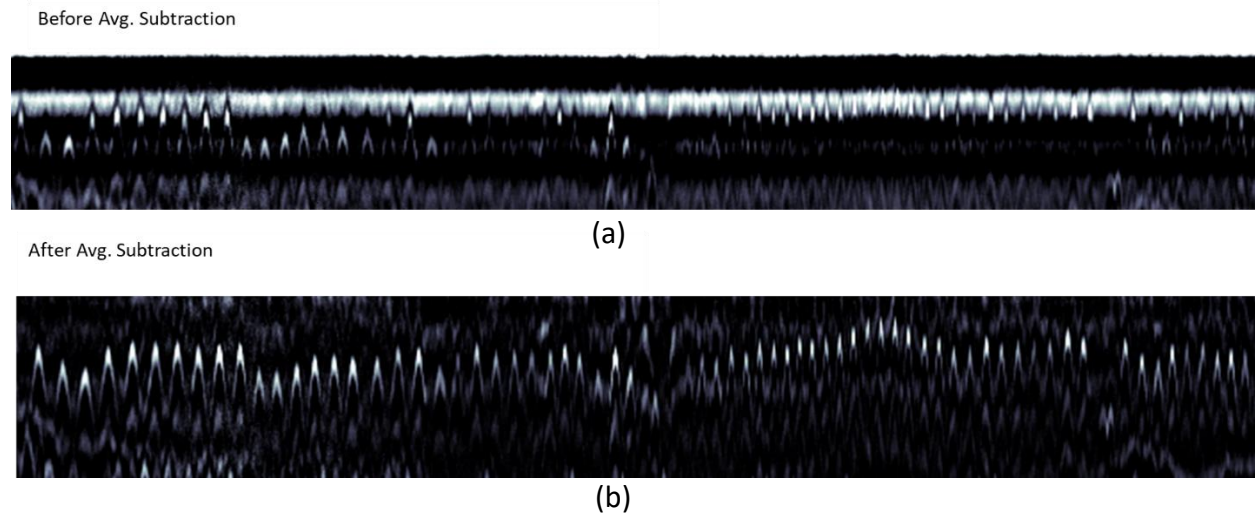


**Figure 6.2. Process of EM wave subtraction: (a) raw EM wave A-scan signal obtained from the data acquisition, (b) overall average of all the EM wave A-scans collected from the antenna and (c) subtracted EM wave signal, showing the rebar reflection after removal of noise and direct wave.**

Upon performing the subtraction process, distinct rebar responses become evident in Figure 6.2 (c) A-scan. As these A-scans are aggregated and aligned, the rebar reflection takes on a conspicuous hyperbolic shape, as depicted in Figure 6.3. Application of average subtraction to the raw data, resulting in a compilation of A-scans termed B-scans, as illustrated in Figure 6.4, provides a lucid and enhanced comprehension of rebar reflection, serving as a foundation for in-depth study.



**Figure 6.3.** Time steps of A-scans in proximity to the rebar location are depicted: (a) before subtraction and (b) after subtraction, revealing the distinct outline of the rebar.



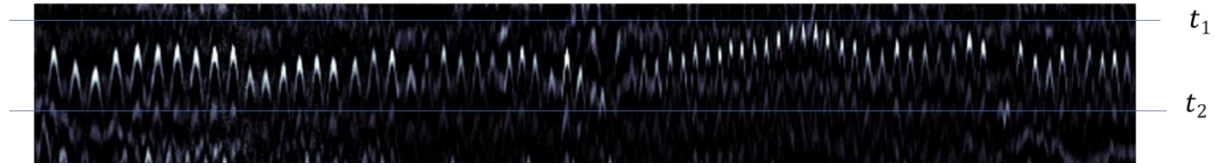
**Figure 6.4.** The unprocessed B-scan data (a) before and (b) after subtraction distinctly illustrate the hyperbolic reflection response of the EM wave.

### 6.3.2 Rebar picking and amplitude normalization.

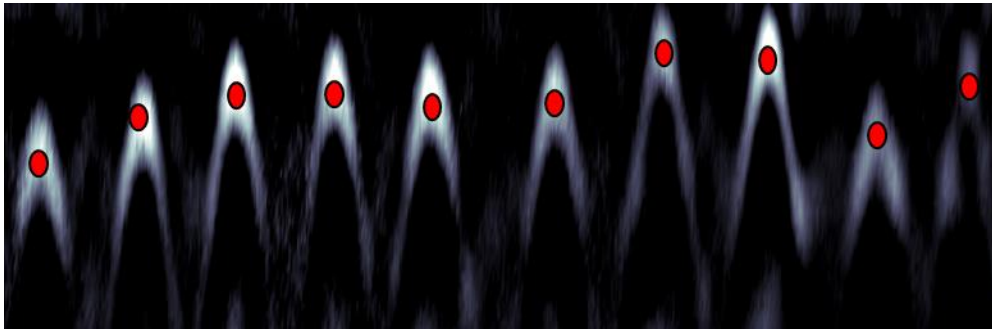
Upon aligning the subtracted A-scans, a composite B-scan is generated, revealing a succession of hyperbolic forms corresponding to the rebar placements within the bridge deck. The current objective involves precisely positioning the rebar at the center of each hyperbolic region, as depicted in Figure 6.6. Remarkably, all rebar hyperbolic reflections manifest within a distinct time window range between  $t_1$  and

$t_2 (X_w(t))$  characterized by conspicuous high amplitudes, as showcased in Figure 6.5 . The signal time window is expressed in:

$$X_w(t) = |X_i(t)|_{t_1}^{t_2} \quad 6.3$$



**Figure 6.5.** The rebar's hyperbolic reflection is observed to occur within a specific time window, between  $t_1$  and  $t_2$ , of the EM wave signal.



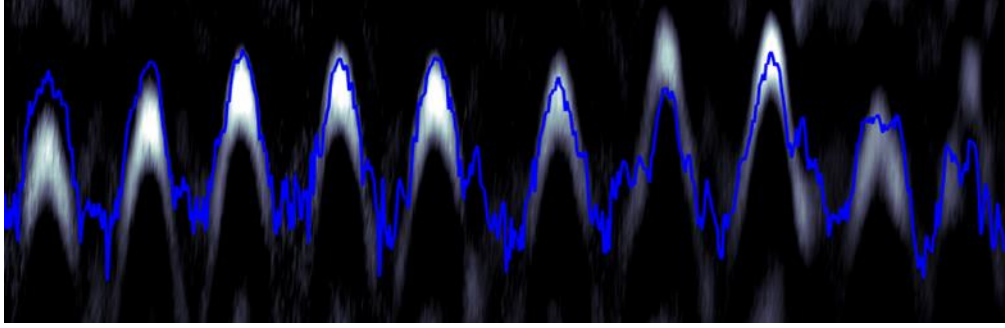
**Figure 6.6** Anticipated red dots signifying the targeted rebar location in need of identification.

Within this designated time window, the maximum amplitudes corresponding to various time points are accumulated and graphed across the B-scan, thus revealing the hyperbolic patterns along the scanned line, illustrated in Figure 6.7. Since the line of maximum amplitude serves as a representation of the hyperbolic rebar reflections acquired through GPR, the apex of each hyperbolic region can be identified as the peak of the respective curve on the maximum amplitude line ( $A_i, T_i$ ) akin to Figure 6.8 mirroring the concept presented in Figure 6.6. The culmination of each hyperbolic curve ( $A_m$ ) is ascertained from the maximum amplitude line, along with its corresponding time value ( $T_m$ ) signifying the amplitude of rebar reflection and the time required for the signal to travel from that specific rebar depth. Here, the subscript "m"

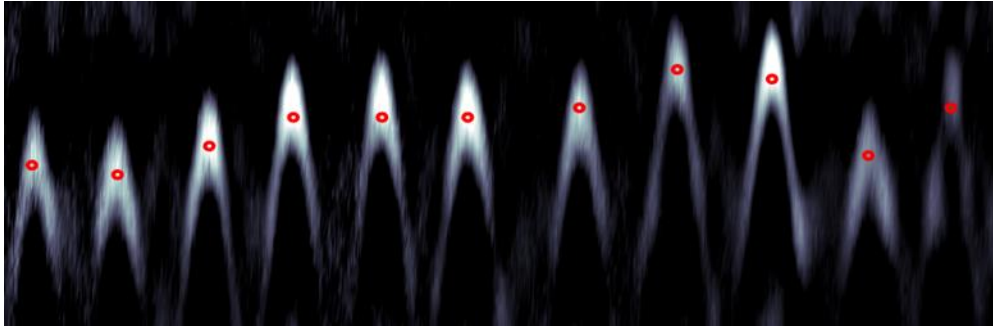
represents each individual rebar, with indices ranging from 1 to  $r$ , where  $r$  denotes the total number of rebars. The maximum amplitude line is obtained from:

$$A_i = X_w(t_{max}), T_i = t_{max}, \text{ when } X_w(t_{max}) = \max \quad 6.4$$

$$A_m = \max(A_i)|_r, T_m = t_p \quad 6.5$$



**Figure 6.7.** The maximum amplitude line (depicted in blue) is plotted over the B-scan within the specified time window.



**Figure 6.8.** The rebar locations are determined by identifying the peaks of the hyperbolic curves.

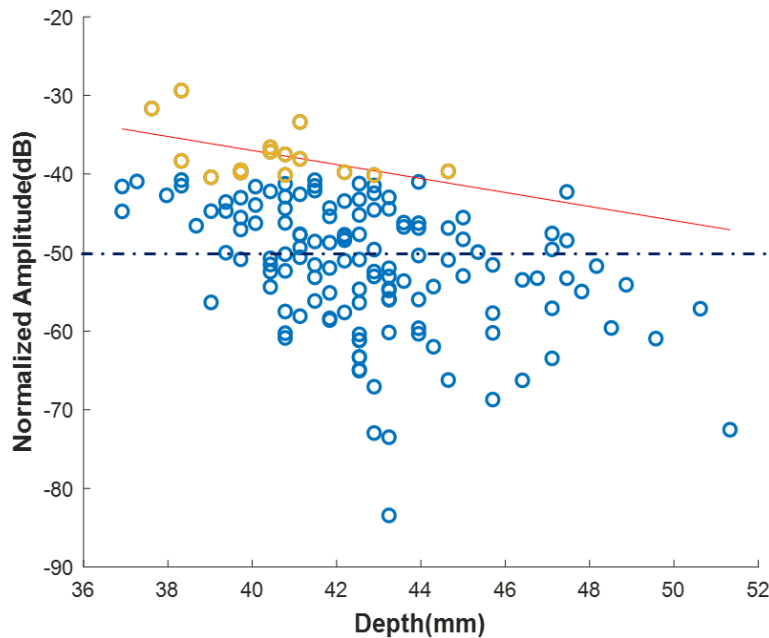
Upon plotting these points onto the B-scan, the desired rebar picking points are attained. To ensure consistency and mitigate abnormal high amplitude responses, the rebar picking points are normalized ( $A_{norm}$ ) expressed as:

$$A_{norm} = 20 \log \left( \frac{A_m}{A_{DW}} \right) \quad 6.6$$

where  $A_m$  represents the amplitude of the  $m^{\text{th}}$  rebar and  $A_{DW}$  denotes the average peak amplitude of the direct wave. Subsequently, these normalized amplitudes undergo further processing for amplitude-depth correlations and mapping.

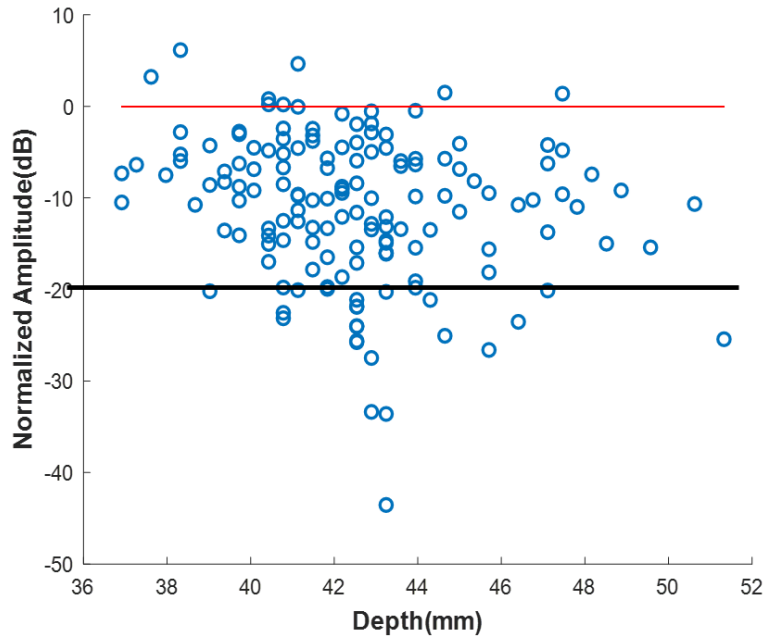
Given the rapid motion of vehicles, subtle depth variations in the rebar become apparent within the designated time window. The depths are computed using the equation presented in Section 2.4.1 (Eq.2.24). This amplitude-depth variance can be associated with the amplitude-depth correlation methodology (Dinh, 2016; Sun, 2018). The objective of this approach is to align the positions of rebar that exhibit low amplitude responses with those that have high amplitude responses. This alignment is achieved by considering the 90th percentiles of the rebar's normalized amplitude data points, which are established as reliable reflections from rebar through the earlier rebar selection process. Subsequently, a linear regression line (depicted as the red line in Figure 6.9), is derived from the data points beyond the 90th percentiles and superimposed onto the scatter plot of rebar normalized amplitudes, as illustrated in Figure 6.9.

Subsequently, all the rebar's normalized amplitude data points undergo an adjustment based on the linear fit regression line, resulting in updated rebar normalized amplitudes. This transformation effectively eliminates the influence of depth, as illustrated in Figure 6.10



**Figure 6.9.** The scatter plot depicting rebar picking in relation to depth is displayed prior to the amplitude-depth correlation, showcasing the range of variability in normalized amplitudes. The red line signifies the 90% regression line, while the black dashed line represents the corrosion threshold with before amplitude-depth correlation.





*Figure 6.10. The scatter plot illustrating rebar picking relative to depth is presented following the amplitude-depth correlation, highlighting the adjustment made to the normalized amplitude values. The red line signifies the 90% regression line, while the black solid line represents the corrosion threshold after amplitude-depth correlation.*

### 6.3.3 Mapping of the 3DGPR scanning data

Up until this point, all the collected and processed data pertains to a single antenna; however, the system's design encompasses four antennas for comprehensive bridge deck scanning. To amalgamate the data from all four antennas and obtain a clearer understanding of the corroded areas the overall amplitude normalization is executed by:

$$A_a = \text{mean}(A_{norm}), \quad 6.7$$

$$C_a = \frac{A_a}{\min(A_a)|_{a_n}}, \quad 6.8$$

$$A_{j,a} = C_a \cdot A_{norm}, \quad 6.9$$

where each antenna's normalized data ( $A_{j,a}$ ) is adjusted by a coefficient ( $C_a$ ) relative to the minimum of its normalized amplitudes ( $A_a$ ).

Once the rebar normalized amplitudes for all antennas ( $a_n$  is the number of antenna's 1...n) are obtained, the data sizes of these normalized amplitudes and the encoder readings are cross-referenced for correlation. The encoder data ( $D_k$ ) is then utilized to correlate with the rebar normalized amplitudes, enabling the creation of a corrosion map. The mapping procedure commences by normalizing the depth-correlated amplitudes of each antenna to prevent any anomalous high amplitude values. Given that the data collected through GPR occurs at a shorter time interval compared to the encoder data acquisition time interval, it is necessary to expand the encoder data points while maintaining the identical length of the bridge deck. The new encoder data by interpolation is expressed as:

$$D_j = D_k + (t_j - t_k) \cdot \frac{D_{k+1} - D_k}{t_{k+1} - t_k}, \quad \mathbf{6.10}$$

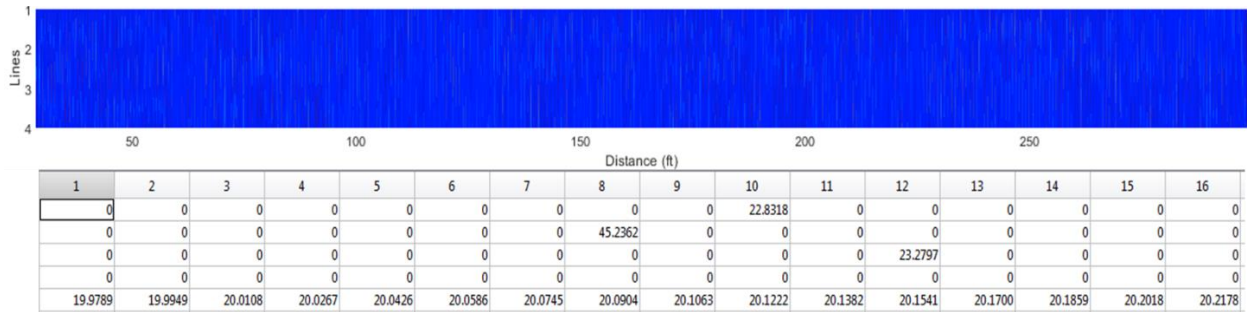
where  $D_k$  is the encoder data,  $D_j$  is the interpolated new encoder data,  $t_j$  is the new high resolution time ( $j=1..size\ of\ A_{j,a}$ ),  $t_k$  is the time of known encoder data time ( $k=1..size\ of\ D_k$ ),  $D_{k+1}$ ,  $D_k$  is the encoder data at interval at  $k+1$  and  $k$ . This expansion is achieved through interpolation, as described in Eq. 6.10, enabling the attainment of a comparable data size to that of the rebar normalized amplitudes.

Utilizing the newly adjusted encoder data, which now matches the data size of the rebar normalized amplitudes, the mapping of the scanned area is executed (Figure 6.11). However, upon plotting the resulting matrix, a notable presence of zero columns is observed due to the higher resolutions. To enhance visual clarity, these zero columns are removed (Figure 6.12).

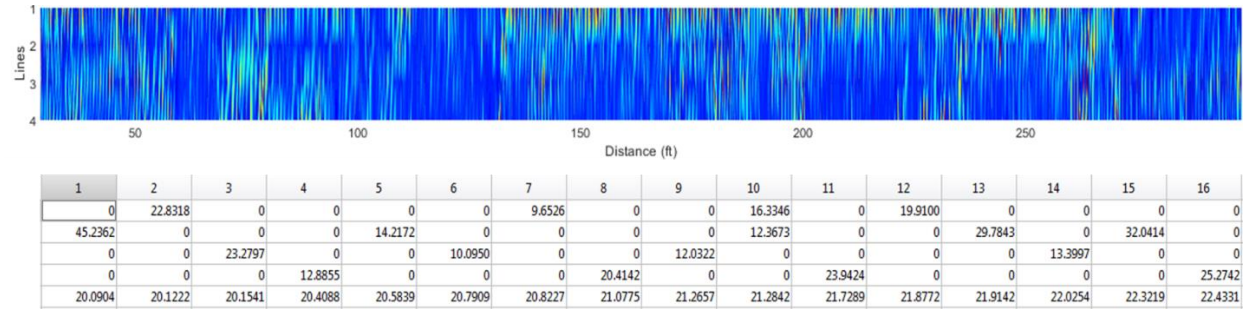
Subsequent to the removal of zero columns, the associated encoder values are likewise eliminated. However, this removal causes a noticeable variance in encoder resolution, leading to inaccurate representation of the rebar normalized amplitude area. To address this, in Figure 6.13 the encoder data and normalized amplitude matrix are realigned and combined within 3 inches (0.25ft). A final verification for



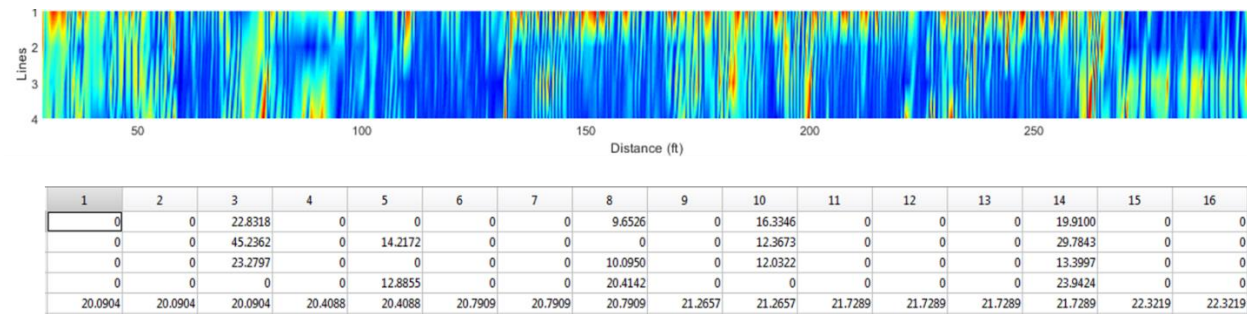
the presence of zero columns is conducted. The concluding stage of the mapping process entails aligning the encoder values according to the spacing specified in the bridge deck plan. This final alignment provides an accurate depiction of the rebar location areas.



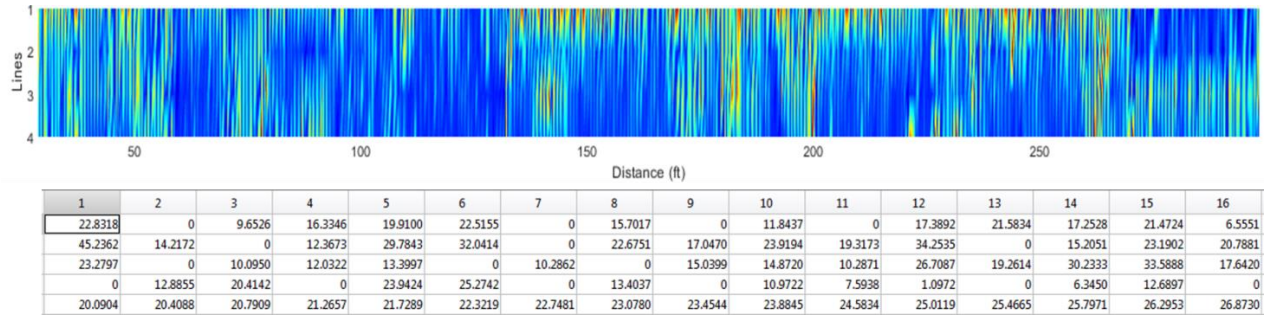
**Figure 6.11. Mapping: correlation between encoder readings and normalized rebar amplitudes.**



**Figure 6.12. Mapping refinement: zero column removal for enhanced visualization.**



**Figure 6.13. Mapping enhancement: aligning and merging normalized amplitudes at a 3-inch resolution, accompanied by inclusion of missing encoder values.**



**Figure 6.14. Mapping finalization: achieving conformity with rebar spacing in the plan through last realignment and zero column elimination.**

### 6.3.4 Corrosion thresholds

The preceding mapping procedures furnish rebar normalized amplitude values across the scanned lane. However, in order to identify corroded regions, the corrosion threshold (Sun, 2018) must be incorporated. Calculated using the disparity between the median and mean absolute deviation, the corrosion threshold (TH) is expressed as:

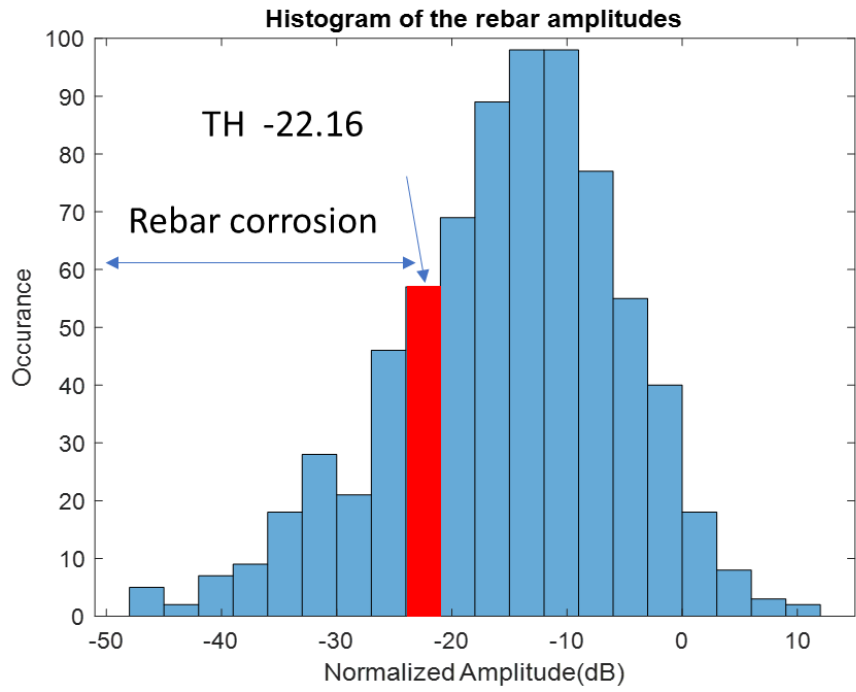
$$MAD = \text{median}(|A_{j,a} - \hat{A}|) \quad 6.11$$

$$\hat{A} = \text{median}(A_{j,a}) \quad 6.12$$

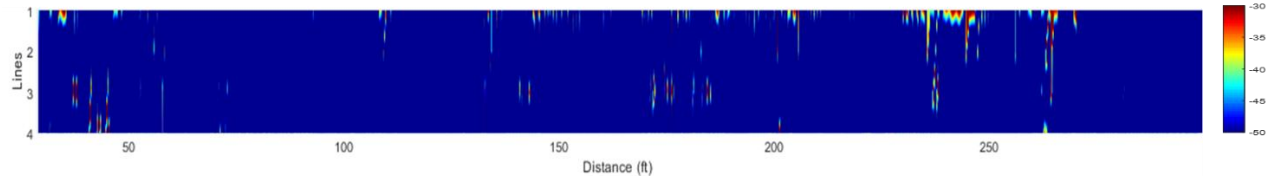
$$TH = \text{Median} - \text{Coeff} \times MAD \quad 6.13$$

where,  $MAD$  is the mean absolute deviation obtained from the median of the absolute subtraction of each normalized amplitude ( $A_{j,a}$ ) with median of the normalized amplitude data ( $\hat{A}$ ).

An illustrative instance is presented herein (Figure 6.15) depicting the amplitude histogram of the rebar for a designated lane. In this case, the threshold value calculated from the above Eq. 6.13 has been determined as -22.16. Any value below this threshold is categorized as a corroded area within that specific lane scan, as portrayed in the corresponding map Figure 6.16.



*Figure 6.15. The histogram illustrates the corrosion threshold, where normalized amplitude values below the threshold (TH) are categorized as corrosion.*



*Figure 6.16. Concluding corrosion area map following application of normalized amplitude corrosion threshold. The red spot indicates the area with a high probability of corrosion, as identified through EM wave analysis.*

**6.4 Field demonstration of 3DGPR scanning system**

**6.4.1 Inspection of Bridge 1**

In March 2022, a concrete bridge measuring 150 meters (496 feet) in length and 32 meters wide was selected for field inspection in Texas, United States, using the new 3DGPR system. The bridge, constructed

in 1960, features two lanes catering to one-way traffic. Employing the 3DGPR system, scanning was conducted along a 150-meter length and 4-meter width (each scanning path spanning 2 meters wide). Two scans, referred to as Lane 1 and Lane 2 in Figure 6.17 were carried out at a speed of 16 km/h. Following the bridge scanning, a virtual inspection was undertaken using recorded video footage, through which instances of cracks and spalling were identified. Figure 6.17 visually displays various surface defects gleaned from the recorded video imagery.

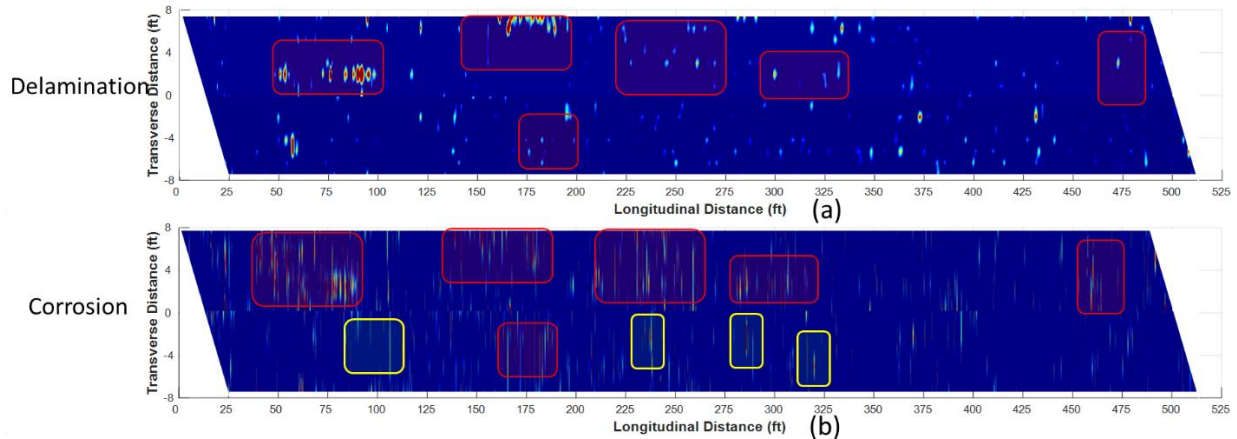


**Figure 6.17. Bridge scanning and surface defects visualization: The 3DGPR system covers a 150-meter length and 4-meter width area, employing four scanning paths (Lane 1 and Lane 2). The bridge deck exhibits multiple surface damages, including cracks and spalling.**

The corrosion map for the inspection of Bridge 1, as presented in Figure 6.18 emerges after the application of depth-corrected normalized amplitudes and the mapping procedure outlined in Section 6.3. Notably, the corrosion map displays substantial overlap (highlighted in red box) with the delamination map are document from the TxDOT monthly report submitted by Dr. Suyun Ham (Ham, 2023) .



Moreover, supplementary areas showing potential corrosion, indicated by the yellow box, were detected. These regions hint at the likelihood of corrosion-induced damage that could eventually result in delamination.

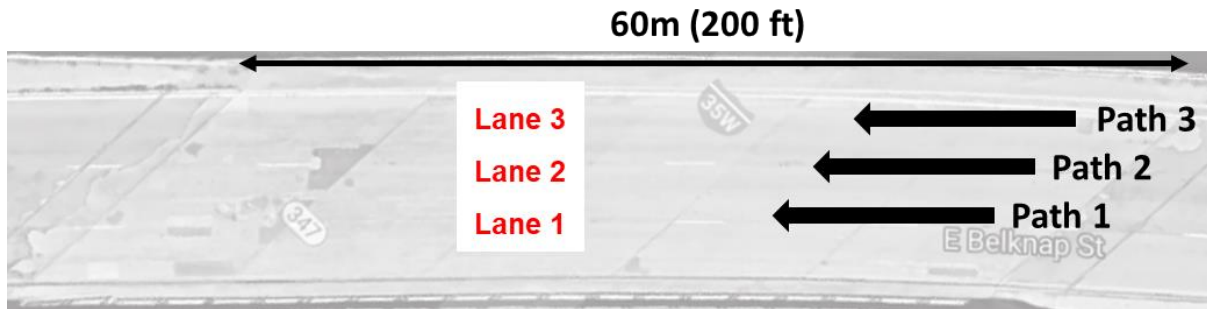


**Figure 6.18. Results of the initial bridge inspection: (a) Delamination Map, (b) Corrosion Map. The red box indicates the corresponding regions between the delamination and corrosion maps, while the yellow box highlights the corroded area that could potentially result in delamination.**

### 6.4.2 Inspection of Bridge 2

A concrete bridge measuring 60 meters (200 feet) in length and 32 meters in width, situated in Texas, United States, was selected for thorough field inspection utilizing the innovative 3DGPR system. This comprehensive inspection was conducted in March, June, and November of 2022. The bridge, originally built in 1961, boasts three lanes dedicated to one-way traffic flow.

Utilizing the 3DGPR system, scanning was carried out over an area of 60 meters in length and 6 meters in width (with each scanning path spanning 2 meters). A total of three scans (Path 1, Path 2, and Path 3 as indicated in Figure 6.19) were performed at a speed of 15 km/h. Subsequent to the bridge scanning, a virtual inspection was executed using recorded video footage, leading to the identification of spalling and potholes, which have been documented in Table 6.1.








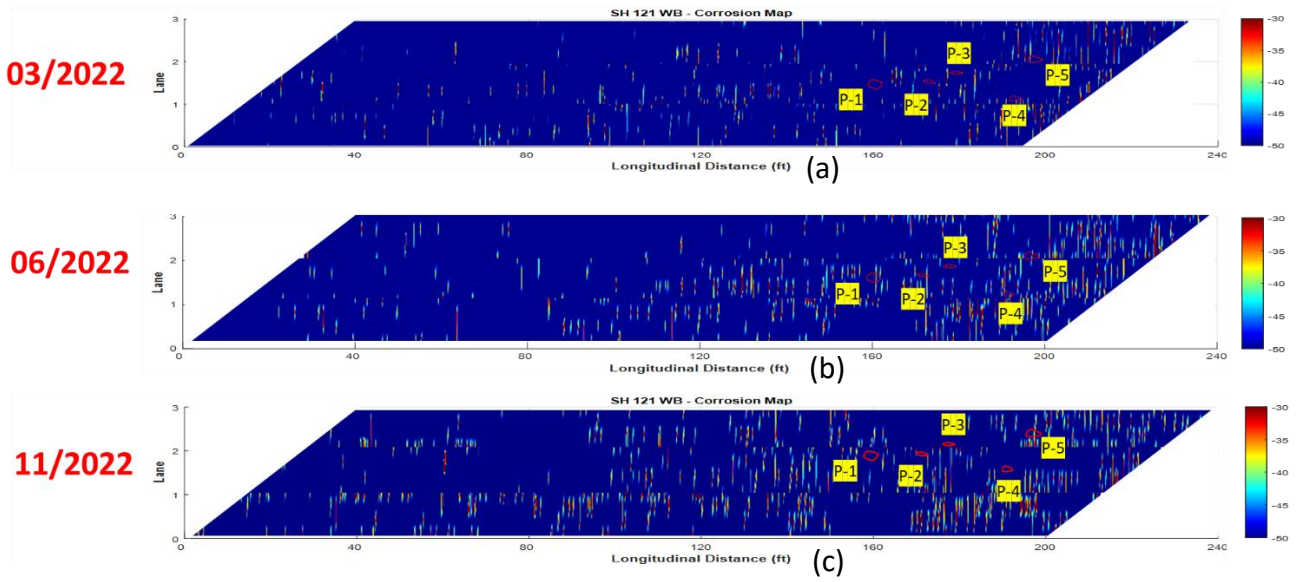
**Figure 6.19.** The bridge was subjected to scanning using the 3DGPR system, covering an expanse of 150 meters in length and 4 meters in width through four distinct scanning paths (designated as Lane 1 and Lane 2).

The corrosion maps were generated using the post-processing algorithm outlined in section 6.3. Remarkably, as Bridge 2 underwent multiple inspections, discernible alterations in the corrosion areas became evident with each subsequent month. From Figure 6.20, provides a clear depiction of this trend, highlighting a significant escalation of corrosion along Path-1 and Path-2. Notably, these pathways saw major repairs addressing potholes and spalling, which, unfortunately, led to further deterioration.

Referring to Table 6.1, it is evident that Path-1 (P-1) and Path-2 (P-2) experienced pronounced spalling. Moreover, Path-5 (P-5) exhibited the most severe damage, with rebar exposure to the environment, resulting in a heightened rate of corrosion progression. Impressively, the 3DGPR scanning system demonstrated its capacity to detect corrosion even following repair work. The extent of corrosion and delamination on this bridge deck was so severe that a replacement of the bridge was deemed necessary.

**Table 6.1. Progression of Detected Damage Across Three Scans.**

Patches	Visual Inspection	Corrosion Map Inference
P-1		Escalated corrosion conditions observed in the second (6/2022) and third (11/2022) scans
P-2		Escalated corrosion conditions observed in the second (6/2022) and third (11/2022) scans
P-3		Corrosion advancement noted in the third (11/2022) scan.
P-4		Consistent corrosion progression across all scans.
P-5		Ongoing corrosion progression across all scans.



*Figure 6.20. Bridge 2 inspection results: corrosion maps for three sequential scans: (a) 03/2022, (b) 06/2022 and (c) 11/2022, highlighting affected areas, alongside visual damage patches (Ham, 2023).*



## CHAPTER 7 CONCLUSION

The core focus of this dissertation revolves around an in-depth investigation into the influence of EM waves on moisture and corrosion within a complex, inhomogeneous medium. The initial phase of the study unveiled intriguing shifts in the frequency spectrum as the medium transitioned from saturation to dryness. The subsequent stages of experimentation and detailed numerical simulations focused on moisture effects validated and extrapolated the following significant insights:

- The study revealed consistent frequency spectrum variations during the transition from saturation to dryness. This was accompanied by evaporation patterns primarily concentrated in the upper portion of the medium. Analysis of baseplate arrival times demonstrated uncertainty, particularly at middle and end distances, indicating potential boundary effects or non-uniform drying as influencing factors. The utilization of the EM signal window within the moisture medium emerged as an effective strategy to mitigate uncertainties linked to boundary effects. Uncertainty in arrival times underscored the limitations of using the bottom plate as a reference. Focusing on the medium's signal window and processing the frequency spectrum unveiled a distinct shift in peak frequency during the transition from saturation to dryness.
- The designed 1600MHz antenna model displayed reliable analysis results, aligning well with experimental propagation of EM waves through air. Simulation models, created via a randomly generated particle algorithm, exhibited a similar match with experimental outcomes for an aggregate-void inhomogeneous medium, especially when examined alongside the antenna model. Notably, in Model M2, which simulated moisture changes in the upper aggregated water particle region, a pronounced frequency shift highlighted the correlation between moisture content and EM wave response. While there are limitations preventing a perfect match with the experimental data, further exploration through simulation model parameter studies could potentially lead to a significant level of alignment.

The study's second chapter showcases how EM wave analysis, combined with experiments and numerical simulations, effectively identifies corrosion stages in a rebar rust medium. This method provides crucial insights into corrosion progression, offering a promising approach for comprehending and studying corrosion processes across diverse scenarios:

- The series of six accelerated corrosion experiments yielded valuable insights into the effective utilization of EM wave responses for distinguishing between active and passive corrosion states. These experiments underscored the necessity of appropriately calibrating current levels for prolonged studies, revealing a direct correlation between high current supply and the rapid progression of corrosion.
- Experiments from AC-T3 testing demonstrated the significant role of current in accelerating corrosion. Notably, the experiment involving a constant voltage setup (AC-T3) exposed variations in corrosion rates when compared to constant current systems. The adoption of constant current/voltage configurations offered access to essential corrosion rate data, a crucial parameter that is often challenging to obtain under real-world field conditions.
- Employing constant current/voltage systems from AC-T5 testing revealed distinct alterations in corrosion rates through meticulous EM wave analysis. Noteworthy changes in half bandwidth energy and central frequencies pointed to discernible shifts between active and passive corrosion states, providing valuable early insights into the diverse stages of the corrosion process.
- Experiments conducted on embedded rebar from AC-T6 testing displayed comparable variations in EM wave responses during active corrosion states. While technical obstacles hindered data collection beyond the 14th day, the concurrent validation of experimental results by numerical simulations highlighted the promising potential of simulations for conducting comprehensive corrosion analysis.

- In addition, numerical simulations contributed substantial reinforcement to the corrosion analysis. Not only did they validate the experimental EM wave responses, but they also emphasized their feasibility as effective tools for delving into the complexities of the corrosion process.

Furthermore, the dissertation showcased innovative developments:

- The creation of a 3DGPR system proved to be a pivotal advancement for rapid bridge deck inspection. This system effectively detected potentially corroded rebar sections using a collaborative approach with multiple 1600MHz antennas and the SIR 30 system.
- The fusion of a meticulously designed mapping algorithm with encoder data offered a powerful technique for visualizing and comprehending bridge deck structural elements. This approach significantly enhanced assessments and analysis of surveyed regions.
- The application of the 3DGPR system in comprehensive field studies yielded remarkable outcomes, generating 2D interpolation maps that meticulously outlined potential regions of reinforcement corrosion across the scanned bridge territories.

In conclusion, this dissertation presents a comprehensive exploration of how EM waves exert influence over moisture, corrosion, and structural analysis. Its multifaceted approach yields valuable insights into these intricate phenomena, while also introducing innovative methodologies with practical applications in corrosion assessment and bridge inspection. The combined findings of EM wave analysis with medium response, encompassing both moisture and rebar-rust areas, contribute to a more accurate prediction of corrosion. Further advancements can be pursued through practical evaluations focused solely on the response above the rebar in 3DGPR analysis. Additionally, the avenue of exploration can be expanded by incorporating more intricate numerical simulation models, as this dissertation serves as a robust foundation that supports further advancements in the realm of environmental analysis.

## REFERENCES

- Al-Qadi, I. L., and Lahouar, S. (2005). Measuring layer thicknesses with GPR - Theory to practice, *Construction and Building Materials*, 19, 763–72. doi:10.1016/j.conbuildmat.2005.06.005
- Benedetto, A., and Benedetto, F. (2014). Application Field-Specific Synthesizing of Sensing Technology: Civil Engineering Application of Ground-Penetrating Radar Sensing Technology. *Comprehensive Materials Processing*, 13, 393–425. <http://dx.doi.org/10.1016/B978-0-08-096532-1.01315-7>
- Chen, D.-H., Hong, F., Zhou, W., and Ying, P. (2014). Estimating the hotmix asphalt air voids from ground penetrating radar. *NDT&E International*, 68, 120–127. <http://dx.doi.org/10.1016/j.ndteint.2014.08.008>
- Dinh, K., Gucunski, N., Kim J., and Duong, T.H. (2016). Understanding depth-amplitude effects in assessment of GPR data from concrete bridge decks. *NDT&E International*, 83, 48–58. <http://dx.doi.org/10.1016/j.ndteint.2016.06.004>
- Dong, Z., Ye, S., Gao, Y., Fang, G., Zhang, X., Xue, Z., and Zhang, T. (2016). Rapid Detection Methods for Asphalt Pavement Thicknesses and Defects by a Vehicle-Mounted Ground Penetrating Radar (GPR) System. *Sensors*, 16(12), doi: 10.3390/s16122067.
- Elsener, B., Andrade, C., Gulikers, J. and Polder, R. (2003). Half-Cell potential measurements – Potential mapping on reinforced concrete structures. *Materials and Structures*, 36, 461-471.
- Grosges, T., Vial, A., and Barchiesi, D. (2005). Models of Near-Field Spectroscopic studies: Comparison Between Finite-Element and Finite-Difference methods. *Optics Express*, 13(21), 8483-8497.
- Gucunski, N., Maher, A., Basily, B., La, H., Lim, R., Parvardeh, H., and Kee, S.-H. (2013). Robotic Platform Rabbit for Condition Assessment of Concrete Bridge Decks Using Multiple NDE Technologies. *CrSNDT*. 3(4).

- Gucunski, N., Romero, F., Kruschwitz, S., Feldmann R., and Parvardeh, H. (2011). *Comprehensive Bridge Deck Mapping of Nine by Nondestructive Technologies* (Report No. Project SPR-NDEB(90)--8H-00). Iowa Department of Transportation.
- Gui, Z., and Li, H. (2020). Automated Defect Detection and Visualization for the Robotic Airport Runway Inspection. *IEEE Access*, 8, 76100–76107. doi: 10.1109/ACCESS.2020.2986483.
- Ham, S. (2023). *Bridge inspection report*. (Report No. in progress). Texas Department of Transportation
- Hoegh, K., Tompkins, D., and Khazanovich, L. (2016). *Evaluation, Development, and Implementation of 3D GPR for Assessment of Minnesota Infrastructure*. (Report No. CTS 16-08). Center for Transportation Studies. <http://www.cts.umn.edu/Publications/ResearchReports/>
- Hong, S., Wai Lok Lai, W., Wilsch, G., Helmerich, R., Helmerich, R., Günther, T., and Wiggenhauser, H. (2014). Periodic mapping of reinforcement corrosion in intrusive chloride contaminated concrete with GPR. *Construction and Building Materials*, 66, 671–684. doi: 10.1016/j.conbuildmat.2014.06.019.
- Hugenschmidt, J., and Loser, R. (2008). Detection of chlorides and moisture in concrete structures with ground penetrating radar. *Materials and Structures*, 41(4), 785–792. doi: 10.1617/s11527-007-9282-5.
- Hugenschmidt, J., Wenk, F., and Bruhwiler, E. (2014). GPR Chloride Inspection of a RC Bridge Deck Slab Followed by an Examination of the Results. *IEEE 15th International Conference on Ground Penetrating Radar*.
- Jung, Y., Zollinger D.G., Won, M., and Wimsatt, A.J. (2009). *Subbase and Subgrade Performance Investigation for Concrete Pavement*. (Report No. FHWA/TX-09/0-6037-1). Texas Department of Transportation.
- Kang, M. S., Kim, N., Im, S. B., Jong J. L., and An, Y. K. (2019). 3D GPR Image-based UcNet for Enhancing Underground Cavity Detectability. *Remote Sensing*, 11(21). doi: 10.3390/rs11212545.

- Laurens, S., Balayssac, J.P., Rhazi, J., Klysz, G., and Arliguie, G. (2005). Non-destructive evaluation of concrete moisture by GPR: experimental study and direct modeling. *Materials and Structures*, 38, 827–832. doi:10.1617/14295.
- Lim, Y.-C., Noguchi, T., and Shin, S. (2010). Corrosion Evaluation by Estimating the Surface Resistivity of Reinforcing Bar. *Journal of Advanced Concrete Technology*, 8(2), 113-119.
- Ling, T., He, W., Zhang, S., Zhang, L., Huang, F., and Hua, F. (2022). Calculation of the permittivity of inhomogeneous media based on the TEDAWT method. *Journal of Applied Geophysics*, 196. <https://doi.org/10.1016/j.jappgeo.2021.104513>.
- Oh, T., Kee, S.-H., Arndt R.W., Popovics, J. S., and Zhu, J. (2013). Comparison of NDT Methods for Assessment of a Concrete Bridge Deck. *Journal of Engineering Mechanics*, 139(3), 305–314. doi: 10.1061/(asce)em.1943-7889.0000441.
- Parrillo, R., Roberts, R. and Haggan, A. (2006). *Bridge Deck Condition Assessment Using Ground Penetrating Radar*. ECNDT.
- Patil, A., and Patil, J. (2011). Effects of Bad Drainage on Roads. *Civil and Environmental Research*, 1(1).
- Pour-Ghaz, M., Isgor, O. B., and Ghods, P. (2009). Quantitative Interpretation of Half-Cell Potential Measurements in Concrete Structures. *Journal of Materials in Civil Engineering*, 21(9).467-475. doi: 10.1061/ASCE0899-1561200921:9467.
- Pratanu, G. and Tran, Q. (2015). Influence of Parameters on Surface Resistivity of Concrete. *Cement and Concrete Composites*, 62, 134–145. <http://dx.doi.org/10.1016/j.cemconcomp.2015.06.003>.
- Roqueta, G., Jofre, L., and Feng, M. Q. (2012). Analysis of the Electromagnetic Signature of Reinforced Concrete Structures for Nondestructive Evaluation of Corrosion Damage. *IEEE Transactions on Instrumentation and Measurement*, 61(4), 1090–1098. doi: 10.1109/TIM.2011.2174106.

- Senin, S. F., and Hamid, R. (2016). Ground Penetrating Radar Wave Attenuation Models for Estimation of Moisture and Chloride Content in Concrete Slab. *Construction and Building Materials*, 106, 659–669. doi: 10.1016/j.conbuildmat.2015.12.156.
- Stratfull, R. F. (1973). Half-Cell Potentials and The Corrosion of Steel in Concrete.
- Sun, H., Pashoutani, S., and Zhu, J. (2018). Nondestructive Evaluation of Concrete Bridge Decks with Automated Acoustic Scanning System and Ground Penetrating Radar. *Sensors*, 18(6). doi: 10.3390/s18061955.
- Warren, C., and Giannopoulos, A. 2011. Creating finite-difference time-domain models of commercial ground-penetrating radar antennas using Taguchi's optimization method. *Geophysics*, 76(2). G37-G47. doi: 10.1190/1.3548506.
- Yee, K.S. (1966). Numerical Solution of Initial Boundary Value Problems Involving Maxwell's Equations in Isotropic Media. *IEEE Transactions on Antennas and Propagation*, 14(3).